
**MINISTERUL EDUCAȚIEI ȘI CERCETĂRII**

**Universitatea Națională de Știință și Tehnologie**

**POLITEHNICA BUCUREȘTI**

**Ingineria Sistemelor Biotehnice**

**Eng. Cesar BANU**

# Ph. D. Thesis Summary

**Scientific Coordinator:**

**Prof.Univ. Habil. Dr. Eng. Mihai BUGARU**

**2025**

MINISTERUL EDUCAȚIEI ȘI CERCETĂRII

Universitatea Națională de Știință și Tehnologie

POLITEHNICA BUCUREȘTI

Ingineria Sistemelor Biotehnice

# DUAL NUMERICAL-EXPERIMENTAL INVESTIGATIONS REGARDING THE PREDICTION OF GEOMETRIC DISTORTIONS INDUCED BY RESIDUAL STRESSES GENERATED IN THE FABRICATION OF MULTILAYERED ANISOTROPIC STRUCTURES

**Scientific coordinator:**

**Prof.Univ. Habil. Dr. Eng. Mihai BUGARU**

**Ph.D. Student:**

**Eng. Cesar BANU**

**2025**

# Contents

## Abreviations

2D / 3D – bidimensional/ tridimensional

ATL - Automated Tape Laying

C-SPAR1 - U-shaped profile specimen with a rectangular developed surface (220x200 mm) and a thickness of 3.0 mm

C-SPAR2 - U-shaped profile specimen with a rectangular developed surface (220x200 mm) and a thickness of 5.0 mm

C-SPAR3 - U-shaped profile specimen with a rectangular developed surface (220x200 mm) and a variable thickness of 3.0mm-5.0 mm

CAD - Computer aided design

CTE – Coefficient of thermal expansion

CLT – Classical lamination theory

CMM – Coordinate measuring machine

CFRP – Continuous fiber reinforced polymer

CHILE - *Cure-hardening instantaneous linear elastic*

CPU - Computational

DC – Direct current dielectric sensor

DMA – Dynamic mechanical analysis

DSC – Diferential scanning calorimetry

FBG – Fiber Bragg Gratings

FE – Finite Elements

FEA – Finite Elements Analysis

FEM – Finite Element Method

FOS – Fiber Optic Sensors

OFDR - Optical Frequency Domain Reflectometer

OOA – Out of Autoclave

PBCs – Periodic boundary conditions

PVT – Pressure, volume, temperature experimental equipment

RTM - Resin transfer molding

RTM6 – HexFlow RTM6-2 resin system

SKIN1 – Curved skin-type specimen with a rectangular developed surface (280x200 mm) and a thickness of 2.5 mm

SKIN2 – Curved skin-type specimen with a rectangular developed surface (280x200 mm) and a thickness of 6.5 mm

SKIN3 – Curved skin-type specimen with a rectangular developed surface (280x200 mm) and a thickness of 11.5 mm

UD - Unidirectional

VARTM – Vacuum assisted resin transfer moulding

# INTRODUCTION

Composite materials with layered fibers fabricated using thermosetting resins exhibit distortions as a result of the manufacturing process. The shape of a composite part slightly deviates between the beginning and end of the polymerization process due to several irreversible phenomena. If these distortions are not anticipated, assembling multiple structural components may require the application of unacceptable forces or may generate internal stresses that affect the structural behavior during operation. Given the rapid expansion in the use of layered composite materials in the construction of high-performance structures (aircraft, vehicles, ships, etc.), the research topic addressed is of significant importance and current relevance.

The thesis is structured into seven chapters that cover the current state of research regarding the prediction of geometric distortions at both theoretical and experimental levels (Chapters 1 and 2); experimental evaluations of geometric distortions induced by residual stresses (Chapter 3); calibration of measurements, estimation of uncertainties and errors (Chapter 4); development of a numerical tool for distortion simulation, simulation of distortions, and calibration of the simulation tool on test specimens (Chapter 5); simulation and experimental study of distortions on aeronautical composite structures (Chapter 6); and original contributions and conclusions (Chapter 7).

Despite numerous studies on distortions induced by polymerization, the literature still lacks tested and validated methodologies for their comprehensive evaluation. The increasing complexity of structures made from layered composites renders empirical rules obsolete, while relying on trial-and-error experimental sequences involves prohibitive additional costs and significant delays. This thesis focuses on the development of numerical tools capable of predicting the shape and magnitude of distortions. The use of numerical simulation helps avoid costly experimental studies. A dual numerical-experimental method is proposed with the objective of predicting geometric distortions in structures made from layered composites.

Another contribution of the thesis lies in improving the feasibility and accuracy of the simulation methodology for the polymerization process, addressing the pressing need to characterize material properties. Instead of characterizing the material at the composite level, a homogenization method is used to predict the properties of the multi-phase material based on its constituents. One of the novel aspects of the approach is the application of finite element homogenization to coarsely modeled unidirectional laminates, where the geometric representation of fibers often overlaps. Instead of consuming resources to eliminate these overlaps, they are managed using non-conforming meshes and a procedure for reallocating fiber volume in overlapping regions. Another innovation is the holistic approach to simulate polymerization behavior and estimate the shape and distortion values for full-scale (1:1) structural samples and specimens.

# 1. CURRENT STATE OF THEORETICAL RESEARCH ON THE PREDICTION OF GEOMETRIC DISTORTIONS INDUCED BY RESIDUAL STRESSES GENERATED DURING THE FABRICATION OF MULTILAYERED ANISOTROPIC STRUCTURES

In composite manufacturing processes, the final shape of composite parts does not precisely match the shape of the mold at the end of the process due to distortions induced during fabrication. Geometric distortions are caused by the manufacturing process itself, which generates residual stresses within the composite components. The non-uniform distribution of residual stresses in composite materials leads to deformation, matrix cracking, and even delamination.

These distortions are commonly referred to in the industry by established terms such as "spring-in"/"spring-out" for curved elements (e.g., joints, angles, corners) and "warping" for flat components, panels, or shell structures. The issues caused by distortions arise during and after the assembly of composite parts, primarily due to poor contact between mating surfaces — unless the magnitude of these distortions has been accurately predicted and remains within assembly tolerance limits.

## 1.1 MECHANISMS RESPONSIBLE FOR THE GENERATION OF RESIDUAL STRESSES AND GEOMETRIC DISTORTIONS

### 1.1.1 THERMAL ANISOTROPY

Differences in the coefficient of thermal expansion (CTE) between the fiber and the resin generate residual stresses at both the micro- and macro-scale. In curved panels, the CTE mismatch between the through-thickness direction and the circumferential direction leads to a reduction in the enclosed angle of the part—an effect commonly referred to in curved sections as spring-in.

The first attempt to calculate the magnitude of this angular deviation was proposed by Nelson and Cairns, as expressed in Equation 1.1:

$$\Delta\theta = \theta \frac{(\alpha_\theta - \alpha_R)\Delta T}{1 + \alpha_R \Delta T} \tag{1.1}$$

În care:

- $\Delta\theta$ - spring-in angle;
- $\theta$ - the part outer fillet angle;
- $\alpha_\theta$ - coefficient of thermal expansion in the circumferential direction (fiber direction);
- $\alpha_R$ - radial coefficient of thermal expansion (through-thickness direction of the laminate);
- $\Delta T$ - temperature variation;

### 1.1.2 RESIN SHRINKAGE DURING THE CURING PROCESS

To account for the effect of polymerization shrinkage on the spring-in phenomenon, Radford and Diefendorf [BC1.21] introduced a polymerization shrinkage term into Equation 1.1, and the spring-in angle is then expressed as follows:

$$\Delta\theta = \theta\left[\frac{(\alpha_\theta - \alpha_R)\Delta T}{1+\alpha_R\Delta T} + \frac{\varepsilon_\theta - \varepsilon_R}{1+\varepsilon_R}\right] \quad (1.2)$$

Where:

- $\varepsilon_\theta$ - In-plane deformation caused by polymerization shrinkage;
- $\varepsilon_R$ - Through-thickness deformation caused by polymerization shrinkage.

### 1.1.3 TOOL-PART INTERACTION

This phenomenon, inherent in manufacturing processes, leads to a non-uniform distribution of stresses, which become residual as the resin cures. These stresses induce bending moments when the composite part is removed from the mold, resulting in shape distortion.

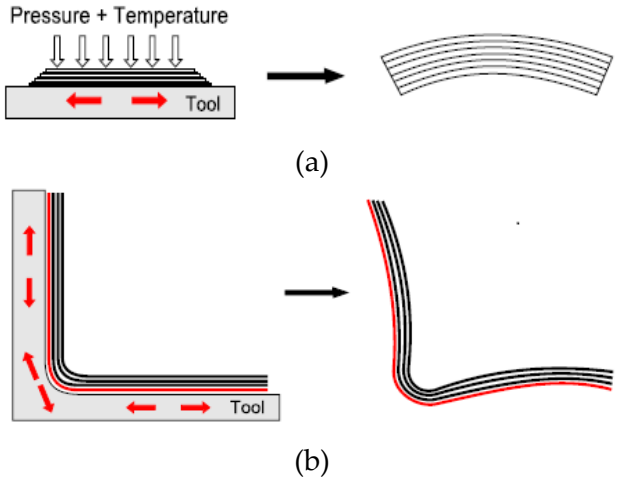


***Figure 1.1**. Tool-part interaction a) Flat part; b) Corner*

### 1.1.4 FIBER IMPREGNATION WITH RESIN AND LAYER COMPACTION

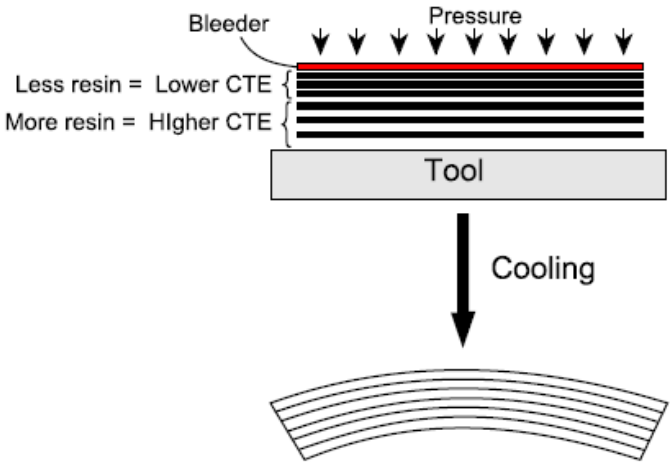


**Figure 1.2** Effect of Fiber Impregnation on the Distortion of Panel-Type Laminates

Figure 1.2 illustrates the formation of resin-rich regions at the mold interface and resin-deficient regions at the laminate–vacuum bag interface. As the part thickness is reduced through compaction induced by atmospheric pressure or additional pressure applied in an autoclave (via the vacuum bag), friction between fiber layers (particularly in prepregs) prevents them from conforming precisely to the mold geometry in corner regions. The applied pressure becomes ineffective at the part corners due to fiber bridging.

### 1.1.5 TEMPERATURE VARIATION

Temperature gradients through the thickness are negligible for thin parts, but for thicker components, the rapid temperature increase during manufacturing—combined with the low thermal conductivity of the composite—can result in a significant through-thickness temperature and polymerization gradient [***BC1.23***].

## 1.2 PHYSICAL MODELS

### 1.2.1 TERMOKINETICS

The mathematical expression of heat transfer, given in Equation 1.3, is solved to predict the temperature history of the fiber-reinforced polymer.

$$\rho C_p \frac{\partial T}{\partial t} = \nabla(k\nabla T) + q_{gen} \qquad (1.3)$$

Where:

- $\rho$ – density;
- $C_p$ – specific heat capacity;
- k – thermal conductivity tensor;
- $\nabla$ - differential operator ;

In general, **homogenized material properties** are used for composites. The term $q_{gen}$ in Equation 1.3 refers to the heat generated during the exothermic reaction of the polymer matrix and can be expressed as follows [***BC1.27, BC1.28***]:

$$q_{gen} = \left(1 - V_f\right)\rho_r H_{tr} R_r(\psi, T) \qquad (1.4)$$

Where:

- $H_{tr}$ – total reaction heat;
- $\rho_r$ – resin density;
- $V_f$ – fiber volume ratio;
- $\psi$ – cure degree;
- $R_r(\psi, T)$ - the cure reaction as a function of $\psi$ and T.

### 1.2.2 RHEOLOGY AND VARIATION OF THE DEGREE OF CURE

Polymerization is most commonly defined by the degree of cure, $\alpha$ which can be determined from the ratio between the heat generated by the process **(H(t))** at a specific time and the total heat generated throughout the entire process (Htr) [***BC1.36***] and can be expressed as follows:

$$\alpha = \frac{H(t)}{H_{tr}} \qquad (1.5)$$

### 1.2.3 VOMULE SHRINKAGE DURING CURING

The chemical shrinkage of the resin during the polymerization process can be expressed as the total volumetric change ($V_{sh}$), as explained in the following parahraph. Starting from the premise of a uniform variation per unit volume, the incremental isotropic deformation ($\dot{\varepsilon}_r^c$ deformatia) is calculated for a thermosetting resin using the following relation[***BC1.24***]:

$$\dot{\varepsilon}_r^c = \sqrt[3]{1 + \Delta\alpha \cdot V_{sh}} - 1 \tag{1.6}$$

Where:

- $\Delta\alpha$– the cure degree variation;
- $V_{sh}$ – the volumetric shrinkage of the thermoset resin;

The volumetric shrinkage of the resin begins after the gelation point and follows a linear dependence on the degree of cure $\alpha$ [***BC1.49***].

### 1.2.4 COMPACTION

The manufacturing process of fiber-reinforced laminated materials can be modeled by considering the three states of the resin: viscous, elastomeric (gel), and vitreous. In the viscous state, the liquid flows and impregnates the fibers due to pressure gradients within the laminate. Fiber impregnation has been modeled using a 2D model [***BC1.60, BC1.61***] or composite materials based on Darcy's law for flow in porous media. The theory developed by Darcy was coupled with the internal material stresses in these studies. For most laminated composites, one dimension is significantly larger than the other two, justifying the use of a plane strain state associated with the model [***BC1.60, BC1.61***]. It is assumed that the resin is an incompressible Newtonian fluid.

## 1.3 CONSTITUTIVE MATERIAL MODELS

In this section, we will describe the various approaches to defining constitutive models, as outlined in the specialized literature. The linear elastic model, the viscoelastic model, and material-specific models with structure-dependent constitutive properties are discussed. The relationship between stresses and strains is presented along with the elastic modulus of the polymer matrix. The effective mechanical properties, as well as the thermo-chemical volumetric shrinkage for composite samples, are calculated using micromechanical methods.

### 1.3.1 LINEAR ELASTIC MODEL

The elastic modulus of the polymer matrix is defined as a function of the degree of cure and is expressed as follows[***BC1.24***]:

$$E_r = (1 - \propto_{mod}) E_r^0 + \propto_{mod} E_r^\infty + \gamma \propto_{mod} (1 - \propto_{mod})(E_r^\infty - E_r^0) \tag{1.7}$$

and

$$\propto_{mod} = \frac{\alpha - \alpha_{mod}^{gel}}{\alpha_{mod}^{diff} - \alpha_{mod}^{gel}} \tag{1.8}$$

Where:

- $E_r^0$ and $E_r^\infty$- The elastic moduli for the fully unpolymerized resin, respectively, the elastic modulus for the fully polymerized resin;

- $\alpha_{mod}^{gel}$ si $\alpha_{mod}^{diff}$ – These are the boundaries of the interval in which the elastic modulus of the resin increases from its initial value to its final value;
- $\gamma$ – Parameter that describes the relaxation of internal stresses during curing [***BC1.24***]

In the calculations, it is approximated that $E_r^0 = E_r^\infty/1000$ [***BC24, BC50, BC67***]. Equation 1.7 has been modified to include the temperature dependence, as suggested in the CHILE method [***BC1.23, BC1.68***] which indicates both solidification during curing and the variation of the modulus with temperature, as shown in the equation 1.14:

$$E_r = \begin{cases} E_r^0 \\ E_r^0 + \frac{T^* - T_{C1}}{T_{C2} - T_{C1}}(E_r^\infty - E_r^0) \\ E_r^\infty \end{cases} \text{ for } \begin{cases} T^* \le T_{C1} \\ T_{C1} < T^* < T_{C2} \\ T_{C2} < T^* \end{cases} \quad (1.9)$$

În care:

- $T_{C1}$ si $T_{C2}$- critical temperatures of the glass transition interval;
- $T^*$ - the instantaneous difference between the glass transition temperature and the temperature T of the resin. $T^* = T_g - T$ [***BC1.23, BC1.68***].

### 1.3.2 STRESS_STRAIN DEPENDENCE

The stresses and displacements induced by the curing process can be solved incrementally using FEM. At each calculation step, the total strain ($\dot{\varepsilon}^{tot}$) is composed of the mechanical strain ($\dot{\varepsilon}^{mec}$), deformațiile termice ($\dot{\varepsilon}^{th}$) and chemical strains ($\dot{\varepsilon}^{c}$) and can be written as in Equation 1.10:

$$\begin{aligned} \dot{\varepsilon}_{ij}^{tot} &= \dot{\varepsilon}_{ij}^{mec} + \dot{\varepsilon}_{ij}^{th} + \dot{\varepsilon}_{ij}^{c} \\ \dot{\varepsilon}_{ij}^{pr} &= \dot{\varepsilon}_{ij}^{th} + \dot{\varepsilon}_{ij}^{c} \\ \dot{\varepsilon}_{ij}^{mec} &= \dot{\varepsilon}_{ij}^{tot} - \dot{\varepsilon}_{ij}^{pr} \end{aligned} \quad (1.10)$$

$$\dot{\sigma}_{ij} = C_{ijkl}\dot{\varepsilon}_{ij}^{mec} \quad (1.11)$$

The stresses induced by the process ($\dot{\varepsilon}_{ij}^{pr}$) and calculated incrementally are defined by the sum $\dot{\varepsilon}_{ij}^{th} + \dot{\varepsilon}_{ij}^{c}$. The incremental stress tensor ($\dot{\sigma_{ij}}$) is calculated using the stiffness matrix ($C_{ijkl}$) which is a function of temperature and degree of cure, based on the incremental mechanical strain tensor ($\dot{\varepsilon}_{ij}^{mec}$).

At the end of each step (time increment **n**), the stress and strain tensors are recalculated:

$$\sigma_{ij}^{n+1} = \sigma_{ij}^{n} + \dot{\sigma}_{ij}^{n} \quad (1.12)$$

$$\varepsilon_{ij}^{n+1} = \varepsilon_{ij}^{n} + \dot{\varepsilon}_{ij}^{n} \quad (1.13)$$

### 1.3.3 VISCOELASTIC MODEL

Viscoelastic models are presented in the literature in two forms: differential and integral. In general, the integral form has been adopted by most researchers [***BC1.50, BC1.70-BC1.78***].

$$\sigma_{ij} = \int_0^1 C_{ijkl}(\psi, T, \xi - \xi')\frac{\partial \varepsilon_{kl}(\xi')}{\partial \xi'} d\xi' \quad (1.14)$$

Where:

$$\xi(t) = \int_0^t \frac{dt}{\chi(\psi,T)} \quad (1.15)$$

$$\xi(t') = \int_0^{t'} \frac{dt\prime}{\chi(\psi,T)} \quad (1.16)$$

ξ si ξ′ are the current reduced time parameter and the reduced time interval of the process, t si t′ are the current time and the process duration, respectively, χ si ψ are the temperature and degree of cure, dependent on the scaling factor. The elastic modulus of the polymer matrix, without residual stresses, can be approximated using a Prony series [***BC1.71***]:

$$E_r(\psi, T, t) = E_r^{rel} + (E_r^{rel} - E_r^{unrel}) \sum_i^n w_i exp\left[\frac{-\xi(\alpha,T)}{\tau(\psi)}\right] \quad (1.17)$$

Where $E_r^{rel}$ is the modulus without residual stresses, $E_r^{unrel}$ is the modulus with residual stresses, $w_i$ is the mass scaling factor, and, $\tau(\psi)$ are the discrete time moments described as a function of the cure factor.

### 1.3.4 MATERIAL-SPECIFIC MODELS WITH CONSTITUTIVE DEPENDENCY STRUCTURE

A simplified version of the viscoelastic model was proposed in [***BC1.12, BC1.67, BC1.79, BC1.80***] by introducing the time-dependent evolution of the material. Thus, the stress-strain relationships can be expressed as follows:

$$\sigma_{ij} = \begin{cases} C_{ijkl}^r \varepsilon_{kl,} & T^* \leq 0 \\ C_{ijkl}^g \varepsilon_{kl,} - \left[(C_{ijkl}^g - C_{ijkl}^r)\varepsilon_{kl,}\right]_{t=t_{vit}}, & T^* > 0 \end{cases} \quad (1.18)$$

### 1.3.5 EQUILIBRIUM CONDITIONS

In the case of stresses, the gradients are in static equilibrium, so for a control volume, we can write the following force equilibrium equation for the surface unit *t(S)* and the volume unit *f(V)*:

$$\int tdS + \int fdV = 0 \quad (1.19)$$

The Cauchy stress matrix at a point in S is defined by:

$$t = n \cdot \sigma \quad (1.20)$$

Where n is the normal to the surface S at the considered point:

$$\int n \cdot \sigma dS + \int fdV = 0 \quad (1.21)$$

Using Gauss's theorem, we rewrite the surface integral as a volume integral, as follows:

$$\int n \cdot \sigma dS = \int \nabla \sigma dV = 0 \quad (1.22)$$

## 1.4 MODELLING THE TOOL-PART INTERACTION

Most studies on the interaction between the matrix and the component, considering the nature of the phenomena, are experimental studies whose results aimed at calibrating numerical simulations and models.

The critical shear stress at which sliding occurs is mathematically expressed by the equation *1.23*:

$$\tau_{cr} = \mu \cdot P \quad (1.23)$$

## REFERENCES – CHAPTER 1

**[BC1.1]** Campbell FC. *Manufacturing technology for aerospace structural materials.* London: Elsevier; 2006

**[BC1.2]** Li M, Tucker C L. *Optimal Curing for Thermoset Matrix Composites: Thermochemical and Consolidation Considerations.* Polymer Composites 2002; 23(5):739-757

**[BC1.3]** Laurenzi S, Marchetti M (2012) Advanced composite materials by resin transfer molding for aerospace applications, composites and their properties. Ning Hu (ed). ISBN: 978-953-51-0711-8. InTech. doi:10.5772/48172.

**[BC1.4]** Wisnom MR, Gigliotti M, Ersoy N, Campbell M, Potter KD (2006) Mechanisms generating residual stresses and distortion during manufacture of polymer-matrix composite structures. Compos A 37:522–529

**[BC1.5]** Parlevliet PP, Bersee HEN, Beukers A (2006) Residual stresses in thermoplastic composites—a study of the literature—part I: formation of residual stresses. Compos A Appl Sci Manuf 37:1847–1857

**[BC1.6]** Parlevliet PP, Bersee HEN, Beukers A (2007) Residual stresses in thermoplastic composites—a study of the literature—part II: experimental techniques. Compos A Appl Sci Manuf 38:651–665

**[BC1.7]** Parlevliet PP, Bersee HEN, Beukers A (2007) Residual stresses in thermoplastic composites—a study of the literature—part III: effect of thermal residual stresses. Compos A Appl Sci Manuf 38:1581–1596

**[BC1.8]** Ito Y, Obo T, Minakuchi S, Takeda N (2015) Cure strain in thick CFRP laminate: optical-fiber-based distributed measurement and numerical simulation. Adv Compos Mater 24(4):325–342

**[BC1.9]** Nelson RH, Cairns DS (1989) Prediction of dimensional changes in composite laminates during cure. 34th International SAMPE symposium and exhibition, vol 34, pp 2397–2410

**[BC1.10]** Sarrazin H, Kim B, Ahn SH, Springer GS (1995) Effects of processing temperature and lay-up on springback. J Compos Mater 29(10):1278–1294

**[BC1.11]** Gigliotti M, Wisnom MR, Potter D (2003) Development of curvature during the cure of AS4/8552 [0/90] unsymmetric composite plates. Compos Sci Technol 63:187–197

**[BC1.12]** Svanberg JM, Holmberg JA (2001) An experimental investigation on mechanisms for manufacturing induced shape distortions in homogeneous and balanced laminates. Compos A 32:827–838

**[BC1.13]** Ersoy N, Potter K, Wisnom MR, Clegg MJ (2005) Development of spring-in angle during cure of a thermosetting composite. Compos A 36:1700–1706

**[BC1.14]** Radford DW, Rennick TS (2000) Separating sources of manufacturing distortion in laminated composites. J Reinf Plast Compos 19(8):621–640

**[BC1.15]** Garstka T (2005) Separation of process induced distortions in curved composite laminates. Ph.D. thesis, University of Bristol

**[BC1.16]** Hahn HT, Pagano NJ (1975) Curing stresses in composite laminates. J Compos Mater 9(1):9–91

**[BC1.17]** Weitsman Y (1979) Residual thermal stresses due to cool-down of epoxy-resin composites. J Appl Mech 46(3):563–567

**[BC1.18]** Adolf D, Martin JE (1996) Calculation of stresses in crosslinking polymers. J Compos Mater 30(1):13–34

**[BC1.19]** Sunderland P, Yu W, Manson JA (2001) A thermoviscoelstic analysis of process-induced internal stresses in thermoplastic matrix composites. Polym Compos 22(5):579–592

**[BC1.20]** Kevin D, Beaumont PWR (1997) The measurement and prediction of residual stresses in carbon-fibre/polymer composites. Compos Sci Technol 57(11):1445–1455

**[BC1.21]** Radford DW, Diendorf RJ (1993) Shape instabilities in composites resulting from laminate anisotropy. J Reinf Plast Compos 12(1):58–75

**[BC1.22]** Hubert P, Poursartip A (1998) A review of flow and compaction modelling relevant to thermoset matrix laminate processing. J Compos Mater 17(4):286–318

**[BC1.23]** Johnston A (1997) An integrated model of the development of process-induced deformation in autoclave processing of composite structures. Ph.D. thesis, The University of British Columbia

**[BC1.24]** Bogetti TA, Gillespie JW Jr (1992) Process-induced stress and deformation in thick-section thermoset composite laminates. J Compos Mater 26(5):626–660
**[BC1.25]** Bogetti TA, Gillipse JW (1989) Processing-induced stress and deformation in thick section thermosetting composite laminates. CCM report. University of Delaware, August, pp 89–21
**[BC1.26]** Ruiz E, Trochu F (2005) Numerical analysis of cure temperature and internal stresses in thin and thick RTM parts. Compos A 36:806–826
**[BC1.27]** Baran I, Tutum CC, Hattel JH (2013) The effect of thermal contact resistance on the thermosetting pultrusion process. Compos B Eng 45:995–1000
**[BC1.28]** Baran I, Hattel JH, Tutum CC (2013) Thermo-chemical modelling strategies for the pultrusion process. Appl Compos Mater 20:1247–1263
**[BC1.29]** Liu XL, Crouch IG, Lam YC (2000) Simulation of heat transfer and cure in pultrusion with a general-purpose finite element package. Compos Sci Technol 60:857–864
**[BC1.30]** Baran I, Tutum CC, Hattel JH (2013) Optimization of the thermosetting pultrusion process by using hybrid and mixed integer genetic algorithms. Appl Compos Mater 20:449–463
**[BC1.31]** Baran I, Tutum CC, Hattel JH (2013) Reliability estimation of the pultrusion process using the first- order reliability method (FORM). Appl Compos Mater 20:639–653
**[BC1.32]** Ersoy N, Garstka T, Potter K, Wisnom MR, Porter D, Clegg M, Stringer G (2010) Development of the properties of a carbon fibre reinforced thermosetting composite through cure. Compos A 41:401–409
**[BC1.33]** Akkerman R (2002) On the properties of quasi-isotropic laminates. Compos B Eng 33:133–140
**BC1.[34]** Tsai SW, Hahn HT (1980) Introduction to composite materials. Technomic, Lancaster
**[BC1.35]** Goetschel DB, Radford DW (1997) Analytical development of through-thickness properties of composite laminates. J AdvMater 28(4):37–46
**[BC1.36]** Ersoy N, Tugutlu M (2010) Cure kinetics modelling and cure shrinkage behaviour of a thermosetting composite. Polym Eng Sci 50(1):84–92
**[BC1.37]** Monti M, Puglia D, Natali M, Torre L, Kenny JM (2011) Effectof carbon nanofibers on the cure kinetics of unsaturated polyester resin: thermal and chemorheological modelling. Compos Sci Technol 71:1507–1516
**[BC1.38]** Kosar V, Gomzi Z (2001) Thermal effects of cure reaction for an unsaturated polyester in cylindrical moulds. Chem Biochem Eng Q 15(3):101–108
**[BC1.39]** Martin JL, Cadenato A, Salla JM (1997) Comparative studies on the non-isothermal DSC curing kinetics of an unsaturated polyester resin using free radicals and empirical models. Thermochim Acta 306:115–126
**[BC1.40]** De la Caba K, Guerrero P, Mondragon I, Kenny JM (1998) Comparative study by and DSC FTIR techniques of an unsaturated polyester resin cured at different temperatures. Polym Int 45:333–338
**[BC1.41]** Avella M, Martuscelli E, Mazzola M (1985) Kinetic study of the cure reaction of unsaturated polyester resins. J Therm Anal 30:1359–1366
**[BC1.42]** Vilas JL, Laza JM, Garay MT, Rodriguez M, Leon LM (2001) Unsaturated polyester resins cure: kinetic, rheologic, and mechanical-dynamical analysis. I. Cure kinetics by DSC and TSR. J Appl Polym Sci 79:447–457
**[BC1.43]** Kenny JM (1994) Determination of autocatalytic kinetic model parameters describing thermoset cure. J Appl Polym Sci 51:761–764
**[BC1.44]** Kessler MR, White SR (2002) Cure kinetics of the ring-opening metathesis polymerization of dicyclopentadiene. J Poly Sci A Poly Chem 40:2373–2383
**[BC1.45]** Baran I, Akkerman R, Hattel JH (2014) Material characterization of a polyester resin system for the pultrusion process. Compos B Eng 64:194–201
**[BC1.46]** Chachad YR, Roux JA, Vaughan JG, Arafat E (1995) Threedimensional characterization of pultruded fiberglass-epoxy composite materials. J Reinf Plast Comp 14:495–512
**[BC1.47]** Valliappan M, Roux JA, Vaughan JG, Arafat ES (1996) Die and post-die temperature and cure in graphite-epoxy composites. Compos Part B Eng 27:1–9

**[BC1.48]** Khoun L, Centea T, Hubert P (2010) Characterization methodology of thermoset resins for the processing of composite materials - case study: CYCOM 890RTM epoxy resin. J Compos Mater 44:1397–1415
**[BC1.49]** Khoun L (2009) Process-induced stresses and deformations in woven composites manufactured by resin transfer moulding. Ph.D. thesis, McGill University, Montreal
**[BC1.50]** Nielsen MW (2012) Predictions of process induced shape distortions and residual stresses in large fibre reinforced composite laminates, Ph.D. thesis, Technical University of Denmark, Lyngby, Denmark
**[BC1.51]** White SR, Hahn HT (1992) Process modelling of composite materials: residual stress development during cure. Part II.Experimental validation. J Compos Mater 26(16):2423–2453
**[BC1.52]** Russell JD, Madhukar MS, Genidy MS, Lee AY (2000) A new method to reduce cure-induced stresses in thermoset polymer composites, part III: correlating stress history to viscosity, degree of cure, and cure shrinkage. J Compos Mater 34(22):1926–1947
**[BC1.53]** Msallem YA, Jacquemin F, Boyard N, Poitou A, Delaunay D, Chatel S (2010) Material characterization and residual stresses simulation during the manufacturing process of epoxy matrix composites. Compos A 41:108–115
**[BC1.54]** Prasatya P, McKenna GB, Simon SL (2001) A viscoelastic model for predicting isotropic residual stresses in thermosetting materials: effects of processing parameters. J Compos Mater 35(10):826–847
**[BC1.55]** Madhukar MS, Genidy MS, Russell JD (2000) A new method to reduce cure-induced stresses in thermoset polymer composites, part I:test method. J Compos Mater 34(22):1882–1904
**[BC1.56]** DA Darrow JR, Smith LV (2001) Isolating components of processing induced warpage in laminated composites. J Compos Mater 36(21):2407–2418
**[BC1.57]** Hsiao KT, Gangireddy S (2008) Investigation on the spring-in phenomenon of carbon nanofibre-glass fibre/polyester composites manufactured with vacuum assisted resin transfer moulding. Compos A 39:834–842
**[BC1.58]** Wisnom MR, Ersoy N, Potter KD (2007) Shear-lag analysis of the effect of thickness on spring-in of curved composites. J Compos Mater 41(11):1311–1324
**[BC1.59]** Ersoy N, Garstka T, Potter K, Wisnom MR, Porter D, Stringer G (2010) Modelling of the spring-in phenomenon in curved parts made of a thermosetting composite. Compos A 41:410–418
**[BC1.60]** Hubert P, Vaziri R, Poursartip A (1999) A two-dimensional flow model for the process simulation of complex shape composite laminates. Int J Numer Meth Eng 44(1):1–26
**[BC1.61]** Min L, Yanxia L, Yizhuo G (2008) Numerical simulation flow and compaction during the consolidation of laminated composites. Wiley Intersci Soc Plast Eng 29(5):560–568
**[BC1.62]** Dave R, Kardos JL, Dudukovic MP (1987) A model for resin flow during composite processing: part 1-general mathematical development. Polym Compos 8(1):29–38
**[BC1.63]** Gutowski TG, Cai Z, Bauer S, Boucher D (1987) Consolidation experiments for laminate composites. J Compos Mater 21(7):650–669
**[BC1.64]** Li M, Li Y, Zhang Z, Gu Y (2008) Numerical simulation flow and compaction during the consolidation of laminated composites. Polym Compos 29(5):560–568
**[BC1.65]** Li M, Charles L, Tucker III (2002) Modelling and simulation of two-dimensional consolidation for thermoset matrix composites. Compos A 33:877–892
**[BC1.66]** Dong C (2011) Model development for the formation of resinrich zones in composites processing. Compos A 42:419–424
**[BC1.67]** Svanberg JM (2002) Predictions of manufacturing induced shape distortions-high performance thermoset composites. PhD thesis, Lulea University of Technology
**[BC1.68]** Johnston A, Vaziri R, Poursartip A (2001) A plane strain model for process-induced deformation of laminated composite structures. J Compos Mater 35(16):1435–1469
**[BC1.69]** Ersoy N, Potter K, Wisnom MR, Clegg MJ (2005) An experimental method to study frictional processes during composite manufacturing. Compos A 36:1536–1544

**[BC1.70]** Kim YK (2004) Process-induced residual stress analysis by resin transfer molding. J Compos Mater 38(11):959–972
**[BC1.71]** Kim YK, White SR (1996) Stress relaxation behavior of 3501–6 epoxy resin during cure. Polym Eng Sci 36(23):2852–2862
**[BC1.72]** Kim YK, White SR (1997) Viscoelastic analysis of processing induced residual stresses in thick composite laminates. Mech Compos Mater Struct 4(4):361–387
**[BC1.73]** 98. White SR, Kim YK (1998) Process-induced residual stress analysis of AS4/3501-6 composite material. Mech Compos Mater Struct Int J 5(2):153–186
**[BC1.74]** 99. Kim YK, White SR (1999) Cure-dependent viscoelastic residual stress analysis of filament-wound composite cylinders. Mech Compos Mater Struct 5(4):327–354
**[BC1.75]** 100. Ding A, Li S, Wang J, Zu L (2015) A three-dimensional thermos-viscoelastic analysis of process-induced residual stress in composite laminates. Compos Struct 129:60–69
**[BC1.76]** 101. Ding A, Li S, Sun J, Wang J, Zu L (2015) A thermo-viscoelastic model of process-induced residual stresses in composite structures with considering thermal dependence. Compos Struct. doi:10.1016/j.compstruct.2015.09.014
**[BC1.77]** 102. Zobeiry N (2006) Viscoleastic constitutive models for evaluation of residual stresses in thermoset composites during cure. PhD thesis, The University of British Columbia
**[BC1.78]** 103. ZocherMA(1995)AThermoviscoelastic finite element formulation for the analysis of composites. PhD. thesis, Texas AM University
**[BC1.79]**Svanberg JM, Altkvist C, Nyman T (2005) Prediction of shape distortions for a curved composite C-spar. J Reinf Plast Compos 24(3):323–339
**[BC1.80]** Svanberg JM, Holmberg JA (2004) Prediction of shape distortions. Part II. Experimental validation and analysis of boundary conditions. Compos A 35:723–734
**[BC1.81]** Cinar K, Oztrk UE, Ersoy N, Wisnom MR (2014) Modelling manufacturing deformations in corner sections made of composite materials. J Compos Mater 48(7):799–813
**[BC1.82]** Cinar K (2014) Process modelling for distortions in manufacturing of fibre reinforced composite materials. Ph.D. thesis, Bogazici University
**[BC1.83]** Arafath ARA, Vaziri R, Poursartip A (2008) Closed-from solution for process-induced stresses and deformation of a composite part cured on a solid tool: Part I- flat geometries. Compos A 39:1106–1117
**[BC1.84]** Arafath ARA, Vaziri R, Poursartip A (2009) Closed-from solution for process-induced stresses and deformation of a composite part cured on a solid tool: Part II- curved geometries. Compos A 40:1545–1557
**[BC1.85]** Ferlund G, Rahman N, Courdji R, Bresslauer M, Poursartip A, Willden K, Nelson K (2002) Experimental and numerical study of the effect of cure cycle, tool surface, geometry, and lay-up on the dimensional fidelity of autoclave-processed composite parts. Compos A 33:341–351
**[BC1.86]** Zhu Q, Geubelle PH, Li M, Tucker CL (2001) Dimensional accuracy of thermoset composites: simulation of process-induced residual stresses. J Compos Mater 35(24):2171–2205
**[BC1.87]** Flanagan R (1997) The dimensional stability of composite laminates and structures. Ph.D. thesis, Queen's University of Belfast
**[BC1.88]** Ozsoy OO, Ersoy N, Wisnom MR (2007) Numerical Investigation of tool-part interactions in composite manufacturing. Proceedings of ICCM-16
**[BC1.89]** Twigg G, Poursartip A, Ferlund G (2004) Tool-part Interaction in composite processing. Part II: numerical modelling. Compos A 35:135–141
**[BC1.90]** Sun J, Gu Y, Li Y, Li M, Zhang Z (2012) Role of tool-part interaction in consolidation of L-shaped laminates during autoclave process. Appl Compos Mater 19(3):583–597
**[BC1.91]** 118. Hibbit, Karlson, Sorensen Inc. (2004) ABAQUS online documentation, version 6.5.1
**[BC1.92]** Twigg G, Poursartip A, Ferlund G (2003) An experimental method for quantifying tool-part shear interaction during composites processing. Compos Sci Technol 63:1985–2002
**[BC1.93]** Twigg G, Poursartip A, Ferlund G (2004) Tool-part interaction in composite processing. Part I: experimental investigation and analytical model. Compos A 35:121–133

**[BC1.94]** Potter KD, Campbell M, Langer C, Wisnom MR (2005) The generation of geometrical deformations due to tool/part interaction in the manufacture of composite components. Compos A 36:301–308
**[BC1.95]** Kappel E, Stefaniak D, Sprowitz T, Hhne C (2011) A semianalytical simulation strategy and its application to warpage of autoclave-processed CFRP parts. Compos A 42:1985–1994
**[BC1.96]** Stefaniak D, Kappel E, Sprowitz T, Hhne C (2012) Experimental identification of process parameters inducing warpage of autoclave-processed CFRP parts. Compos A 43:1081–1091
**[BC1.97]** Zeng X, Raghavan J (2010) Role of tool-part interaction in process-induced warpage of autoclave-manufactured composite structures. Compos A 41:1174–1183
**[BC1.98]** Kaushik V, Raghavan J (2010) Experimental study of tool-part interaction during autoclave processing of thermoset polymer composite structures. Compos A 41:1210–1218
**[BC1.99]** de Oliveria R, Lavanchy S, Chatton R, Costantini D, Michaud V, Salathe R, Manson JAE (2008) Experimental investigation of the mould thermal expansion on the development of internal stresses during carbon fibre composite processing. Compos A 39:1083–1090
**[BC1.100]** Potter K, Campbell M, Wisnom MR (2003) Investigation of tool/part interaction effects in the manufacture of composite components. Proceedings of ICCM-14
**[BC1.101]** Kim YK, Daniel IM (2002) Cure cycle effect on composite structures manufactured by resin transfer moulding. J Compos Mater 36(14):1725–1742
**[BC1.102]** Antonucci V, Cusano A, Giordano M, Nasser J, Nicolais L (2006) Cure- induced residual strain build-up in a thermoset resin. Compos A 37:592–601
**[BC1.103]** Martin CJ, Seferis JC, Wilhelm MA (1996) Frictional resistance of thermoset prepregs and its influence on honeycomb composite processing. Compos A 27:943–951

# 2. CURRENT STATE OF EXPERIMENTAL RESEARCH ON THE PREDICTION OF GEOMETRIC DISTORTIONS INDUCED BY RESIDUAL STRESSES GENERATED IN THE FABRICATION OF MULTILAYERED ANISOTROPIC STRUCTURES

In the specialized literature, three categories of experimental approaches are highlighted, aiming to quantify the effects of the interaction at the matrix-component interface level. These experimental methods aim to adjust numerical models simulating residual stresses by monitoring the polymerization process, as well as by monitoring deformations, the evolution of residual stresses, and the post-polymerization geometry.

## 2.1 EXPERIMENTAL INVESTIGATIONS OF THE TOOL-PART INTERACTION

The effect of the interaction between the matrix and the component on distortions has been highlighted in recent studies [***BC2.1-BC2.24***]. Twig et al. [***BC2.11, BC2.14, BC2.15***] conducted experiments to understand the mechanical behavior of the matrix-component interface. An experimental method was used to examine the interaction between the component and the matrix. To define the critical shear stress at which slippage occurs at the interface, the following expression was used:

$$\tau_{cr} = \mu \cdot P \tag{2.1}$$

The friction coefficients during the polymerization process have been measured in other studies as well [***BC2.9, BC2.18, BC2.24***]. Martin et al. [***BC2.24***] and Flanagan et al. [***BC2.9***] measured only the static friction values (without slippage) over the temperature increase interval of the cycle. Their observations [***BC2.4, BC2.24***] indicated that the matrix-component interface undergoes changes throughout the polymerization cycle. In [***BC2.19***], both static and dynamic friction coefficients were measured as a function of the degree of cure and the rate of temperature increase [***BC2.9, BC2.19***]. A nonlinear relationship was observed between the static and dynamic friction coefficients and the degree of cure. This suggested that at the interface, conditions transition from motion (slippage) in the early stages of the manufacturing cycle to the complete cessation of any slippage and fixation (adhesion, "sticking," etc.). A mathematical model for friction was developed [***BC2.26***] to evaluate the friction forces between a polypropylene-based composite reinforced with glass fiber (Twintex) and a rigid mold at the melting temperature.

## 2.2 EXPERIMENTAL MONITORING OF THE CURING PROCESS

### 2.2.1 OPTICAL SENSORS

Fiber optic monitoring systems are capable of detecting various parameters and can be integrated into fiber-reinforced laminated materials to monitor the curing process during the manufacturing stage. These same sensors can also be used to measure temperature and

deformations throughout the service life of the structure. Refractive index sensors have been successfully tested for monitoring the curing process of thermosetting resin-based composites. In fact, they can be utilized in manufacturing stages that involve changes in density, chemical alterations, or phase transitions.
The use of FBG (Fiber Bragg Grating) technology allows for extremely useful and precise qualitative and quantitative results when measuring distributed deformations and temperature, compared to conventional measurement and monitoring systems.

### 2.2.2 DIRECT CURRENT DIELECTRIC SENSORS (DC)

The experimental analysis with dielectric sensors is a widely used technique in the composite structure manufacturing industry because it is a very robust method for characterizing the state of the resin during the fabrication process. The monitoring method using dielectric sensors is based on the presence of dipoles in the resin in its unpolymerized state. At the beginning of the curing reaction, the monomers can move freely. As the curing reaction progresses, the monomers form polymer chains, and the mobility of the dipoles is restricted until the gelation point, at which a complex cross-linked polymer network (A+B) is formed, and the mobility of the formed polymers tends to zero.
From this point onwards, the rate at which the parameter $\alpha$ (degree of cure) increases drastically decreases, and the measured electrical resistance stabilizes, thus marking the end of the curing reaction from a DC sensor recording standpoint. In this way, a DC sensor is able to indirectly measure the evolution of the thermosetting resin and its degree of curing by monitoring the variation in resistivity. However, to accurately quantify the degree of cure ($\alpha$), it is necessary to analyze the thermal evolution of the process in order to correlate the sensor signal with the evolution of the $\alpha$ parameter.

## 2.3 EXPERIMENTAL DETERMINATIONS OF GEOMETRIC CHANGES

Distortion measurements, in general, and "spring-in" angles in particular, are typically performed using optical methods such as laser scanning or by using coordinate measuring machines (CMM). Distortion measurement is an operation that requires high-performance measuring equipment to provide high-precision information for both adjusting the geometry of molds and, most importantly, for the calibration steps of numerical simulations of the curing processes. These measurements are crucial for validating and fine-tuning the manufacturing process, ensuring the final product meets the desired specifications without geometric defects.

Figure 2.8 presents a summary of the results obtained from measurements using both optical methods and CMM. To assess the global distortions for the manufactured specimens, measurements are taken of the mold that will be used to manufacture the U-profile specimen. The results of the optical inspection can be seen in images a and b of Figure 2.1.

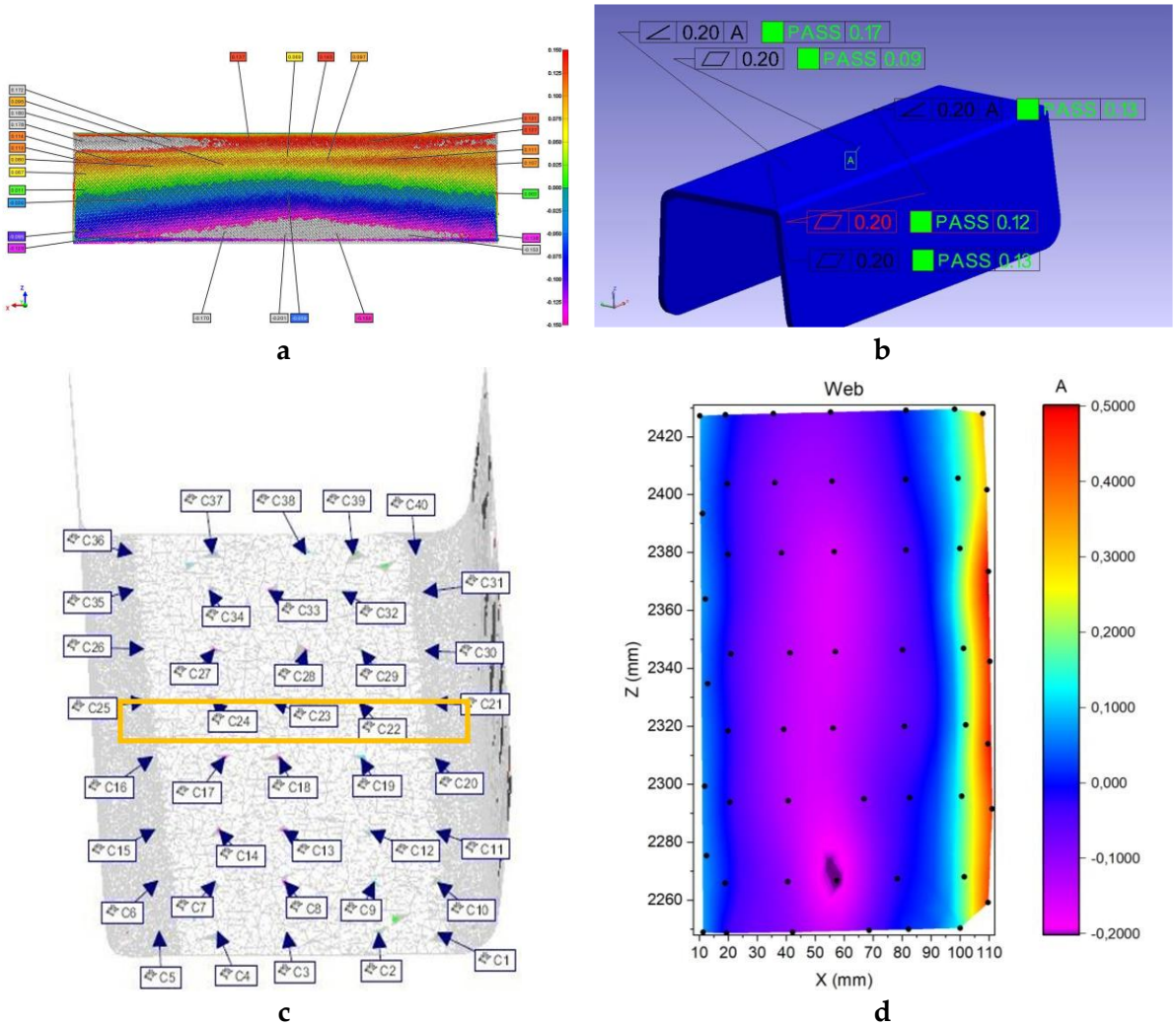


**Figure 2.1**. *Measurements on molds and specimens:* ***a)*** *Geometric scanning of the mold with the PolyWorks optical system;* ***b)*** *Geometric scanning of the mold with the FARO Laser Tracker optical system;* ***c)*** *U-profile specimen measured with the CMM method – measurement points;* ***d)*** *Dimensional deviation map of the U-profile specimen.*

## 2.4 EX-SITU MEASUREMENTS AND EVALUATIONS

A category of material property evaluations that is well-established in the scientific and engineering world is that of material evaluations to accurately determine information of interest. Unlike methods that use sensors, these latter methods, by their nature, cannot be used during the manufacturing of composite structures or specimens. Ex-situ methods for evaluating material properties are not directly relevant for assessing the course of curing processes and the distribution of residual stresses that lead to geometric distortions of layered composites, which is why we will not go into the technical details of these methods. However, in the numerous cases where sensors are used to monitor the dynamics of curing and to provide information at key moments of the process, sensor readings require, as a mandatory step, referencing and calibration. Therefore, sensor calibration is typically done through ex-situ evaluation methods.

## REFERENCES CHAPTER 2

**[BC2.1]** Johnston A (1997) An integrated model of the development of process-induced deformation in autoclave processing of composite structures. Ph.D. thesis, The University of British Columbia
**[BC2.2]** Johnston A, Vaziri R, Poursartip A (2001) A plane strain model for process-induced deformation of laminated composite structures. J Compos Mater 35(16):1435–1469
**[BC2.3]** Khoun L, Hubert P (2010) Investigation of the dimensional stability of carbon epoxy cylinders manufactured by resin transfer moulding. Compos A 41:116–124
**[BC2.4]** Ersoy N, Potter K, Wisnom MR, Clegg MJ (2005) An experimental method to study frictional processes during composite manufacturing. Compos A 36:1536–1544
**[BC2.5]** Arafath ARA, Vaziri R, Poursartip A (2008) Closed-from solution for process-induced stresses and deformation of a composite part cured on a solid tool: Part I- flat geometries. Compos A 39:1106–1117
**[BC2.6]** Arafath ARA, Vaziri R, Poursartip A (2009) Closed-from solution for process-induced stresses and deformation of a composite part cured on a solid tool: Part II- curved geometries. Compos A 40:1545–1557
**[BC2.7]** Ferlund G, Rahman N, Courdji R, Bresslauer M, Poursartip A, Willden K, Nelson K (2002) Experimental and numerical study of the effect of cure cycle, tool surface, geometry, and lay-up on the dimensional fidelity of autoclave-processed composite parts. Compos A 33:341–351
**[BC2.8]** Zhu Q, Geubelle PH, Li M, Tucker CL (2001) Dimensional accuracy of thermoset composites: simulation of process-induced residual stresses. J Compos Mater 35(24):2171–2205
**[BC2.9]** Flanagan R (1997) The dimensional stability of composite laminates and structures. Ph.D. thesis, Queen's University of Belfast
**[BC2.10]** Ozsoy OO, Ersoy N, Wisnom MR (2007) Numerical Investigation of tool-part interactions in composite manufacturing. Proceedings of ICCM-16
**[BC2.11]** Twigg G, Poursartip A, Ferlund G (2004) Tool-part Interaction in composite processing. Part II: numerical modelling. Compos A 35:135–141
**[BC2.12]** Sun J, Gu Y, Li Y, Li M, Zhang Z (2012) Role of tool-part interaction in consolidation of L-shaped laminates during autoclave process. Appl Compos Mater 19(3):583–597
**[BC2.13]** Twigg G, Poursartip A, Ferlund G (2003) An experimental method for quantifying tool-part shear interaction during composites processing. Compos Sci Technol 63:1985–2002
**[BC2.14]** Twigg G, Poursartip A, Ferlund G (2004) Tool-part interaction in composite processing. Part I: experimental investigation and analytical model. Compos A 35:121–133
**[BC2.15]** Potter KD, Campbell M, Langer C, Wisnom MR (2005) The generation of geometrical deformations due to tool/part interaction in the manufacture of composite components. Compos A 36:301–308
**[BC2.16]** Kappel E, Stefaniak D, Sprowitz T, Hhne C (2011) A semianalytical simulation strategy and its application to warpage of autoclave-processed CFRP parts. Compos A 42:1985–1994
**[BC2.17]** Stefaniak D, Kappel E, Sprowitz T, Hhne C (2012) Experimental identification of process parameters inducing warpage of autoclave-processed CFRP parts. Compos A 43:1081–1091
**[BC2.18]** Zeng X, Raghavan J (2010) Role of tool-part interaction in process-induced warpage of autoclave-manufactured composite structures. Compos A 41:1174–1183
**[BC2.19]** Kaushik V, Raghavan J (2010) Experimental study of tool-part interaction during autoclave processing of thermoset polymer composite structures. Compos A 41:1210–1218
**[BC2.20]** de Oliveria R, Lavanchy S, Chatton R, Costantini D, Michaud V, Salathe R, Manson JAE (2008) Experimental investigation of the mould thermal expansion on the development of internal stresses during carbon fibre composite processing. Compos A 39:1083–1090
**[BC2.21]** Potter K, Campbell M, Wisnom MR (2003) Investigation of tool/part interaction effects in the manufacture of composite components. Proceedings of ICCM-14
**[BC2.22]** Kim YK, Daniel IM (2002) Cure cycle effect on composite structures manufactured by resin transfer moulding. J Compos Mater 36(14):1725–1742

**[BC2.23]** Antonucci V, Cusano A, Giordano M, Nasser J, Nicolais L (2006) Cure- induced residual strain build-up in a thermoset resin. Compos A 37:592–601
**[BC2.24]** Martin CJ, Seferis JC, Wilhelm MA (1996) Frictional resistance of thermoset prepregs and its influence on honeycomb composite processing. Compos A 27:943–951
**[BC2.25]** Garstka T (2005) Separation of process induced distortions in curved composite laminates. Ph.D. thesis, University of Bristol
**[BC2.26]** ten Thije RHW, Akkerman R, Ubbink M, van der Meer L (2011) A lubrication approach to friction in thermoplastic composites forming processes. Compos A Appl Sci Manuf 42(8):950–960
**[BC2.27]** Sachs U, Akkerman R, Fetfatsidis K, Vidal-Sall E, Schumacher J et al (2014) Characterization of the dynamic friction of woven fabrics: experimental methods and benchmark results. Compos A Appl Sci Manuf 67:289–298
**[BC2.28]** Cornelissen B, Sachs U, Rietman B, Akkerman R (2014) Dry friction characterisation of carbon fibre tow and satin weave fabric for composite applications. Compos A Appl Sci Manuf 56:127–135
**[BC2.29]** Cusano, A., Breglio, et al. Multifunction fiber optic sensing system for smart applications. IEEE/ASME Trans. Mechatronics (2004)
**[BC2.30]** García, I. et al. Optical fiber sensors for aircraft structural health monitoring. Sensors (Switzerland) (2015)
**[BC2.31]** Kuang, K. S. C., et al. Embedded fibre Bragg grating sensors in advanced composite materials. Compos. Sci. Technol. (2001)
**[BC2.32]** Kahandawa, G. C., et al. Use of FBG sensors for SHM in aerospace structures. Photonic Sensors (2012)
**[BC2.33]** Takagaki K, Minakuchi S and Takeda N. 2017 *Compos. Part A Appl. Sci,* **103**, 236-251
**[BC2.34]** Zhang G, Zhou Z, Ding G, Xu S, Xie C and Zhang J 2015 Materials Research Innovations, 19, S5-718,
**[BC2.35]** Chaloupka A, Pflock T., Horny R., Rudolph N and Horn S R 2018 *J. Polym. Sci. Part B: Polym. Phys.* **56**: 907-913
**[BC2.36]** A. Chaloupka, T. Pflock, R. Horny, N. Rudolph, S.R. Horn, Dielectric and rheological study of the molecular dynamics during the cure of an epoxy resin, J. Polym. Sci., Part B: Polym. Phys. 56 (2018) 907–913, https://doi.org/10.1002/ polb.24604.
**[BC2.37]** R. Hardis, J.L. Jessop, F.E. Peters, M.R. Kessler, Cure kinetics characterization and monitoring of an epoxy resin using DSC, Raman spectroscopy, and DEA, Compos. Appl. Sci. Manuf. 49 (2013) 100–108, https://doi.org/10.1016/j. compositesa.2013.01.021
**[BC2.38]** M. Demleitner, S.A. Sanchez-Vazquez, D. Raps, G. Bakis, T. Pflock, A. Chaloupka, S. Schmolzer, ¨ V. Altst¨ adt, Dielectric analysis monitoring of thermoset curing with ionic liquids: from modeling to the prediction in the resin transfer molding process, Polym. Compos. 40 (2019) 4500–4509, https://doi.org/10.1002/ pc.25306.
**[BC2.39]** ] J.-P. Pascault, Thermosetting Polymers, Marcel Dekker, New York, 2002.
**[BC2.40] ]** H.L. Lee, Handbook of Dielectric Analysis and Cure Monitoring, Lambient Technologies, 2017**.**
**[BC2.41]** N.W. Radebe, C. Fengler, C.O. Klein, R. Figuli, M. Wilhelm, -I.R. Rheo, A combined setup for correlating chemical changes via FTIR spectroscopy and rheological properties in a strain-controlled rheometer, J. Rheol. 65 (2021) 681–693, https://doi.org/10.1122/8.0000251.
**[BC2.42]** M. Kempf, B. Dippel, O. Arnolds, Hyphenation of Rheology and Raman Spectroscopy - Investigation of Epoxy Curing Mechanism and Polyethylene Crystallization, ANNUAL TRANSACTIONS OF THE NORDIC RHEOLOGY SOCIETY, 2017, pp. 181–187
**[BC2.43]** N. Liebers, F. Raddatz, et al., Effective and Flexible Ultrasound Sensors for Cure Monitoring for Industrial Composite Production, Deutscher Luft- und Raumfahrtkongress, 2012.
**[BC2.44]** H.E. Adabbo, R.J.J. Williams, The evolution of thermosetting polymers in a conversion–temperature phase diagram, J. Appl. Polym. Sci. 27 (1982) 1327–1334, https://doi.org/10.1002/app.1982.070270422

**[BC2.45]** J.M. Svanberg, J.A. Holmberg., An experimental investigation on mechanisms for manufacturing induced shape distortions in homogenous and balanced laminates., Composites: Part A 32 (2001), 827-838
**[BC2.46]** Y.K. Kim, S.R. White, Stress relaxation behavior of 3501-6 epoxy resin during cure, Polym. Eng. Sci. 36 (1996) 2852–2862, https://doi.org/10.1002/ pen.10686
**[BC2.47]** A. Courtois, M. Hirsekorn, M. Benavente, A. Jaillon, L. Marcin, E. Ruiz, M. L´evesque, Viscoelastic behavior of an epoxy resin during cure below the glass transition temperature: characterization and modeling, J. Compos. Mater. 53 (2019) 155–171, https://doi.org/10.1177/0021998318781226
**[BC2.48]** D.J. O'Brien, P.T. Mather, S.R. White, Viscoelastic properties of an epoxy resin during cure, J. Compos. Mater. 35 (2001) 883–904, https://doi.org/10.1177/ a037323
**[BC2.49]** S. Saseendran, M. Wysocki, J. Varna, Evolution of viscoelastic behavior of a curing LY5052 epoxy resin in the glassy state, Adv. Manuf. Polym. Compos. Sci. 2 (2016) 74–82, https://doi.org/10.1080/20550340.2016.1236223
**[BC2.50]** M. Zarrelli, A.A. Skordos, I.K. Partridge, Thermomechanical analysis of a toughened thermosetting system, Mech. Compos. Mater. 44 (2008) 181–190, https://doi.org/10.1007/s11029-008-9009-x
**[BC2.51]** D.J. O'Brien, N.R. Sottos, S.R. White, Cure-dependent viscoelastic Poisson's ratio of epoxy, Exp. Mech. 47 (2007) 237–249, https://doi.org/10.1007/s11340-006- 9013-9
**[BC2.52]** S.R. White, P.T. Mather, M.J. Smith, Characterization of the cure-state of DGEBADDS epoxy using ultrasonic, dynamic mechanical, and thermal probes, Polym. Eng. Sci. 42 (2002) 51–67, https://doi.org/10.1002/pen.10927
**[BC2.53]** D. Dykeman, Minimizing Uncertainty in Cure Modeling for Composites Manufacturing, PhD Thesis, 2008. Vancouver
**[BC2.54]** R. Hardis, J.L. Jessop, F.E. Peters, M.R. Kessler, Cure kinetics characterization and monitoring of an epoxy resin using DSC, Raman spectroscopy, and DEA, Compos. Appl. Sci. Manuf. 49 (2013) 100–108, https://doi.org/10.1016/j. compositesa.2013.01.021
**[BC2.55]** F. Henning, L. Karger, ¨ D. Dorr, ¨ F.J. Schirmaier, J. Seuffert, A. Bernath, Fast processing and continuous simulation of automotive structural composite components, Compos. Sci. Technol. 171 (2019) 261–279, https://doi.org/ 10.1016/j.compscitech.2018.12.007
**[BC2.56]** C. Block, B. van Mele, P. van Puyvelde, G. van Assche, Time–temperaturetransformation (TTT) and temperature–conversion-transformation (TxT) cure diagrams by RheoDSC: combined rheometry and calorimetry on an epoxy-amine thermoset, React. Funct. Polym. 73 (2013) 332–339, https://doi.org/10.1016/j. reactfunctpolym.2012.05.009
**[BC2.57]** M. Müller, A. Winkler, M. Gude, H. J¨ ager, Aspects of reproducibility and stability for partial cure of epoxy matrix resin, J. Appl. Polym. Sci. 137 (2020), 48342, https://doi.org/10.1002/app.48342
**[BC2.58]** R.S. Lakes, Viscoelastic measurement techniques, Rev. Sci. Instrum. 75 (2004) 797–810, https://doi.org/10.1063/1.1651639
**[BC2.59]** I.M. Ward, J. Sweeney, Mechanical Properties of Solid Polymers, third. ed., Wiley, Chichester, 2013
**[BC2.60]** R.A. Venditti, J.K. Gillham, Y.C. Jean, Y. Lou, Free volume after cure vs. fractional conversion for a high-Tg epoxy/amine thermosetting system, J. Appl. Polym. Sci. 56 (1995) 1207–1220, https://doi.org/10.1002/ app.1995.070561003
**[BC2.61]** J.B. Enns, J.K. Gillham, Effect of the extent of cure on the modulus, glass transition, water absorption, and density of an amine-cured epoxy, J. Appl. Polym. Sci. 28 (1983) 2831–2846, https://doi.org/10.1002/ app.1983.070280914
**[BC2.62]** F. Lionetto, A. Maffezzoli, Monitoring the cure state of thermosetting resins by ultrasound, Materials 6 (2013) 3783–3804, https://doi.org/10.3390/ ma6093783

# 3. EXPERIMENTAL EVALUATIONS OF GEOMETRIC DISTORTIONS INDUCED BY RESIDUAL STRESSES GENERATED IN THE MANUFACTURING OF ANISOTROPIC MULTILAYER STRUCTURES USED IN THE AEROSPACE INDUSTRY (ANISOTROPIC MULTILAYER STRUCTURES MANUFACTURED THROUGH OOA - OUT OF AUTOCLAVE PROCESSES)

We will propose an experimental monitoring strategy for the manufacturing process and measurements of geometric distortions based on the results highlighted in the second research report regarding the current state of experimental research on residual stresses and the geometric deviations they induce.

Selection of Relevant Specimen Geometries for the Experimental Program

Different types of test specimens will be studied to understand the evolution of the influence of each parameter in the curing process. A generic description of the test specimens is provided in Figure 3.1. The geometry of the test specimens will gradually increase in complexity. In addition to modifying the geometry, the test specimens will also feature different values for the laminate thickness (number of layers). From the perspective of the type of test specimen, the experimental study strategy will be divided into three phases:

- In **Phase 0**, 2D (plane) specimens made solely from resin will be monitored;
- In **Phase 1**, specimens with two geometries will be monitored: one with a very large curvature radius (quasi-plane) and a "U" profile specimen;
- In **Phase 2**, a complex assembly consisting of a skin and the "U" profile will be monitored.

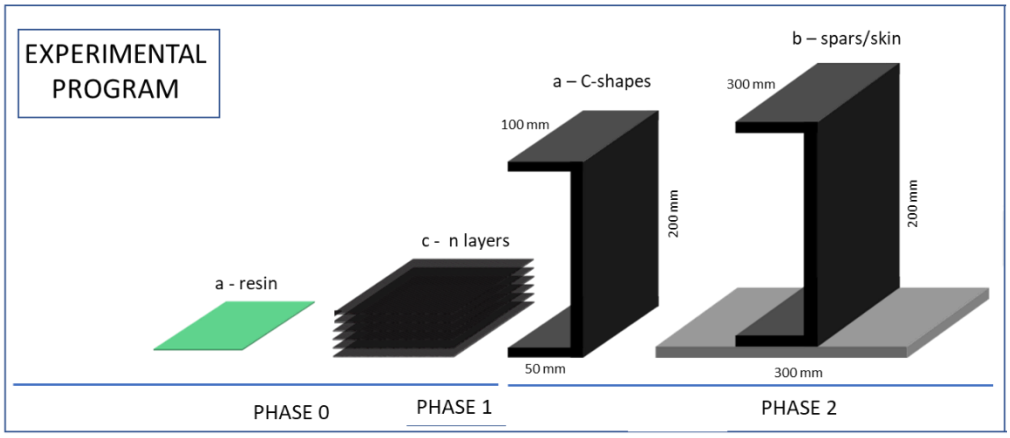


**Figure 3.1**. *The experimental program is described in phases for the test specimens*

*Monitoring with Dielectric Sensors (DC)*

The electrical properties of a polymer matrix can provide information about the state of the polymer, such as viscosity, gel point, glass transition temperature (Tg), and the completion of

the curing process. The goal is to correlate these electrical properties with quality and performance criteria, so that electrical and temperature measurements can be combined with material models to convert them into resin viscosity (η), degree of cure ($\alpha$), or glass transition temperature (Tg). These models can be used offline to determine the optimal curing/manufacturing process cycle [***BC3.1***], but also online, to ensure real-time optimal control of the composite manufacturing process [***BC3.2***].

*Monitoring with FBG Optical Sensors*

The most commonly used optical sensors for process monitoring are FBG sensors, because they: represent the most advanced optical sensor technology, have a lower cost compared to distributed fiber optic sensors, offer high point sensitivity for temperature and strain, feature a low noise-to-signal ratio, which is very advantageous when detecting small magnitude variations (such as strain, temperature), have a short response time, and have excellent multiplexing capability (multiple sensors on the same optical fiber).

## 3.1 TEST SPECIMENS

By conducting experimental studies on different types of specimens, the aim is to understand the influence of each parameter in the curing process on the residual stresses and geometric distortions [***BC3.3-BC3.32***].

A series of key elements were considered in the design and conceptualization of the test specimens:

- Geometric similarity of the specimens with primary aircraft structural elements (reinforced skins, stringer-type reinforcements, ribs, frames, etc.);
- The geometric characteristics of the specimens should help understand the phenomena associated with the curing process—identifying the factors with the greatest influence on the appearance of residual stresses and, consequently, distortions;
- The geometry must be simple enough to effectively repeat a relevant number of experimental trials, but also sufficiently complex to not be limited to the study of simple flat laminated structures and capable of providing comprehensive information for the development of the distortion simulation software tool, covering as wide a range of real process conditions as possible;
- Ensuring the safety of the sensor instrumentation on the specimens, considering that optical sensors can be affected or broken if not placed under favorable conditions, especially outside the specimens;
- Ease and safety of demolding from the molds;
- Refining a practical procedure for embedding sensors into the test specimens to monitor the curing process throughout;
- Calibration and interpretation of the readings from the sensors (signal) during the curing process.

### 3.1.1 PHASE 0

For Phase 0, in the study of resin behavior, a flat specimen was used, as simple as possible, with the focus solely on monitoring the resin and not on the anisotropic behavior of the laminated structures.

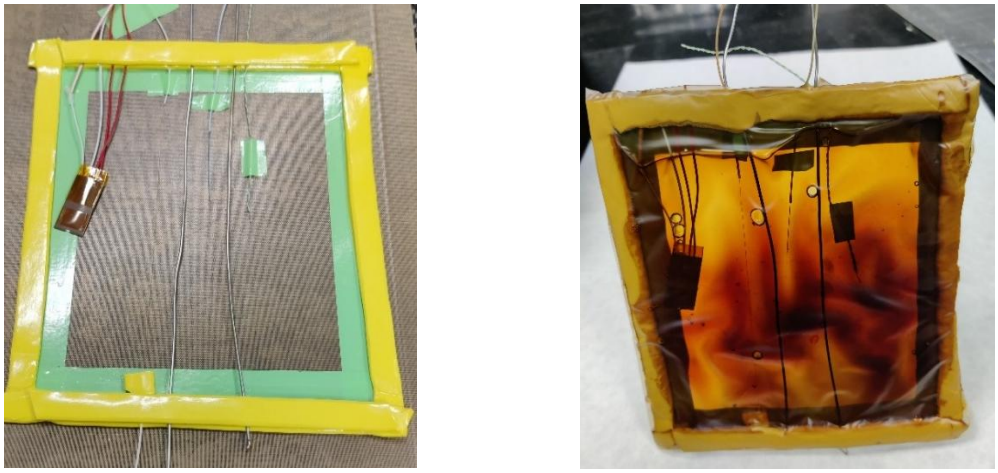

***a*** **b**

**Figure 3.2**. *The setup with sensors in the mold for characterizing the RTM6 resin; (**a**) and the resin cured with embedded sensors (**b**)*

### 3.1.2 PHASE 1

For all the material systems used in the experiments, specimens of lightly curved laminated shell type and specimens with a "U" shape profile were selected as representative geometries for the outer shell (skin) and stringers. The shell-type specimens are shells with a curvature radius of 1475 mm (with a measured edge thickness at the extreme edges of 7.65 mm), considered to best replicate the geometry of a generic wing profile.

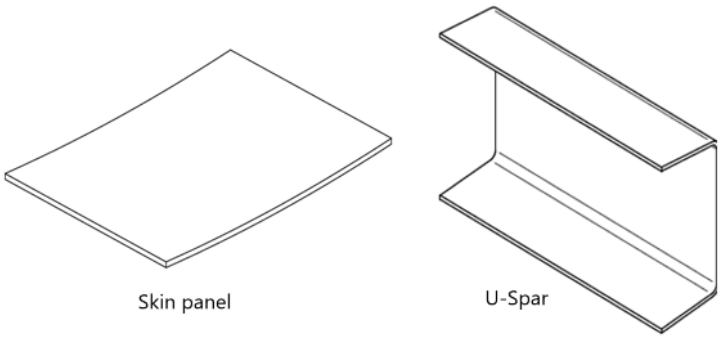


**Figure 3.3**. *Test specimens in PHASE 1*

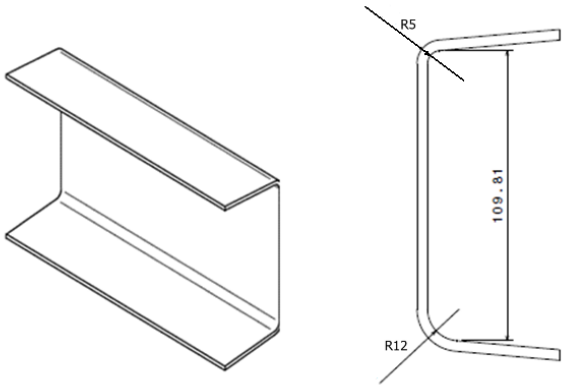


**Figure 3.4**. *U-Spar specimen geometry*

### 3.1.3 PHASE 2

For the second phase of monitoring on test specimens, the possibility of constructing a stiffened shell assembly was studied, with the aim of collecting data on a complex structure at a scale very similar to a section of a primary wing structure.

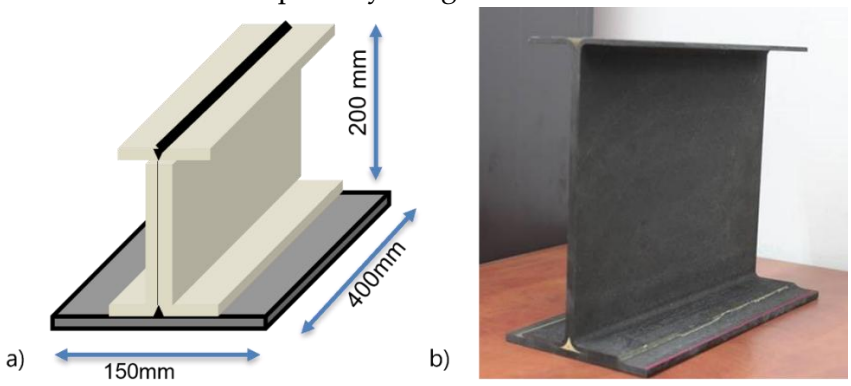


**Figure 3.5**. *FAZA 2 specime – stiffened skin (**a**) design geometry. (**b**) reference specimen.*

## 3.2 SENSOR MONITORING OF THE TEST SPECIMENS

### 3.2.1 PHASE 0

To monitor the behavior of the resin during its polymerization transformation, optical fiber sensors and dielectric sensors (DC) were embedded within it during the consolidation process. Regarding the optical fiber sensors, two types were used: Fiber Bragg Grating (FBG) sensors and distributed optical sensors. The data obtained from the primary analysis of the FBG sensor during these tests are presented in Figure 3.6.

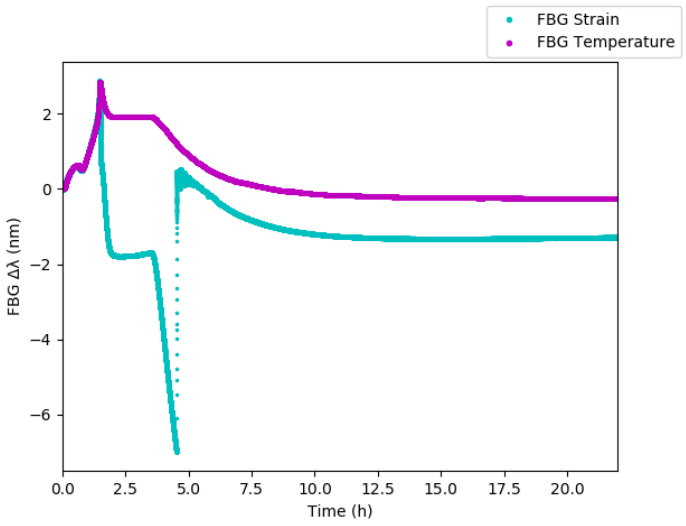


**Figure 3.6**. *Raw data PHASE 0 – RTM6 resin behavior*

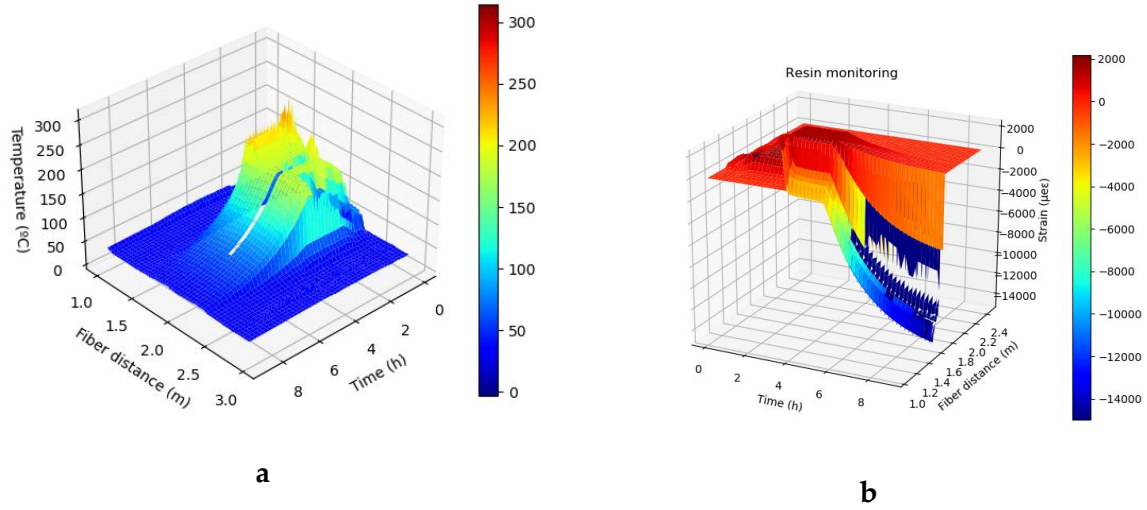


**a** **b**

**Figure 3.7**. *3D maps for (**a**) temperature readings with FBG sensors (**b**) strain variation with fiber distance and time measured by the distributed fiber optics sensor during RTM6 resin curing cycle*

As shown in Figure 3.7 a), the temperature reaches slightly above 200°C, although it is not uniform along the entire measurement line..

### 3.2.2 PHASE 1

The skin specimens with three different thicknesses and the "C" spar specimen with two different thicknesses (Table 1) were manufactured using Liquid Resin Infusion (LRI). The process parameters were monitored using the sensors described in Section 3.1.1.

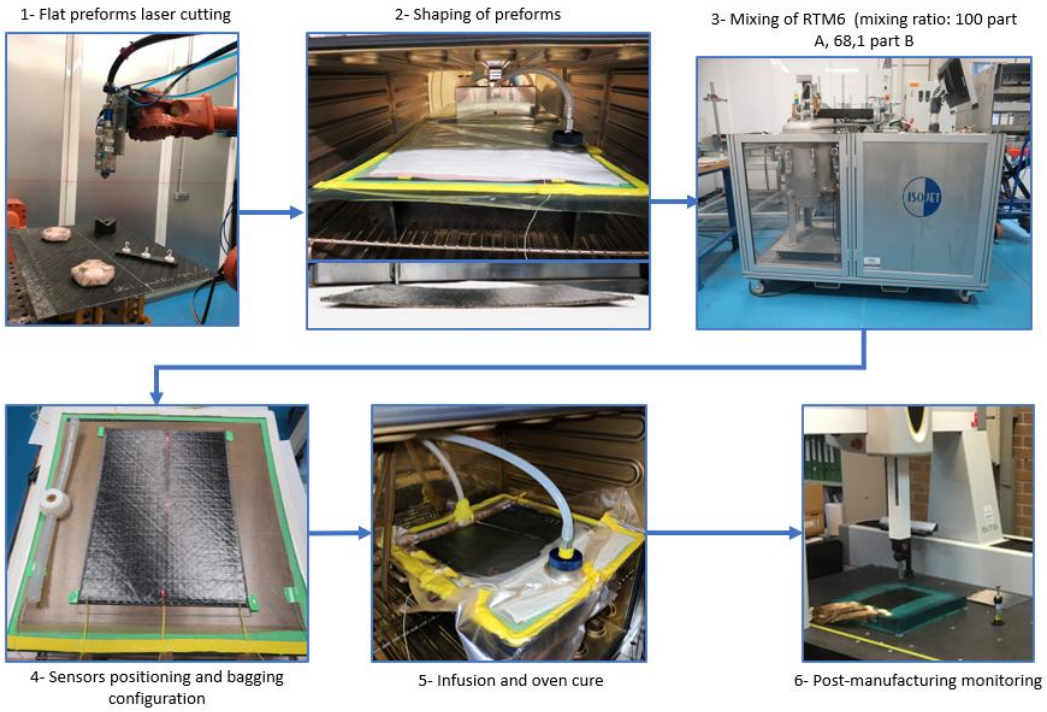


**Figure 3.8**. *Experimental procedure carried out for LRI skin coupons*

The sensor configuration for the skin specimens was designed according to Figure 3.9.

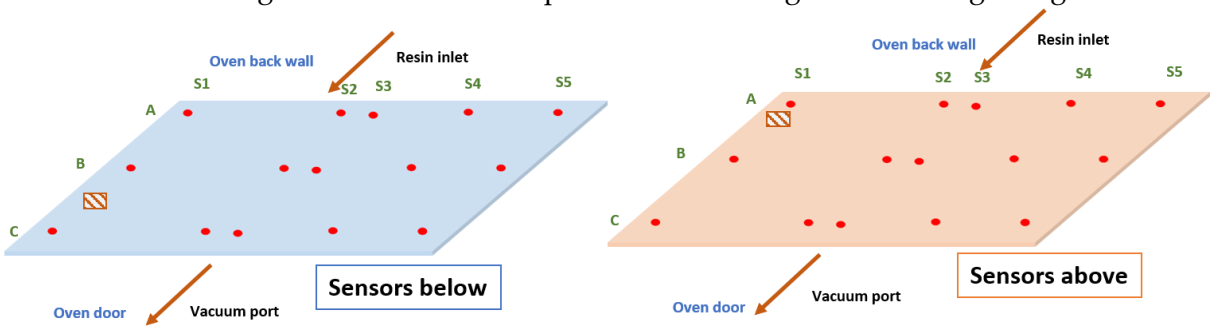


**Figure 3.9**. *Distribution of temperature sensors on shell specimens: FBG sensor (red dots) and DC sensor (square).*

The FBG temperature sensors were placed in networks containing 5 FBG sensors each (one along the imaginary line passing through point A, another through B, and another through C).

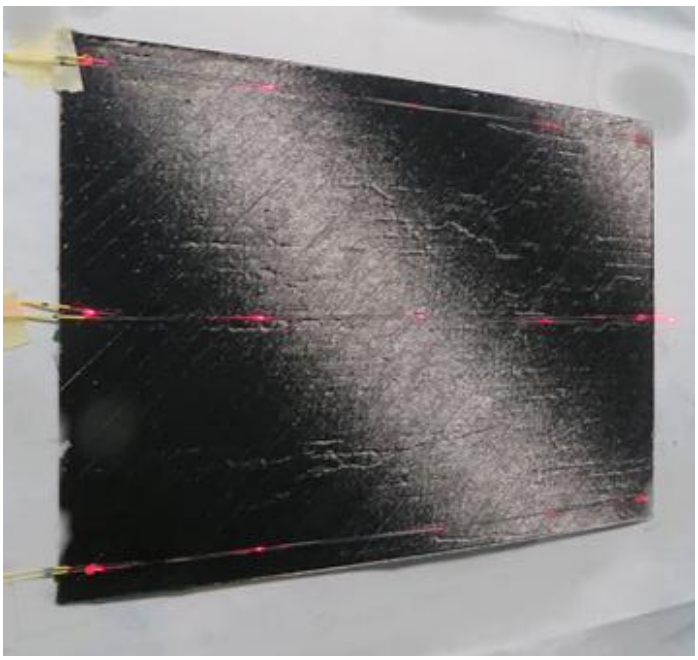

**Figure 3.10**. *Photograph of a skin specimen with 3 networks, each containing 5 FBG sensors for measuring deformation (the illuminated red points represent the locations of the FBG sensors in the optical fiber).*

### *3.2.2.1 Temperature monitoring results*

The temperature profile recorded by the FBG temperature sensors is presented in Figure 3.11. In this graph, the curing cycle has been divided into several stages: the compaction of the laminate and heating of the mold and resin, the infusion process, the heating ramp (controlled temperature increase), holding at the constant curing temperature (plateau), and the cooling phase. This division was made to facilitate the analysis of the results.

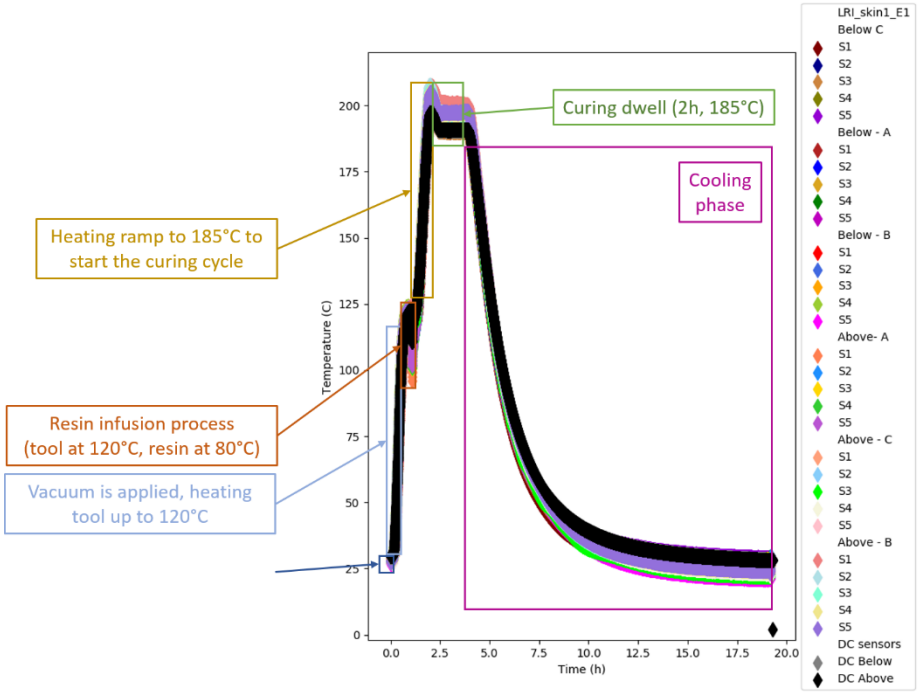


**Figure 3.11**. *The results of temperature monitoring with FBG sensors for the entire LRI curing cycle of a 2.5 mm thick laminate specimen.*

In figure 3.12, the DC sensors are represented and compared with the FBG temperature sensors located nearby.

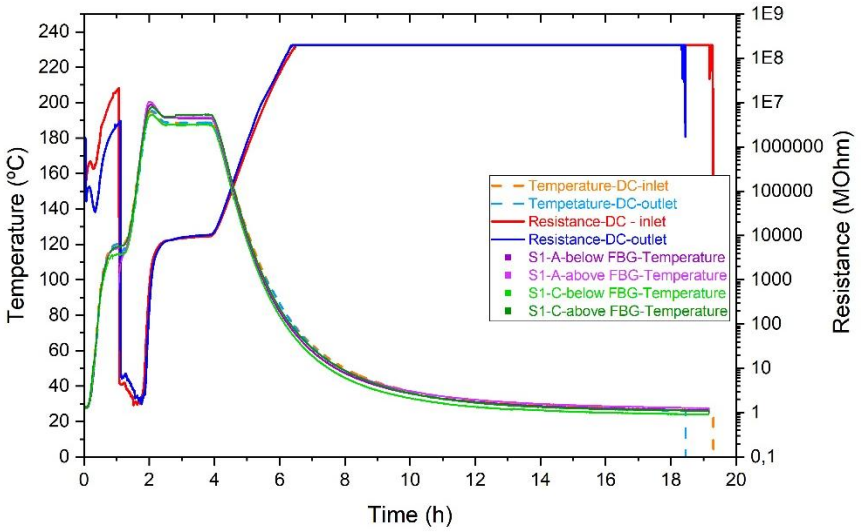


**Figure 3.12**. *Comparison between the temperature monitoring results with FBG and DC sensors and the resistance of the DC sensors during the LRI curing cycle of the 2.5mm skin specimen*

### *3.2.2.2 Strain monitoring results*

By analyzing the results obtained from the FBG strain sensors, presented in Figure 3.13, it is possible to identify the same manufacturing phases as in the case of the temperature data. However, the strain values shown in these graphs are interpreted based on the understanding that only after the gel point, the strain experienced by the specimen (and the sensors) is due to

the curing process. Monitoring the resin curing cycle has shown that only after the gelation point does the strain result from resin shrinkage. The strain recorded by the sensors before this point is caused by pressure and temperature fluctuations. Therefore, in order to analyze the strain caused by resin shrinkage during the curing reaction, the strain at the gel point is considered to be zero.

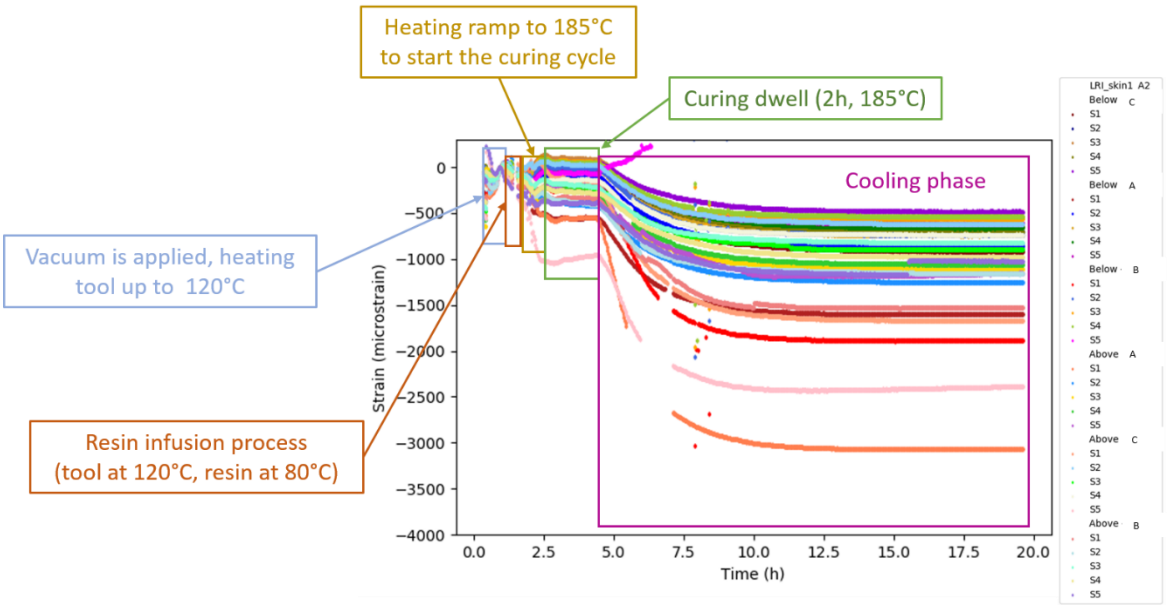


**Figure 3.13**. *Strain monitoring results using FBG sensors for the entire LRI curing cycle of a 2.5 mm thick skin specimen.*

### *3.2.2.3 Post-manufacturing monitoring and measurements*

To analyze how the shape of these specimens changes, contour plots for differences in the Z-coordinate were used. Figure 3.14 presents contour plots extracted from coordinate measurements taken at different times after demolding, where warmer areas indicate higher Z-coordinate values, meaning the part is lifting away from the support tools at those points. These plots show that there is a deformation of the central part of the specimen, indicating that the curvature of the skin specimen increases over time. When comparing the 2.5 mm and 11.5 mm skin specimens, the 2.5 mm specimen shows greater shape variations after 7 days than the 11.5 mm specimen.

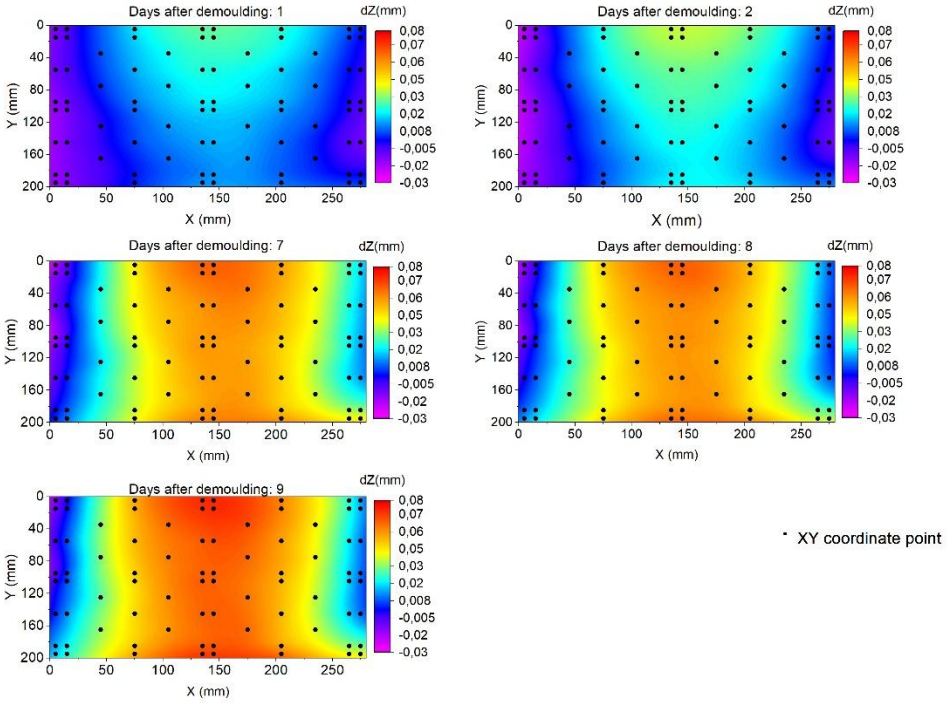


**Figure 3.14**. *3D CMM results for the 2.5 mm skin specimen, obtained 1, 2, 7, 8, and 9 days after demolding, where the black dots represent the coordinate measurement points*

### *3.2.2.4 Strain monitoring results*

The same strain sensors used for monitoring the specimens during the manufacturing phase (and which were not damaged during the demolding phase) were also used for monitoring deformations during the post-manufacturing evaluation with 3D CMM. The advantage of using the same sensors is that they are already integrated into the specimen, thus directly measuring the deformations caused by the release of residual stress.

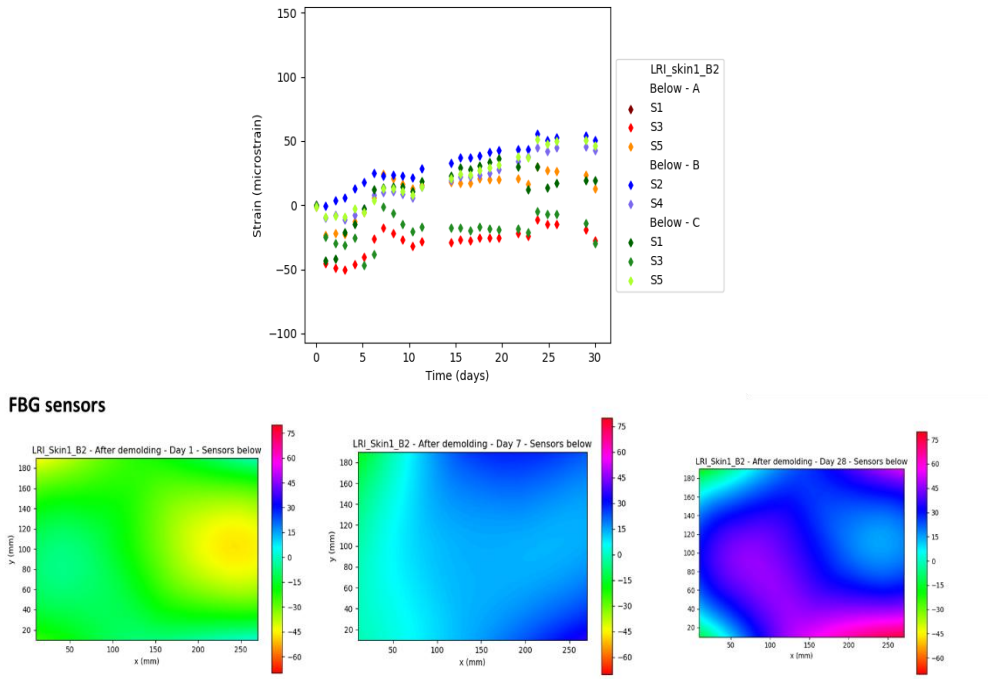


**Figure 3.15**. *Evolution of the strain response of FBG sensors embedded in a 2.5 mm Skin specimen after the demolding process (top graph). Strain maps based on the sensor responses on days: 1 (left), 7 (center), and 28 (right) for the same specimen*

### 3.2.3 PHASE 2

Sensor network map for this demonstrator with complex geometry was created using a total of 4 FBG arrays (lines in Figure 3.16), containing a total of 36 FBG sensors (green dots in Figure 3.16). These sensors were distributed as illustrated in Figure 3.16: one of the "U" stringer specimens had an array positioned with 9 FBG sensors for strain measurement (red line), the lower surface of the skin specimen had an array with 12 FBG sensors positioned for strain measurement (purple line), and the upper surface of the skin specimen had two arrays—one for strain measurement with 12 FBG sensors (purple line) and another for temperature measurement with 3 FBG sensors (gold line).

The sensor distribution comprises a total of 4 FBG arrays (lines in Figure 3.16), containing a total of 36 FBG sensors (green dots in Figure 3.16). These sensors were distributed as illustrated in Figure 3.16: one of the U stringer specimens had an array positioned with 9 FBG sensors for strain measurement (red line), the lower surface of the skin specimen had an array with 12 FBG sensors positioned for strain measurement (purple line), and the upper surface of the skin specimen had two arrays—one for strain measurement with 12 FBG sensors (purple line) and another for temperature measurement with 3 FBG sensors (gold line).

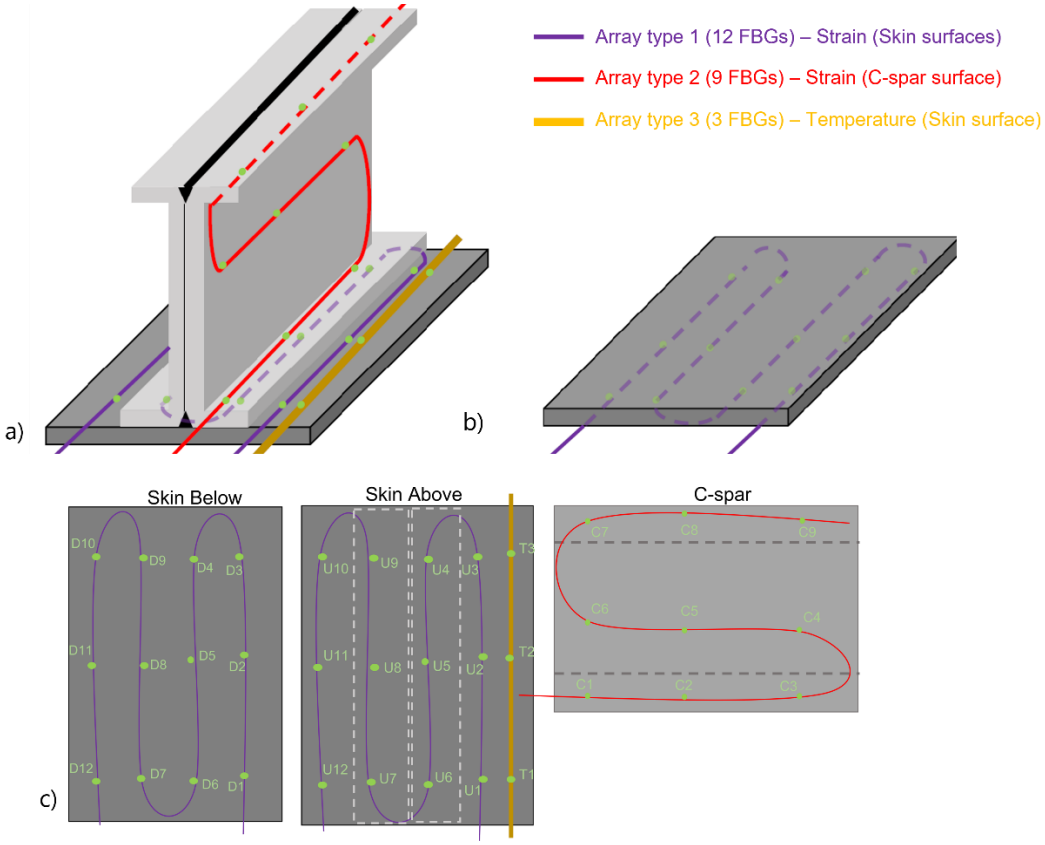


**Figure 3.16.** *Distribution of FBG Sensors in the PHASE 2 Demonstrator (green dots). a) Distribution of strain sensors on the U-stringer (red line), and strain and temperature sensors on the upper surface of the skin (purple line – strain, gold line – temperature), b) Strain sensors on the lower surface of the skin (purple line), and c) position of each FBG sensor on the fiber optic arrangements for each surface.*

The manufacturing activities were carried out similarly to PHASE 1. During the thermoforming of the carbon fiber preforms, the optical fiber outputs were protected in a box to preserve their integrity. Additionally, the optical fibers were secured with epoxy adhesive to prevent movement during the process. The monitoring of the test specimen, as well as the information charts, were conducted according to the procedures developed in PHASE 0 and PHASE 1.

## REFERENCES CHAPTER 3

**[BC3.1]** Pantelelis, Nikos "Optimised cure cycle in Resin Transfer Moulding." Compos SciTechnol. 63 (2003):249-264
**[BC3.2]** Pantelelis, Nikos "Towards the dynamic optimization for the cure control of thermoset-matrix composite materials." Compos Sci Technol. 65 (2005): 1254-1263
**[BC3.3]** Tajima Y. Monitoring Cure Viscosity of Epoxy Composite. Polymer Composites, 3, pp. 162-169 (1982)
**[BC3.4]** Schwab S., Levy R., Glover G. Sensor System for Monitoring Impregnation and Cure During Resin Transfer Molding, Polymer Composites 17, pp. 312-316 (1996)
**[BC3.5]** G.Boiteux, P.Dublineau, M.Feve, C.Mathieu, G.Seytre and J.Ulanski, Dielectric and viscoelastic studies of curing epoxy-amine model systems, Polymer Bulletin 30, 441-447 (1993)
**[BC3.6]** C. Garschke, C. Weimer, P.P. Parlevliet, B.L. Fox, Out-of-autoclave cure cycle study of a resin film infusion process using in situ process monitoring, Composites Part A 43 (2012) 935–944
**[BC3.7]** Pantelelis N., Bistekos E, Process monitoring and control for the production of CFRP componentsin "Proceedings of Conference SAMPE'10", Seattle, USA (2010)
**[BC3.8]** N. Pantelelis, A. Bansal, I. Harismendy, R. Mezzacasa, E. Bistekos, Intelligent Monitoring of the Infusion of Large Carbon-fibre Reinforced Structural Parts, in: First International Symposium on Automated Composites Manufacturing, 2013, Concordia University, Montreal, Canada
**[BC3.9]** Ramakrishnan, M.; Rajan, G.; Semenova, Y.; Farrell, G. Overview of Fiber Optic Sensor Technologies for Strain/Temperature Sensing Applications in Composite Materials. Sensors 2016, 16, 99
**[BC3.10]** Di Sante, R. Fibre Optic Sensors for Structural Health Monitoring of Aircraft Composite Structures: Recent Advances and Applications. Sensors 2015, 15, 18666-18713
**[BC3.11]** *Sensors* 2014, *14*, 7394-7419; doi:10.3390/s140407394
**[BC3.12]** Raymond M. Measures, Fiber optic sensing for composite smart structures, Composites Engineering, Volume 3, Issues 7–8, 1993, Pages 715-750, ISSN 0961-9526, https://doi.org/10.1016/0961-9526(93)90093-Y
**[BC3.13]** Alfredo Guemes, Malte Frovel, Antonio Fernandez-Lopez, Jose Maria Pintado; "Computational Simulation and Experimental Validation of a Fiber-Optic Based SHM System Applied to a UAV Structure"; STO-MP-AVT-305, 2018
**[BC3.14]** Nobuo Takeda and Shu Minakuchi; "Recent development of optical fiber sensor based structural health monitoring and in-process monitoring of CFRP structures in Japan"; 9th European Workshop on Structural Health Monitoring July 10-13, 2018, Manchester, United Kingdom
**[BC3.15]** Johannes Mattheus BALVERS; "In situ strain & cure monitoring in liquid composite moulding by fibre Bragg grating sensors"; Thesis, Technische Universiteit Delft, 2014
**[BC3.16]** S. Konstantopoulos, E. Fauster, R. Schledjewski; "Monitoring the production of FRP composites: A review of in-line sensing methods"; eXPRESS Polymer Letters Vol.8, No.11 (2014) 823–840
**[BC3.17]** L. Khoun, R. de Oliveira, V. Michaud, P. Hubert; "Measurement of process-induced strains by fibre bragg grating optical sensor in resin transfer moulding"; ICCM17proceedings
**[BC3.18]** Clara Andrea Pereira Sánchez; "Analysis of Shape Distortion Resulting from the Manufacturing Process of Thermoset Composites"; Master thesis, Joint master programme in Turbomachinery Aeromechanical University Training (THRUST), June 2017
**[BC3.19]** Pierre Ferdinand, Sylvain Magne, Véronique Dewynter-Marty, Stéphane Rougeault, Laurent Maurin. Applications of Fiber Bragg Grating sensors in the composite industry. MRS Bulletin, Cambridge University Press (CUP), 2002, 27 (5), pp.400-407. <10.1557/mrs2002.126>. <cea-01841910>
**[BC3.20]** Raffaella Di Sante; "Fibre Optic Sensors for Structural Health Monitoring of Aircraft Composite Structures: Recent Advances and Applications"; *Sensors* 2015, *15*, 18666-18713; doi:10.3390/s150818666

**[BC3.21]** X. W. Ye, Y. H. Su, and J. P. Han; "Structural Health Monitoring of Civil Infrastructure Using Optical Fiber Sensing Technology: A Comprehensive Review"; The Scientific World Journal Volume 2014 (2014), Article ID 652329, 11 pages http://dx.doi.org/10.1155/2014/652329
**[BC3.22]** Stephen J. Mihailov; "Fiber Bragg Grating Sensors for Harsh Environments"; Sensors 2012, 12, 1898-1918; doi:10.3390/s120201898
**[BC3.23]** Kleiton de Morais Sousa, Werner Probst, Fernando Bortolotti, Cicero Martelli and Jean Carlos Cardozo da Silva; "Fiber Bragg Grating Temperature Sensors in a 6.5-MW Generator Exciter Bridge and the Development and Simulation of Its Thermal Model"; Sensors 2014, 14, 16651-16663; doi:10.3390/s140916651
**[BC3.24]** Co-PATCH project http://www.co-patch.com/
**[BC3.25]** OXIGEN project http://cordis.europa.eu/project/rcn/106325_en.html
**[BC3.26]** NEWSOL project http://cordis.europa.eu/project/rcn/207604_en.html
**[BC3.27]** FOSAS project http://cordis.europa.eu/result/rcn/159516_en.html
**[BC3.28]** Gabriele Chiesura, Alfredo Lamberti, Yang Yang, Geert Luyckx, Wim Van Paepegem, Steve Vanlanduit, Jan Vanfleteren and Joris Degrieck; "RTM Production Monitoring of the A380 Hinge Arm Droop Nose Mechanism: A Multi-Sensor Approach"; Sensors 2016, 16, 866; doi:10.3390/s16060866
**[BC3.29]** Damien Kinet, Patrice Mégret, Keith W. Goossen, Liang Qiu, Dirk Heider and Christophe Caucheteur; "Fiber Bragg Grating Sensors toward Structural Health Monitoring in Composite Materials: Challenges and Solutions"; Sensors 2014, 14, 7394-7419; doi:10.3390/s140407394
**[BC3.30]** G Luyckx, W De Waele, J Degrieck, W Van Paepegem, J Vlekken, S Vandamme and K Chah; "Three-dimensional strain and temperature monitoring of composite laminates"; Insight Vol 49 No 1 January 2007
**[BC3.31]** Shu Minakuchi, Takahide Umehara, Kazunori Takagaki, Yusaku Ito, Nobuo Takeda; "Life cycle monitoring and advanced quality assurance of L-shaped composite corner part using embedded fiber-optic sensor"; Composites: Part A 48 (2013) 153–161
**[BC3.32]** Ulrich A. Mortensen, Tom L. Andersen, Jacob Christensen, Marco Aurelio Miranda Maduro; "Experimental investigation of process induced strain during cure of epoxy using optical fibre bragg grating and dielectric analysis"; ECCM18 - 18th European Conference on Composite Materials Athens, Greece 24-28th June 2018

# 4. CALIBRATION OF EXPERIMENTAL DETERMINATIONS OF GEOMETRIC DISTORTIONS INDUCED BY RESIDUAL STRESSES GENERATED DURING THE MANUFACTURING OF ANISOTROPIC STRUCTURES, ESTIMATION OF UNCERTAINTIES AND ERRORS OF THE TECHNIQUES USED TO MEASURE THESE DISTORTIONS

Experimental measurements are fundamental for the analysis and understanding of the behavior of mechanical and composite structures. The accuracy of these measurements is essential for validating theoretical models, evaluating material performance, and, in our case, accurately estimating distortions and ensuring the safety of structures used in engineering. However, any measurement process is subject to uncertainties and errors, which can affect the interpretation of results. To obtain relevant and reliable experimental data, rigorous calibration of measurement instruments is necessary, along with the identification of sources of uncertainty and the minimization of both systematic and random errors..

## 4.1 FUNDAMENTALS OF MEASUREMENTS

### 4.1.1 MEASUREMENT

The objective of a measurement is to determine the value of the measurand, that is, the value of the specific quantity to be measured. Therefore, a measurement begins with the proper specification of the measurand, the measurement method, and the measurement procedure.

### 4.1.2 EXPERIMENTAL DATUM

An experimental datum refers to a single measurement recorded during an experiment. In the context of laminated composite structures, these data may represent deviations, strain readings, or angular distortions. The accuracy and precision of these data are influenced by multiple factors, including sensor sensitivity, environmental conditions, and human error[***BC4.1***].

### 4.1.3 ERRORS, EFFECTS AND CORRECTIONS

In general, a measurement exhibits imperfections that generate an error in the measurement result. Traditionally, an error is considered to have two components: a random component and a systematic component. Error is an idealized concept and cannot be known precisely [***BC4.2***].

The random component of the error presumably arises from unpredictable or stochastic temporal and spatial variations of influencing quantities. The effects of these variations, hereafter referred to as random effects, cause variations in repeated observations of the measured quantity. Although it is not possible to compensate for the random error of a measurement result, it can usually be reduced by increasing the number of observations; its expected or mean value is zero.

Systematic error, like random error, cannot be eliminated but can often be reduced. If a systematic error arises due to a recognized effect of an influencing quantity on the result of a measurement—hereafter referred to as a systematic effect—this effect can be quantified. If it is

significant relative to the required measurement precision, a correction or correction factor can be applied to compensate for the effect. It is assumed that, after applying the correction, the expected value of the error caused by a systematic effect is zero.
The uncertainty of a correction applied to a measurement result to compensate for a systematic effect is not the systematic error—often referred to as bias—of the measurement result caused by that effect. Instead, it represents a measure of the uncertainty of the result due to incomplete knowledge of the necessary correction value. The error resulting from imperfect compensation of a systematic effect cannot be known exactly. The terms "error" and "uncertainty" must be used correctly, and the difference between them should be carefully considered.

### 4.1.4 MEASURMENTS UNCERTAINTIES

The uncertainty of a measurement result reflects the lack of exact knowledge of the true value of the measured quantity. The result of a measurement, after correcting for recognized systematic effects, remains only an estimate of the true value of the measured quantity, due to uncertainty arising from random effects and the imperfect correction of the result for systematic effects.
Measurement uncertainty is often estimated using the standard error of repeated measurements:

$$u = \sqrt{\frac{\sum(x_i - \bar{x})^2}{n-1}} \tag{4.1}$$

where $x_i$ are the individual measurements, $\bar{x}$ is the mean value, and $\boldsymbol{i}$ s the number of measurements.
Classifying the methods used to evaluate the components of uncertainty, rather than classifying the components themselves, avoids this ambiguity. At the same time, it does not exclude the possibility of grouping individual components—evaluated using the two different methods—into categories designated for use in a specific context [***BC4.4***].

### 4.1.5 PRACTICAL ASPECTS

To determine whether a measurement system is functioning correctly, the experimentally observed variability of its output values—measured by the observed standard error—is often compared with the expected standard error, obtained by combining the various uncertainty components that characterize the measurement. In such cases, only those components (whether obtained through Type A or Type B evaluations) that could contribute to the experimentally observed variability of these output values should be considered. This analysis can be facilitated by separately grouping the components that contribute to variability and those that do not, labeling them accordingly.

In some cases, the uncertainty of a correction for a systematic effect should not be included in the evaluation of the measurement result's uncertainty. Although the uncertainty has been assessed, it may be disregarded if its contribution to the combined standard uncertainty of the measurement result is insignificant. If the correction value itself is insignificant relative to the combined standard uncertainty, it too may be ignored [***BC4.6-BC4.8***].

## 4.2 CALCULATION OF ERRORS AND UNCERTAINTIES IN TEST SPECIMEN MEASUREMENTS USING CMM

Coordinate Measuring Machines (CMMs) are widely used in industry to verify the precision of mechanical components. To ensure accurate and repeatable measurements, proper calibration of the CMM is essential. This subsection presents calibration techniques, the necessary steps, and relevant examples for their application.

### 4.2.1 MEASUREMENT UNCERTAINTY DUE TO THE TEMPERATURE OF THE PART

Ideally, the entire measurement process could be mathematically modeled, including all relevant parameters that could influence the measurement, as indicated in equation 4.2:

$$Y = f(X_1, X_2, \dots X_N) \tag{4.2}$$

Where the value of the measurement $Y$ depends on a $N$ number of measurements.

A model of measurement uncertainty could then be developed using the law of propagation of uncertainty, that is, equation 4.3, and the estimation of the variance and covariance of the individual uncertainty terms

The uncertainty of $y$ is given by the following relation:

$$u_y = \sqrt{\left(\frac{\partial y}{\partial x_1} u_{x_1}\right)^2 + \left(\frac{\partial y}{\partial x_2} u_{x_2}\right)^2 + \cdots} \tag{4.3}$$

Where $u_{x_i}$ are the individual measurement uncertainties.

### 4.2.2 THE EMPLOYED CMM EQUIPMENT

For the shape distortion estimates of the manufactured specimens, a Hexagon GLOBAL Advantage 20.40.18 coordinate measuring machine (CMM) was used, equipped with a 2 mm diameter probe, for comparison with the response of the FBG sensors and their calibration.

Figure 4.1 shows a schematic presentation of the equipment used for measurements, and Table 4.1 includes the general specifications of the same CMM equipment.

**Table 4.1.** Specificaţie generală echipament CMM

| Measurement range (mm) | | | Dimensions (mm) | | | | Measurement table (mm) | Max. mass of measured part (kg) | CMM machine mass (kg) |
|---|---|---|---|---|---|---|---|---|---|
| X | Y | Z | Lx | Ly | Lz | Dz | Py | | |
| 2000 | 4000 | 1800 | 2888 | 5240 | 5326 | 1950 | 5000 | 5000 | 17970 |

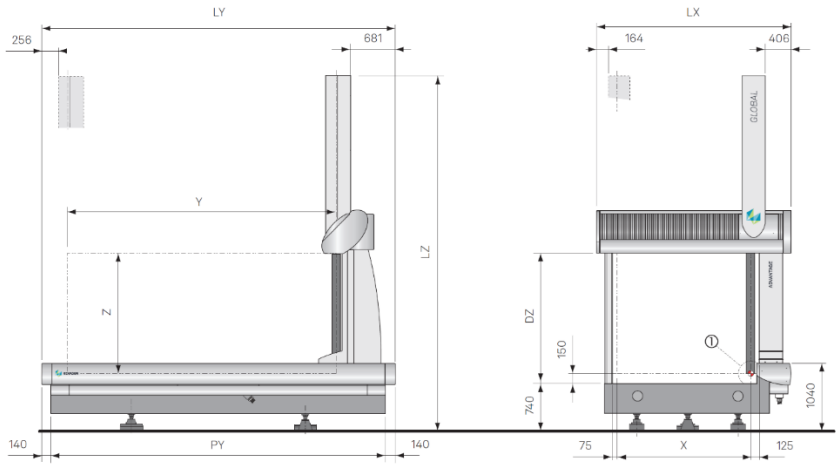


**Figure 4.1.** *CMM machine Hexagon GLOBAL Advantage 20.40.18*

## 4.2.3 CALCULATION OF ERRORS IN THE CMM MEASUREMENT OF A TEST SPECIMEN

To evaluate the changes in the Z coordinate during the first 9 days after manufacturing, a measurement scheme with 80 points uniformly distributed over the geometry of the specimen was used (Figure 4.2).

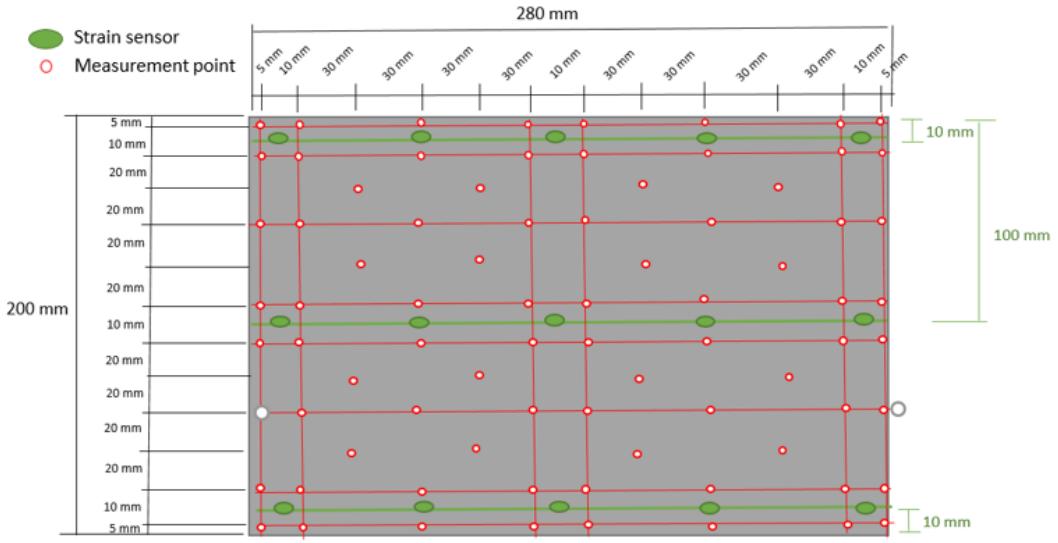


**Figure 4.2.** *Distribution of coordinate points on the test panel specimen for shape distortion measurements using 3D CMM*

Based on the measurement results in the X, Y, and Z columns, the r column was calculated using the following relation:

$$r = \sqrt{X^2 + Y^2 + Z^2}\ (mm) \tag{4.4}$$

Starting from relation 4.4, I calculated the error for each of the X, Y, and Z directions as follows:

$$\Delta_{x,y,z} = \left(4{,}5 + 1 \cdot \frac{L}{250}\right)(\mu m) \tag{4.5}$$

The value of the absolute error is calculated using the following relation:

$$\Delta_{abs} = \sqrt{\Delta_X^2 + \Delta_Y^2 + \Delta_Z^2}(\mu m) \quad (4.6)$$

Based on the numerical values from the measurements, the graph of the variation of the measurement deviations as a function of the measured value is plotted, as shown in Figure 4.3.

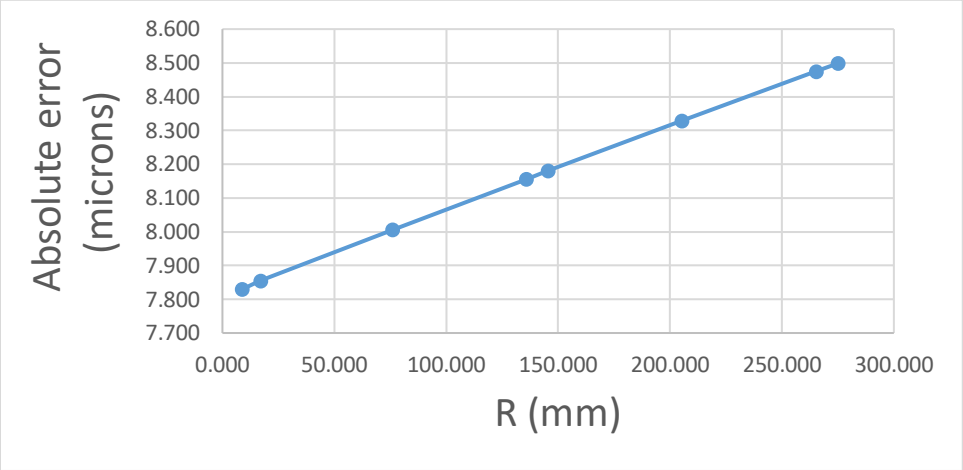


**Figure 4.3.** *Variation of measurement errors as a function of the measured value*

## 4.2.4 CALCULATION OF UNCERTAINTIES IN CMM MEASUREMENT OF A TEST SPECIMEN

Using the data detailed in Table 4.8 and applying the mathematical relations 4.7–4.11, the uncertainty associated with the three directions and the angles $\alpha$, $\beta$ si $\gamma$, was calculated :

$$U_x(\alpha) = \frac{\Delta_{x_{max}} - \Delta_{x_{min}}}{2} = 5{,}6 - 4{,}52 = 0{,}54\mu m \quad (4.7)$$

$$U_y(\beta) = \frac{\Delta_{y_{max}} - \Delta_{y_{min}}}{2} = 5{,}28 - 4{,}52 = 0{,}38\mu m \quad (4.8)$$

$$U_z(\gamma) = \frac{\Delta_{z_{max}} - \Delta_{z_{min}}}{2} = 4{,}55 - 4{,}52 = 0{,}015\mu m \quad (4.9)$$

Next, the measurement uncertainty is calculated $U(\alpha,\beta,\gamma)$ in relation to the three angles using relation 4.110:

$$U(\alpha,\beta,\gamma) = \max(U_x(\alpha), U_y(\beta), U_z(\gamma)) = 0{,}54\mu m \quad (4.10)$$

The total measurement uncertainty of the CMM equipment is calculated using relation 4.11.:

$$U = \sqrt{U_x^2 + U_y^2 + U_x^2} = 0{,}66\mu m \quad (4.11)$$

The CMM equipment uncertainty is determined as U=0,66µm.

The measurement uncertainty of the equipment is calculated based on the measurement results and is higher than the uncertainty indicated in the equipment's calibration certificate.

## REFERENCES CHAPTER 4

**[BC4.1]** JCGM 100:**2008** - Evaluation of measurement data — Guide to the expression of uncertainty in measurement (GUM)**.**
**[BC4.2]** ISO/IEC Guide 98-3:**2008** - Uncertainty of measurement — Part 3: Guide to the expression of uncertainty in measurement**.**
**[BC4.3]** Holman, J.P. (**2012**). Experimental Methods for Engineers. McGraw-Hill Education
**[BC4.4]** Bendat, J. S., & Piersol, A. G. (**2010**). Random Data: Analysis and Measurement Procedures. Wiley.
**[BC4.5]** Coleman, H.W., & Steele, W.G. (**2009**). Experimentation, Validation, and Uncertainty Analysis for Engineers. Wiley.
**[BC4.6]** Taylor, J.R. (**1997**). An Introduction to Error Analysis: The Study of Uncertainties in Physical Measurements. University Science Books.
**[BC4.7]** BIPM (**2019**). International Vocabulary of Metrology – Basic and General Concepts and Associated Terms (VIM).
**[BC4.8]** Dietrich, C.F. (**1991**). Uncertainty, Calibration and Probability: The Statistics of Scientific and Industrial Measurement. Adam Hilger.
**[BC4.9]** Moffat, R.J. (**1988**). Describing the Uncertainties in Experimental Results. Experimental Thermal and Fluid Science.
**[BC4.10]** Beckwith, T.G., Marangoni, R.D., & Lienhard, J.H. (**2007**). Mechanical Measurements. Pearson.
**[BC4.11]** R.G. Easterling, M.E. Johnson, T.R. Bement, and C.J. Nachtsheim, Absolute and Other Tolerances, SAND88-0724, LA-UR 88-906 (Sandia National Laboratories) **1989**.
**[BC4.12]** VDWDE 2617 Accuracy of Coordinate Measuring Machines (1986), Beuth Verlag, D-1000 Berlin, Germany.
**[BC4.13]** CMMA Accuracy Specification for Coordinate Measuring Machines (1989) London, England.
**[BC4.14]** JIS B 7440 Test Code for Accuracy of Coordinate Measuring Machines (1987), Translated and Published by the Japanese Standards Association.

# 5. DUAL INVESTIGATIONS FOR ESTIMATING GEOMETRIC DISTORTIONS INDUCED BY RESIDUAL STRESSES GENERATED IN THE FABRICATION OF MULTILAYER ANISOTROPIC STRUCTURES USED IN THE AEROSPACE INDUSTRY

This chapter of the research paper is based on the article *Development of a Numerical Tool for Laminate Composite Distortion Computation Through a Dual-Approach Strategy* [***BC5.1***] published in *Appl. Sci. 2024, 14(22), 10656;* https://doi.org/10.3390/app142210656, authored by Eng. Cesar BANU and Prof. Univ. Habil. Dr. Ing. Mihai BUGARU.

## 5.1 DEVELOPMENT OF THE NUMERICAL TOOL FOR SIMULATION

### 5.1.1 CONTEXT

The technological and scientific developments presented in this chapter are attributed to the ELADINE project—Evaluation of Laminate Composite Distortion through an Integrated Numerical-Experimental Approach [***BC5.2***]. The project was a support activity (CfP) for the OPTICOMS project [***BC5.3***], developed within the European Clean Sky 2 Program and funded by the European Commission. ELADINE aimed to create an innovative numerical tool for predicting the spring-in phenomenon of primary structural components of an aircraft wing, using an approach where the development and validation of the numerical simulation were based on experimental polymerization data.

An overview of these mechanisms and a high-level approach for the development of a numerical tool for composite distortion evaluation is described in Figure 5.1 [***BC5.4***].

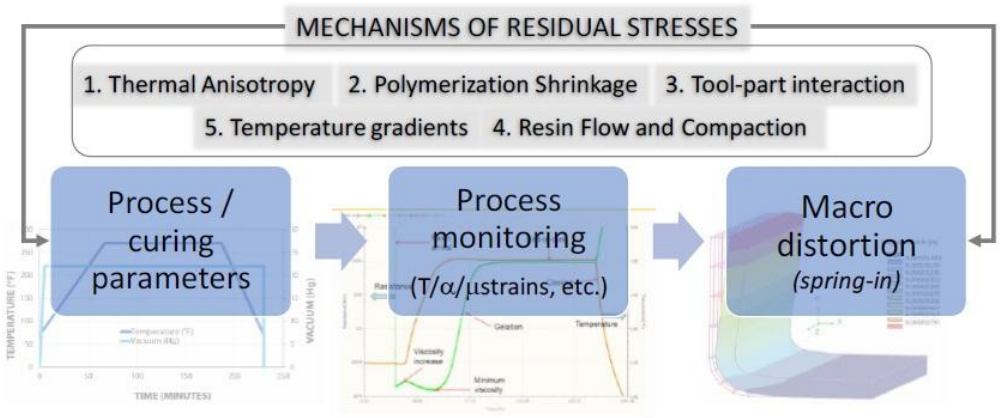


**Figure 5.1.** *Illustration of mechanisms that produce distortion [**BC5.4**]*

### 5.1.2 EXISTING SIMULATION TOOLS AND THEIR SIMULATION CAPBILITIES

In this context, the first step was to identify simulation tools that represent the industry standard for predicting composite distortion. One of the most cited software packages is ESI PAM DISTORTION [***BC5.5***], along with a more complex module called PAM COMPOSITES. According to the ESI website, this tool allows the prediction of residual stresses induced by

manufacturing and the distortion of shapes of composite parts made from continuous fibers and thermoset matrices. A more recent simulation solution, with a similar approach and capabilities to PAM DISTORTION, is ALTAIR Advanced Cure Simulation [***BC5.6***], which promises users the ability to predict polymerization, accumulation of residual stresses, and deformations during composite processing.

### 5.1.3 SIMULATION STRATEGY

Strategia de simulare ia in considerare subacapitolele studiate în sectiunea 1.1 MECANISME CARE GENEREAZA TENSIUNI REMANENTE ȘI DISTORSIUNI GEOMETRICE, dupa cum urmeaza:

*5.1.3.1 Thermal anisotropy*

*5.1.3.2. Cure shrinkage*

*5.1.3.3 Interacțiunea matriță–piesă*

*5.1.3.4. Resin flow and fibers compaction*

*5.1.3.5. Temperature gradientrs*

*5.1.3.6. The experimental approach to monitoring the manufacturing process*

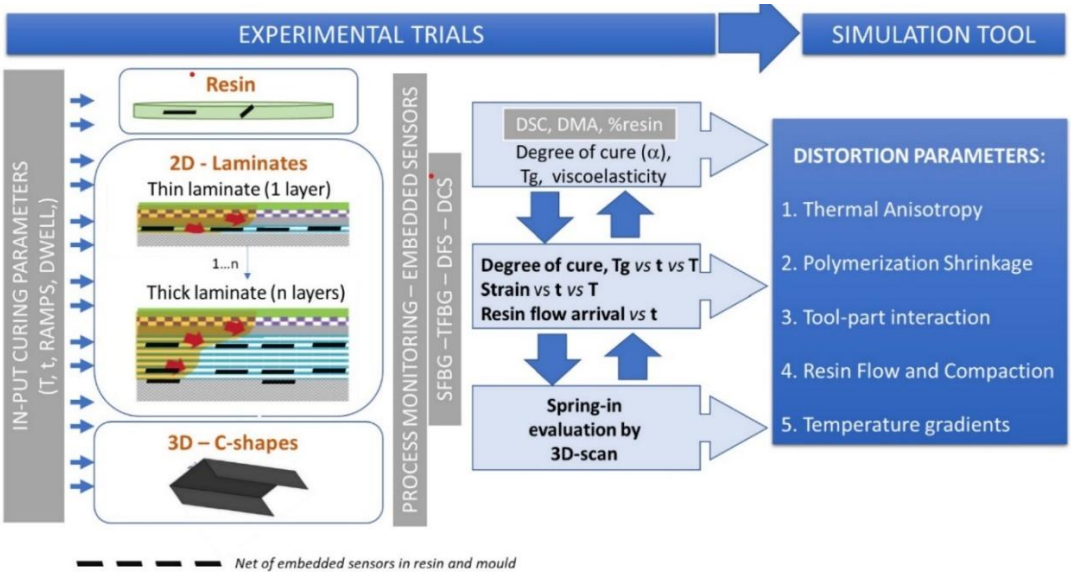


**Figure 5.2.** *Ilustration of the scope of the experimental program* [***BC5.4***]

The manufacturing process was carefully monitored by integrating optical sensors with fiber Bragg grating (FBG) diffraction network sensors and dielectric sensors (DC). The data collected from this monitoring were used to calibrate a simulation tool based on the finite element method (FEM), aimed at predicting shape distortions in large-scale integral composite wing structures [***BC5.4***]. The experimental program used FBG sensors to evaluate temperature and deformations in specimens and test samples, while DC sensors were used to determine the degree of resin polymerization [***BC5.4***].

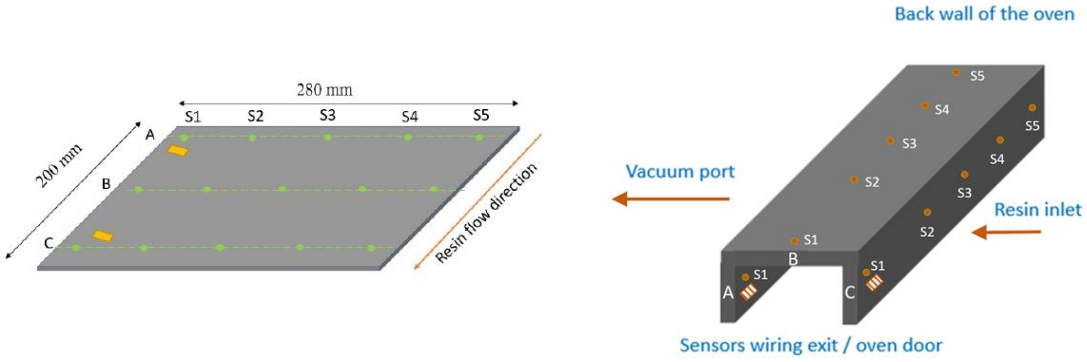


(**a**) (**b**)

**Figure 5.3.** *(**a**) The distribution of sensors on a shell-type specimen: FBG sensors (green dots) and DC sensors (squares). (b) The distribution of sensors on a C-profile specimen: FBG sensors (orange dots) and DC sensors (squares). [**BC5.1, BC5.4**].*

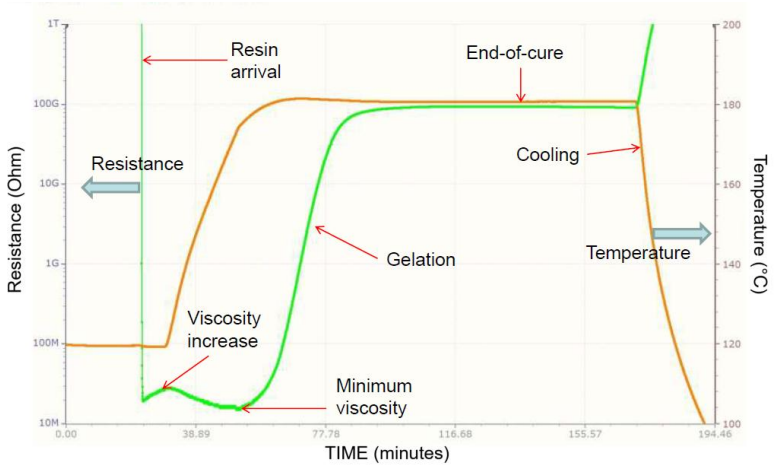


**Figure 5.4.** *Typical monitoring results of the RMT6 epoxy resin cycle. Disposable DC sensors can measure various events that occur during the resin curing process [**BC5.1, BC5.4**]*

## 5.1.4 MATHEMATICAL MODELS. DEVELOPMENT OF THE NUMERICAL MODEL LOGIC

The development of a numerical model to predict complex distortions was based on established commercial simulation software, namely MSC PATRAN, MSC NASTRAN, and MSC MARC. To conduct a numerical analysis of distortion in the fabrication of composite materials, a series of steps were defined as an initial strategy for evaluating the operational capabilities of a generic model:

- Development of the geometric configuration for both the specimen and the manufacturing tools;
- Specification of thermal and structural material characteristics relevant to both the specimen and the tool;
- Establishment of the universal unitary system that will be used throughout the simulation; construction of the finite element model (FEM), including mesh placement and stacking sequence for both the specimen and the tool;

- Determination of the material properties in the FEM for each layer, including both thermal and structural attributes;
- Definition of input parameters necessary for conducting a finite element thermal analysis, including the initial temperature of the specimen/tool assembly, temperature fluctuations in the oven, convective effects on the outer surface of the assembly, thermal interactions between the specimen and the tool, as well as the specific requirements for the mathematical model used in solving the finite element analysis to facilitate polymerization calculations;
- Enhancement of the thermal model based on data obtained from experimental monitoring and, finally, the development and solving of a thermostructural finite element model that integrates structural properties such as Young's Modulus, polymerization shrinkage, and temperature- and polymerization rate-dependent viscosity.

The sequences for the development of the numerical model:

*5.1.4.1. Cure reaction kinetics*

*5.1.4.2 Resin shrinkage during curing*

*5.1.4.3. Variation of the resin modulus during the cure process;*

*5.1.4.4. Laminate mechanical properties during the manufacturing process*

### 5.1.5 SIMULATION MODEL STRUCTURE

A simulation model was build in the Marc commercial software. The model was conceived as thermal-structural with the following components: a model thermal-structural:

- Transient tmal component;
- Structural quasi-static component.

The transient thermal component manages thermal elements, such as temperature variation, specific heat, thermal conduction, and thermal convection.
The quasi-static structural component manages structural elements, such as Young's Modulus, Shear Modulus, Poisson's ratio, deformations, internal stresses, etc.
To illustrate the logic of the workflow and the functional steps of the model, we have defined a model architecture diagram presented in Figure 5.5.

1. For each value of the degree of polymerization between 0 and 1, the resin has specific values for its mechanical properties;
2. The resin-impregnated fibers have mechanical properties that can be considered constant within the working temperature range;
3. Using the DIGIMAT 2019.1 software tool and applying homogenization theory, equivalent material properties for an orthotropic sheet impregnated with resin were calculated at different degrees of polymerization.

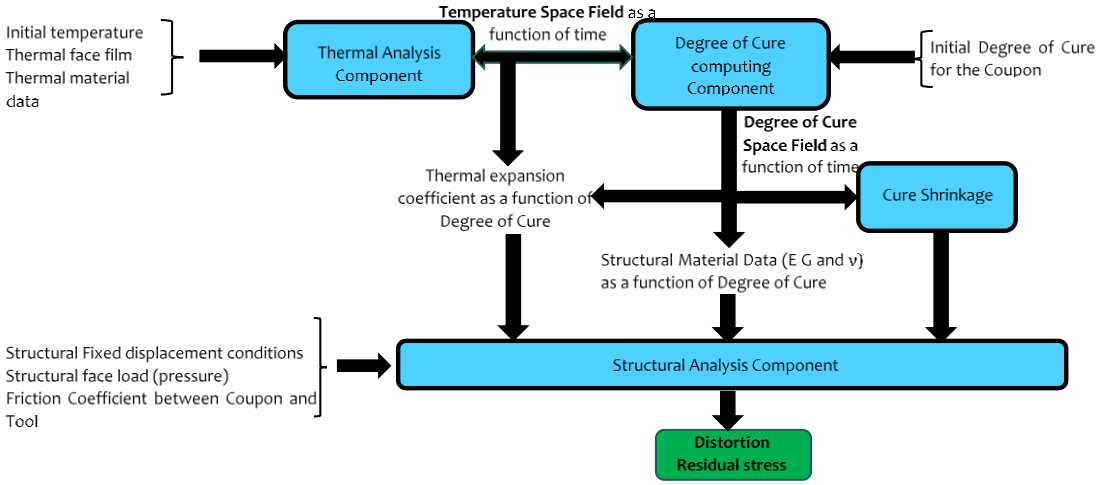


**Figure 5.5.** Simulation model architecture and the simulation sequence *[**BC5.1, BC5.2**]*.

## 5.1.6 STUDIED CASES

Two types of specimens were defined for both the experimental program and the simulation work—the geometries of the specimens are described in Figures 5.6 and 5.7. The specimens for the shell were chosen with a geometry relevant to the shell of the shell–stringer assembly designed within the European project OPTICOMS [***BC5.3***], for which CfP ELADINE [***BC5.2***] prepared the matrix compensation strategy and the numerical simulation tool.

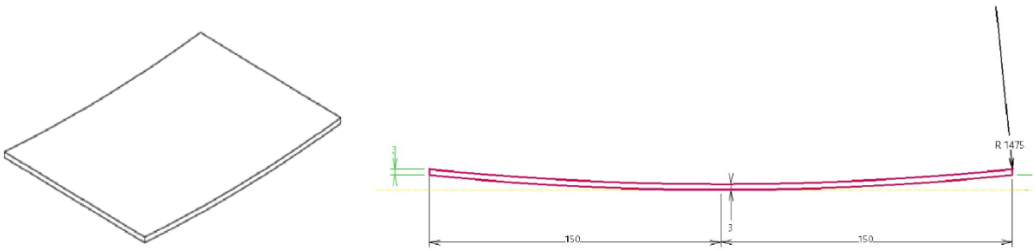


**Figure 5.6**. *Skin specimen*

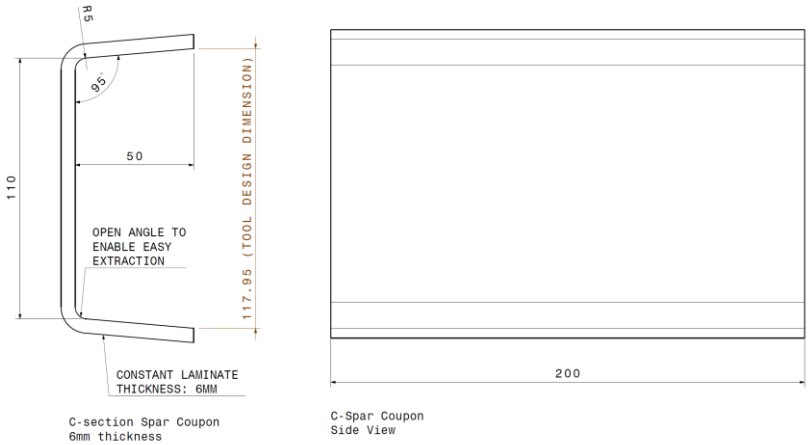


**Figure 5.7.** U-spar specimen [***BC5.1-BC5.3***].

## 5.2 RESULTS

During the initial development phase, numerical trials were conducted for small-sized specimens with geometries identical to those used in the experimental trials. Shells with low curvature and C-profile specimens were extensively analyzed to understand the model and its constraint effects on distortion. This first phase of the numerical model development was also the most intensive among the test specimens analyzed.

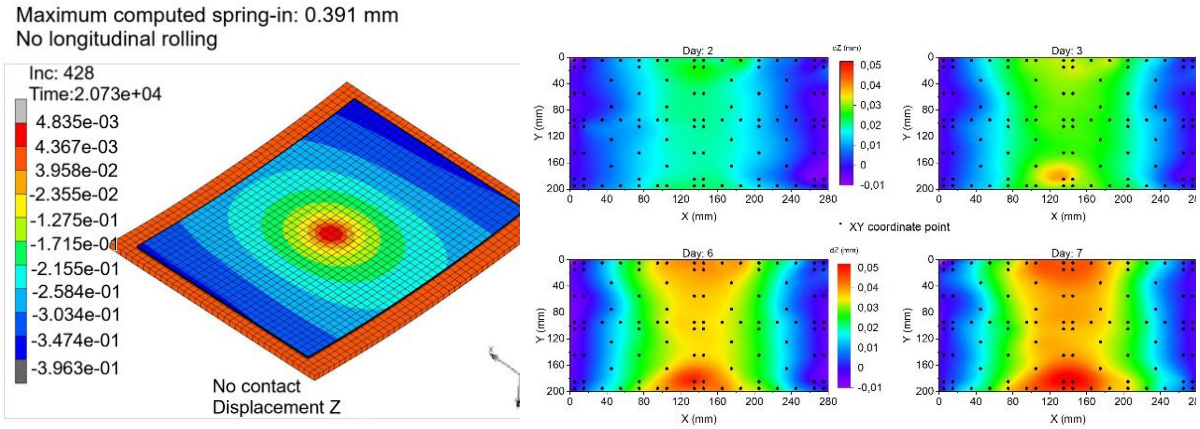


(**a**) (**b**)

**Figure 5.8**. (***a***) Calculated graph of the spring-in displacement for an 80-layer shell (Skin3); (***b***) CMM measurement of an 80-layer shell (Skin3) over a period of 7 days.

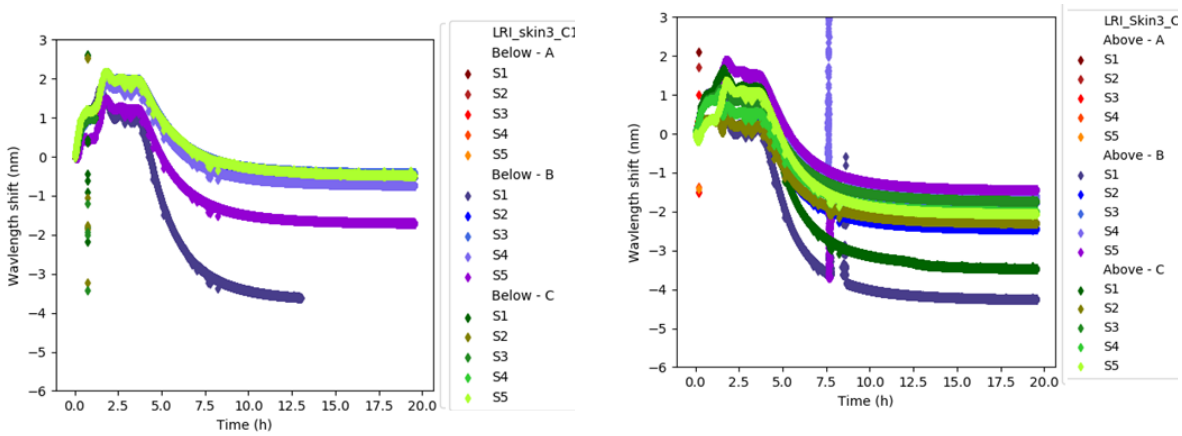


(**a**) (**b**)

**Figure 5.9**. FBG sensor response embedded during the manufacturing process of the Skin3 specimen: (a) bottom surface; (b) top surface.

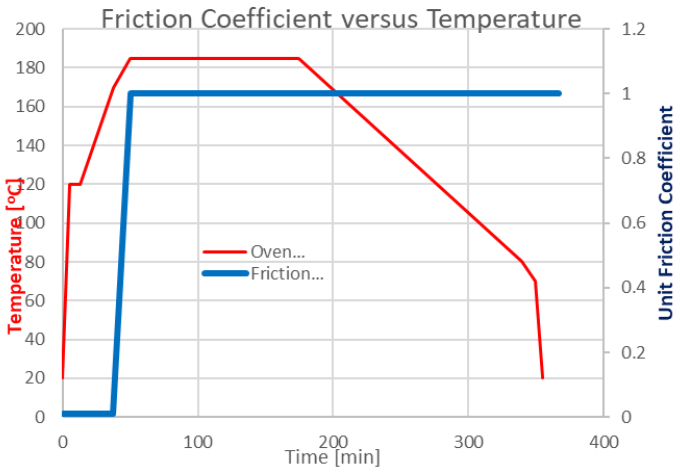


**Figure 5.10**. Friction coefficient evolution throughout the curing process

After simulating multiple scenarios and varying different types of parameters, the final and most suitable approach was chosen due to its accurate predictions of the spring-in phenomenon:

- Defining and incorporating the resin gel point in the simulation was essential for the accuracy of the results;
- Defining a constant fiber volume fraction showed better results compared to the measured specimens, even though the initial approach suggested a possible model adjustment by varying this parameter;
- Defining a variable friction coefficient was dependent on the resin gel point.

Figure 5.11 presents the results obtained using FBG sensors embedded in a C-spar2 specimen. As with the skin-type specimens, it is possible to identify the manufacturing phases through strain measurements.

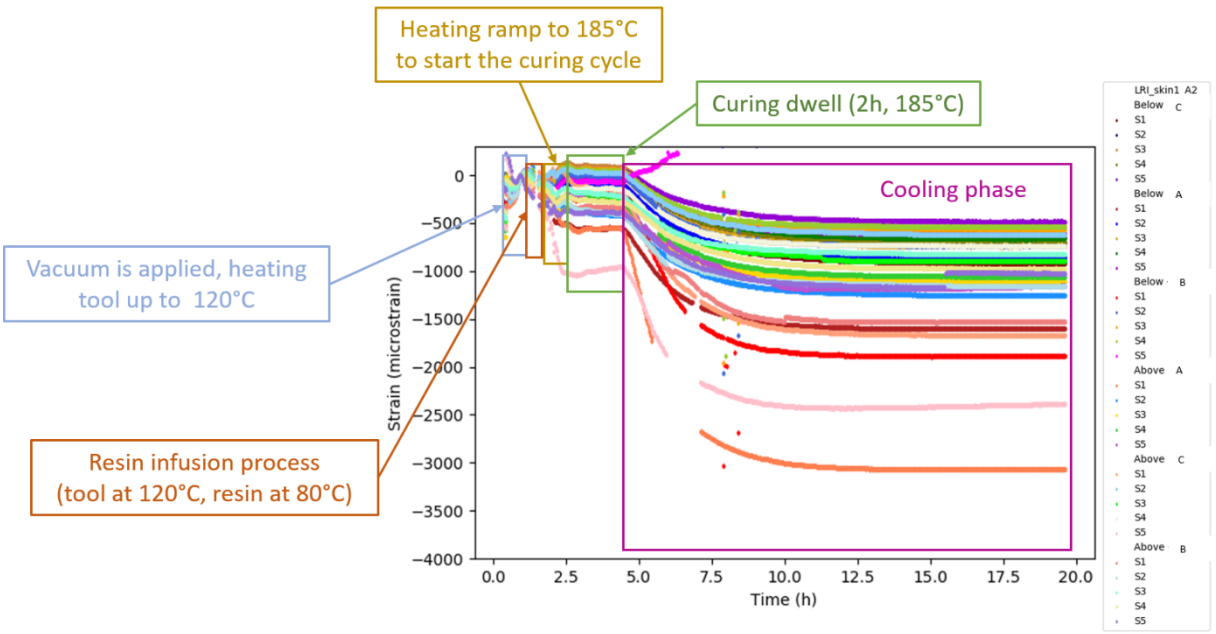


**Figure 5.11**. *Strain monitoring results using FBG sensors for the entire LRI curing cycle of a C-spar2 specimen.*

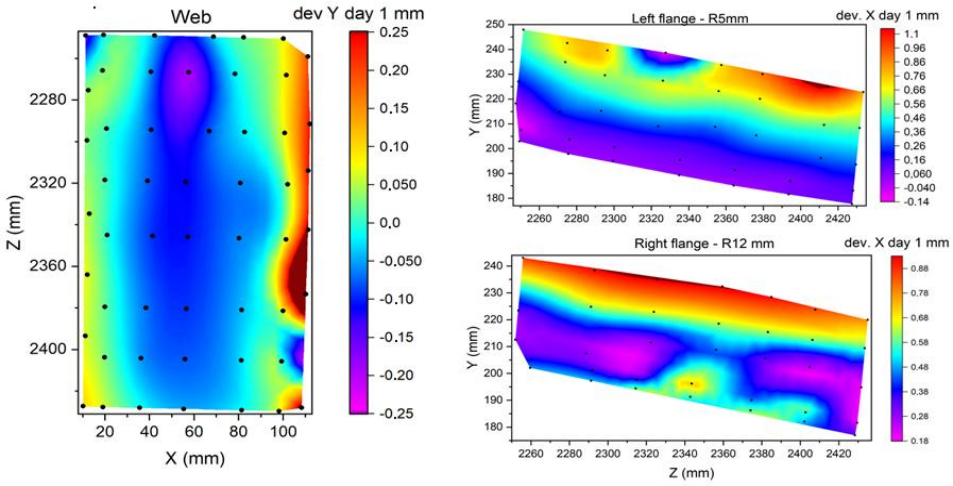


**Figure 5.12**. Contour plots by 3D CMM measuring for evaluating shape distortions on the web and flanges with R 12 mm and R 5 mm of a C-spar2 specimen.

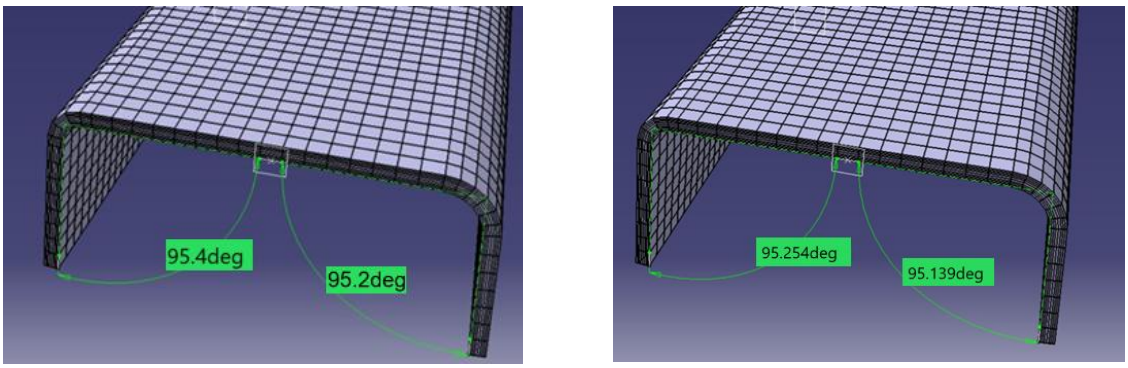


(**a**) (**b**)

**Figure 5.13**. *(**a**) Measurement of the theoretical geometry angle. (**b**) Measurement of the calculated deformation angle due to spring-in.*

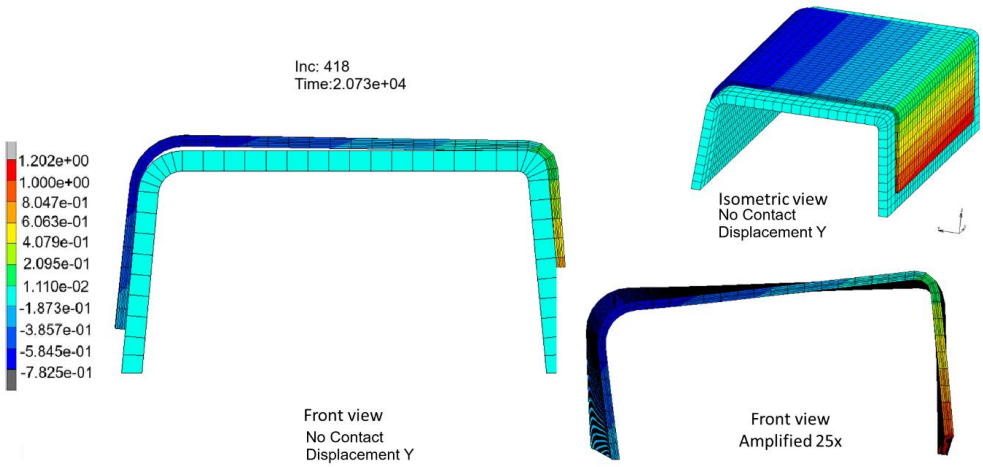


**Figure 5.14**. *Distortion graph calculated for the C-specimen with a thickness of 3 mm.*

After the fabrication and measurement of the C-spar specimen, the data presented in Figure 5.11 were used as a reference for evaluating the simulated numerical distortion values. We completed the experimental and numerical distortion results for numerical comparison in Tables 5.1–5.3. See Figures 5.13 and 5.14 for the numerical results.

**Table 5.1**. Results summary for 2.5mm thick C-spar specimen – measured and computed values.

| | **Corner radius 5 mm** | **Corner radius 12 mm** | **Time of measurement** |
|---|---|---|---|
| **C profile angles** (°) | 95.2 | 95.4 | |
| **Mean experimental angle** (°) | 93.511 | 93.58 | In the day of the manufacturing |
| **Mean experimental angle** (°) | 93.51 | 93.537 | 3 days after manufacturing |
| **Measured spring-in angle** (°) | 1.69 | 1.863 | |
| **Computed spring-in angle** (°) | 93.618 | 93.5704 | |
| **Computed spring-in distortion** (°) | 1.582 | 1.8296 | |

**Table 5.2**. Results summary for 3mm thick C-spar specimen – measured and computed values.

| | **Corner radius 5 mm** | **Corner radius 12 mm** | **Time of measurement** |
|---|---|---|---|
| **C profile angles** (°) | 94.970 | 94.810 | |
| **Mean experimental angle** (°) | 93.821 | 93.702 | In the day of the manufacturing |
| **Mean experimental angle** (°) | 93.813 | 93.693 | 3 days after manufacturing |
| **Measured spring-in angle** (°) | 1.16 | 1.12 | |
| **Computed spring-in angle** (°) | 93.645 | 93.679 | |
| **Computed spring-in distortion** (°) | 1.325 | 1.131 | |

**Table 5.3**. Results summary for 5mm thick C-spar specimen – measured and computed values.

| | **Corner radius 5 mm** | **Corner radius 12 mm** | **Time of measurement** |
|---|---|---|---|
| **C profile angles** (°) | 94.970 | 94.810 | |
| **Mean experimental angle** (°) | 93.943 | 93.62 | In the day of the manufacturing |
| **Mean experimental angle** (°) | 94.128 | 93.518 | 3 days after manufacturing |
| **Measured spring-in angle** (°) | 0.842 | 1.292 | |
| **Computed spring-in angle** (°) | 93.706 | 93.787 | |
| **Computed spring-in distortion** (°) | 1.264 | 1.023 | |

## 5.3 RESULTS ANALYSIS

In the calibration phase, which was initially carried out for the skin specimens, several parameters were varied and their impact on the spring-in displacement was evaluated:

- Varying the fiber volume fraction across the laminate thickness from 52% to 56% led to a reduction of 0.15 mm in displacement value;
- A constant fiber volume fraction across the laminate thickness caused an immediate response in the distortion behavior of the laminate, reducing the maximum displacement to 0.39 mm;
- Additional improvement through model calibration was achieved by applying a variable friction coefficient between the part and the mold. The parameter values were set to 0.01 before the gel point and 0.1 after the gel point threshold. This step did not affect the deflection value;
- An experiment that further reduced the calculated spring-in displacement involved modifying the initial degree of resin cure and applying a constant (high) friction coefficient of 1. The resulting calibration reduced the maximum displacement to 0.37 mm, which was considered acceptable, as no other calibration methods showed significant improvements compared to the test measurements;
- In previous research [***BC5.21***], it was shown that the friction coefficient values could reasonably be set lower (0.2–0.5), together with the implementation of an orthotropic friction behavior between the part and the mold. Given the near-isotropic layup configuration of the studied laminates, we considered this option to have a limited impact on distortion within the scope of the experimental and numerical tests [***BC5.22***].

When evaluating the spring-in angles, several notable findings were observed:

- Both in the experiments and in the simulations, the spring-in angle increased with larger corner radii. For a 3 mm thick specimen, the average increase in the spring-in angle was 1.34° (1.78%) for a 12 mm corner radius. For the same specimen, a 5 mm corner radius resulted in only a 1.03° (1.34%) increase. In conclusion, experimentally measured distortion shows that spring-in is more pronounced for larger corner radii, requiring more careful compensation measures.
- The web of the C-shape specimen exhibited deformation in both measurements and simulations. This behavior was initially observed in the skin specimen simulations and experimental trials. It is critical to note that the curvature axis will differ for parts that are stiffer due to their design geometry. The simulation strategy must account for the inherited geometric stiffness when simulating geometries more complex than flat or slightly curved panels.
- Given that the specimens were monitored for two weeks after the manufacturing cycle (without post-curing), they showed only minor variations in internal residual stress, which in turn led to minor distortion changes. The research team acknowledged this, but since the displacement variation over the monitoring period was very small, the post-curing behavior of the laminate was excluded from the simulation strategy.
- The fact that the simulation results were very close to the experimental values, as summarized in Tables 5.10–5.12, is remarkable and encouraging for the research effort.

A numerical simulation tool capable of predicting distortion in complex shapes is a valuable asset when designing complex molds. Such a simulation tool can be integrated into the overall design framework for composite structures and molds for composite structures in the following phases:

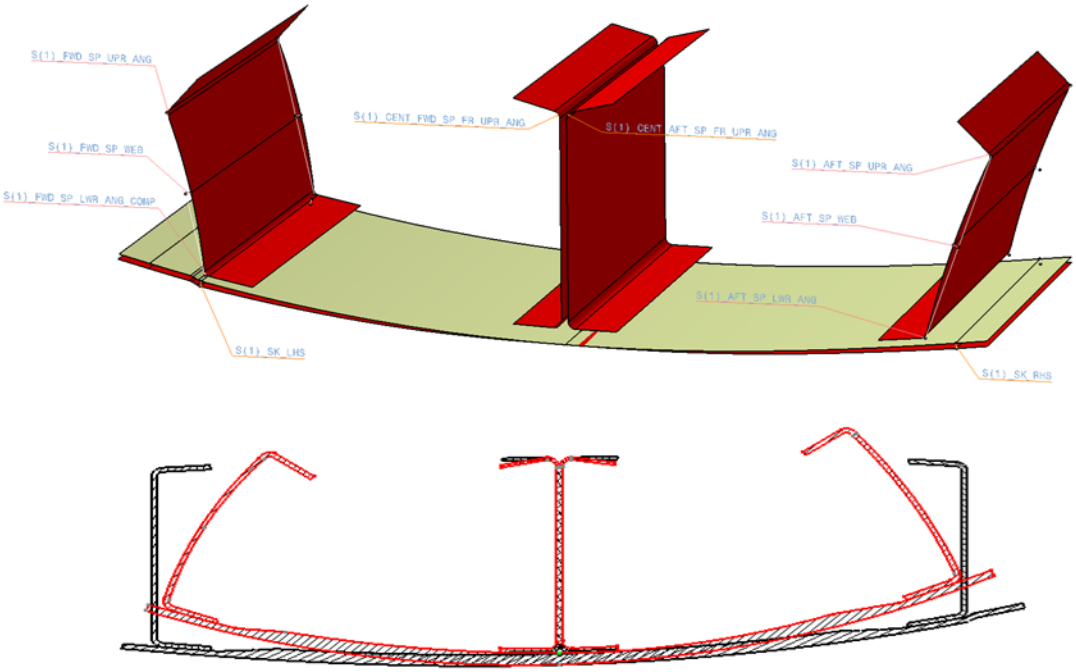


**Figure 5.15**. *Spring-in scenario for a co-cured aero-structure – skin and spars.* [***BC5.22***].

## REFERENCES CHAPTER 5

**[BC5.1]** Banu, C.; Bugaru, M. Development of a Numerical Tool for Laminate Composite Distortion Computation Through a Dual-Approach Strategy. Appl. Sci. 2024, 14(22), 10656; https://doi.org/10.3390/app142210656

**[BC5.2]** Clean Sky 2 ELADINE Project in the Frame of H2020 Frame Program. Disponibil online: https://eladine-project.eu/ (accesat în 20 September 2024).

**[BC5.3]** Clean Sky 2 OPTICOMS Project in the Frame of H2020 Frame Program. Disponibil online: https://opticoms-horizon2020.com/ (accesat în 20 September 2024).

**[BC5.4]** Torre-Poza, A.; Pinto, A.M.R.; Grandal, T.; González-Castro, N.; Carral, L.; Travieso-Puente, R.; Rodríguez-Senín, E.; Banu, C.; Paval, A.; Bocioaga, M.; et al. ELADINE: Sensor monitoring and numerical model approach for composite material wing box shape distortions prediction. *IOP Conf. Ser. Mater. Sci. Eng.* **2022**, *1226*, 012001.

**[BC5.5]** ESI PAM DISTORTION Simulation Module. Disponibil online: https://www.esi.com.au/software/pamdistortion (accesat în 31 October 2024).

**[BC5.6]** ALTAIR Advanced Cure Simulation. Disponibil online: https://altair.com/advanced-cure-simulation (accesat în 31 October 2024).

**[BC5.7]** ANSYS Composite PrepPost Simulation Module. Disponibil online: https://www.ansys.com/resource-center/white-paper/simulating-composite-structures (accesat în 31 October 2024).

**[BC5.8]** ABAQUS/STANDARD Nonlinear Solver. Disponibil online: https://www.3ds.com/products/simulia/abaqus/standard (accesat în 31 October 2024).

**[BC5.9]** COMSOL Multiphysics Nonlinear Structural Materials Module. Disponibil online: https://www.comsol.com/nonlinear-structural-materials-module (accesat în 31 October 2024).

**[BC5.10]** MSC Marc Advanced Nonlinear Simulation Solution. Disponibil online: https://hexagon.com/products/marc (accesat în 31 October 2024).

**[BC5.11]** Nelson, R.H.; Cairns, D.S. Prediction of dimensional changes in composite laminates during cure. In Proceedings of 34th International SAMPE symposium and exhibition, Reno, NV, USA, 8–11 May 1989; Volume 34, pp. 2397–24104.

**[BC5.12]** Radford, D.W.; Diendorf, R.J. Shape instabilities in composites resulting from laminate anisotropy. *J. Reinf. Plast. Compos.* **1993**, *12*, 58–75. https://doi.org/10.1177/073168449301200104.

**[BC5.13]** Radford, D.W. Volume fraction gradient induced warpage in curved composite plates. *Compos. Eng.* **1995**, *5*, 923–934. https://doi.org/10.1016/0961-9526(95)00033-J.

**[BC5.14]** Johnston, A. An Integrated Model of the Development of Process-Induced Deformation in Autoclave Processing of Composite Structures. Ph.D. Thesis, The University of British Columbia, Vancouver, BC, Canada, 1997.

**[BC5.15]** Hubert, P.; Johnston, A.; Poursartip, A.; Nelson, K. Cure Kinetics and Viscosity Models for Hexcel 8552 Epoxy Resin. In Proceedings of the SAMPE Conference, Long Beach, CA, USA, 6–10 May 2001.

**[BC5.16]** Bogetti, T.A.; Gillespie, J.W., Jr. *Influence of Cure Shrinkage on Process-Induced Stress and Deformation in Thick Thermosetting Composites*; Technical report BRL-TR-3182; Army Ballistic Research Lab: Aberdeen Proving Ground, MD, USA, 1992.

**[BC5.17]** White, S.R.; Hahn, H.T. Process Modeling of Composite Materials: Residual Stress Development during Cure. Part I. Model Formulation. *J. Compos. Mater.* **1992**, *26*, 2402–2422. https://doi.org/10.1177/002199839202601604

**[BC5.18]** Nawab, Y.; Shahid, S.; Boyard, N.; Jacquemin, F. Chemical shrinkage characterization techniques for thermoset resins and associated composites. *J. Mater. Sci.* **2013**, *48*, 5387–5409. https://doi.org/10.1007/s10853-013-7333-6.

**[BC5.19]** Digimat Hexagon. Disponibil online: https://hexagon.com/products/digimat (accesat în 20 September 2024).

**[BC5.20]** *MSC Software–MARC 2017.1–VOLUME A: Theory and User Information*; MSC Software: Newport Beach, CA, USA, 2017; pp. 945–954.

**[BC5.21]** Yuksel, O.; Çınar, K.; Ersoy, N. Experimental and numerical study of the tool-part interaction in flat and double curvature parts. In Proceedings of the ECCM17-17th European Conference on Composite Materials, Munich, Germany, 26–30 June 2016.

**[BC5.22]** Wucher, B.**;** Martiny, P.; Lani, F.; Pardoen, T. An example of mold compensation by means of numerical simulation on a generic curved CFRP C-spar. In Proceedings of the ECCM15–15th European Conference on Composite Materials, Venice, Italy, 24–28 June 2012.
**[BC5.23]** Clean Sky 2 FITCOW Project in the Frame of H2020 Frame Program. Disponibil online: https://cordis.europa.eu/project/id/831985/results/ (accesat în 20 September 2024).

# 6. RESEARCH ON THE PREDICTION OF GEOMETRIC DISTORTIONS INDUCED BY RESIDUAL STRESSES GENERATED IN THE DEVELOPMENT OF ANISOTROPIC MULTILAYERED STRUCTURES USED IN THE AEROSPACE INDUSTRY USING NUMERICAL SIMULATIONS

## 6.1 DISTORTION SIMULATION ON A SCALED SPECIMEN

### 6.1.1 CONTEXT

The technological and scientific developments described in this article were carried out within the project titled *Evaluation of Composite Laminate Distortion through an Integrated Numerical-Experimental Approach – ELADINE* [***BC6.1***]. This project represented a support activity (CfP) for the OPTICOMS project [***BC6.2***], carried out under the European Clean Sky 2 program..

### 6.1.2 STRATEGY OF THE WORK AND PRELIMINARY CONSIDERATIONS

Both the experimental program and the development of the simulation tool were carried out using two material systems:

I. Toray P707AG-15 prepreg, unidirectional tape, and resin system 2510;
II. Hexcel Dry Fiber Hi Tape, unidirectional tape, and resin system RTM 6-2.

During manufacturing, optical sensors were incorporated at strategic positions both in the materials and in the molds:

- SFBG (strain FBG sensors) – FBG sensors for measuring deformations;
- TFBG (temperature FBG sensors) – FBG sensors for measuring temperature;
- DFS (dielectric flow sensors) – dielectric sensors for monitoring resin flow;
- DCS (dielectric curing sensors) – dielectric sensors for monitoring the curing process.

A vast set of data regarding the materials' behavior during polymerization was obtained, ranging from simple flat specimens to more complex C-shaped specimens with two distinct flange and web radii. Post-polymerization measurements of the specimens and fabricated samples represented the final step for calibrating and fine-tuning the numerical model, ensuring that the simulation tool could accurately reproduce each of the geometries analyzed.

**Figure 6.1**. *The full-scale aeronautical structure simulated for distortion prediction: LEFT - Piaggio P180 aircraft wing, TOP RIGHT - mold for the full skin and spars, BOTTOM RIGHT - 7-meter part fabricated and demolded from the mold.*

### 6.1.3 CO-CURING

The traditional manufacturing solution used for aircraft composite structures involves assembling two or more individually polymerized parts through mechanical fastening (such as riveting and/or bolting) or adhesive bonding. Although mechanical fastening is a well-understood method by engineers, it remains an undesirable solution as it generates discontinuities in the reinforcement network and promotes delamination.

### 6.1.4 MATERIALS

Regarding the materials used, the molds are made from LTM 12 [BC6.4], a molding prepreg produced by Solvay. In addition to having a reasonable work time at ambient temperature (after being taken out of the freezer), this prepreg allows polymerization at low temperatures over a relatively short period (five hours at 70°C), while also having a maximum operating temperature of 200°C. Polymerizing the molds at low temperatures is essential to reduce differences in thermal expansion (differences in thermal expansion coefficients - CTE) between the temperature at which the epoxy model (master mold) was processed and the temperature required for mold polymerization.

### 6.1.5 DISTORTION ISSUES AND DEMOULDING

One of the main challenges in manufacturing the demonstrator at scale [BC6.3] is reducing the geometric distortion of composite parts. Spring-in is the complex result of residual stresses developed in the manufactured part, influenced by numerous parameters and complex interactions. The increasing complexity of the design has led to the need for the development of compensation algorithms, capable of being implemented in complex geometries and under various polymerization conditions.

### 6.1.6 NUMERICAL SIMULATION ON THE DOWNSCAALE DEMONSTRATOR

By applying the numerical modeling methods perfected earlier and presented in Chapter 5, we modeled the assembly subjected to the polymerization cycle to determine, through

numerical simulation, the distortions of the demonstrator specimen at the end of the manufacturing process [***BC6.13, BC6.14***].

### *6.1.6.1. Geometry*

In the figure 6.2, the 1,2 m downscale demonstrator CAD assy is presented.

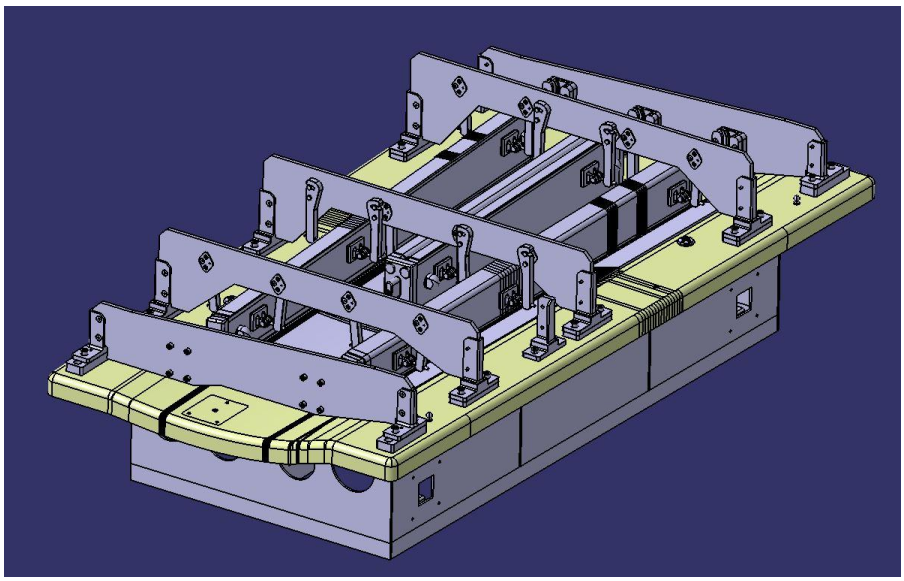

**Figure 6.2** *1.2m downscale demo – CAD assy.*

### *6.1.6.2. Finite elements meshing*

The geometry, with all its components, presents a high level of complexity; therefore, simplifications are necessary. Figure 6.3 shows the simplified model. The skin mold was defined as a surface on which, considering all the geometric constraints (all the parts and molds will be designed on this surface), an effortless design of the adjacent meshing will be allowed.

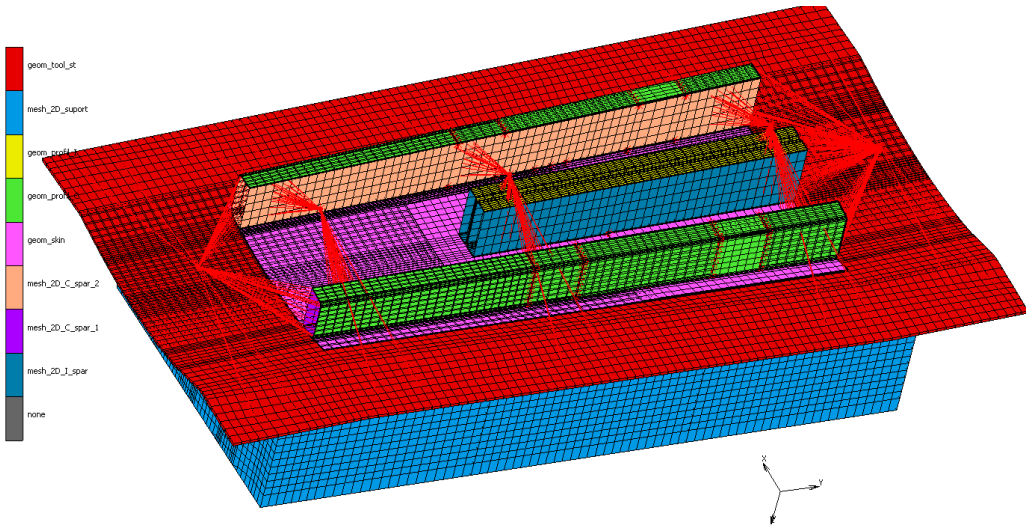


**Figure 6.3** *Downscale demonstrator FEM model*

### *6.1.6.3. Materials properties*

In the finite element model, the total thickness of the composite was divided into several "slices" of finite elements. Internally, each "slice" of finite element is divided into the corresponding composite layers, according to the stacking sequence of the composite defined in the design. Even though, from a geometric perspective, the model is not symmetric, the configuration of the finite element "slices" and the segmentation of the associated layers on the "slice" of the element are symmetric in the model.

### *6.1.6.4. Boundary conditions*

- The thermal component, with material thermal properties such as conductivity, thermal contact, specific heat, thermal loads such as convection between the part and oven temperature;
- Polymerization, with parameters that describe the evolution of polymerization over time and temperature;
- The structural component, with material structural properties that depend on the degree of polymerization, polymerization-associated shrinkage, structural thermal expansion, and structural contact.

### *6.1.6.5. Initial conditions*

For the numerical modeling approach, the start of the simulation was considered to be after the gel point in the polymerization process [***BC6.17***]. To simulate this approach, based on experimental data, two initial conditions were considered:

- The oven temperature after the gel point;
- The degree of polymerization after the gel point.

This approach for the initial conditions takes into account the resin shrinkage [***BC6.18, BC6.19***] during polymerization both before and after the start of the numerical simulation of the process, considering the shrinkage as a function of the degree of polymerization. Additionally, by using this numerical approach, the period before the gelation point, when the material has practically no rigidity, is eliminated.

### *6.1.6.6. Uncalibrated results – LRI*

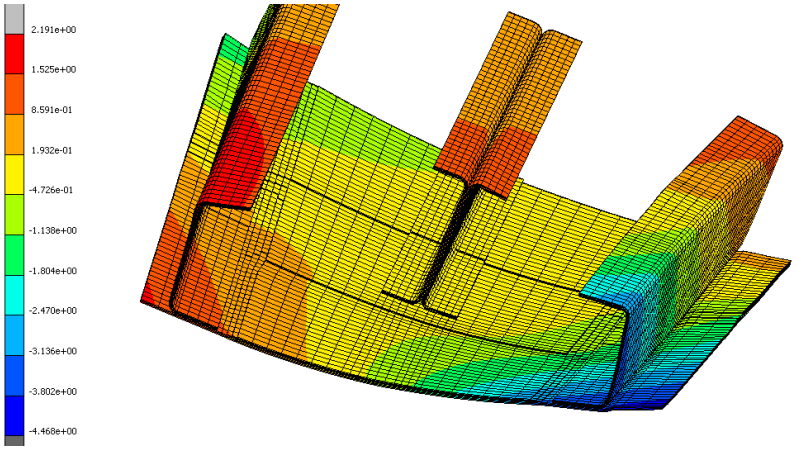


**Figure 6.4**. *Distortions of the demonstrator amplified by 10 times. Color map of displacements in the Z direction* ***[BC6.13, BC6.14]***

Additional calibration actions::

- Increasing the total volumetric contraction of polymerization in the experimental data: from 2% to 5-6%. This value is a target value. This means that if, at the end of the process, the degree of polymerization of the resin is 100%, the total contraction becomes 5-6%. In reality, the degree of polymerization is lower. This will result in a lower polymerization contraction value. This calibration action is in accordance with the document: RHEOLOGICAL RESULTS OF RTM6 RESIN: Polymerization Contraction Test Report: 2020/38-TR-Lb-03 dated 29/10/2020, prepared within the ELADINE project;
- Verifying the numerical stability of the model;
- Verifying the distortion of the model against experimental data and measurement results.

### *6.1.6.7. Uncalibrated results - prepreg*

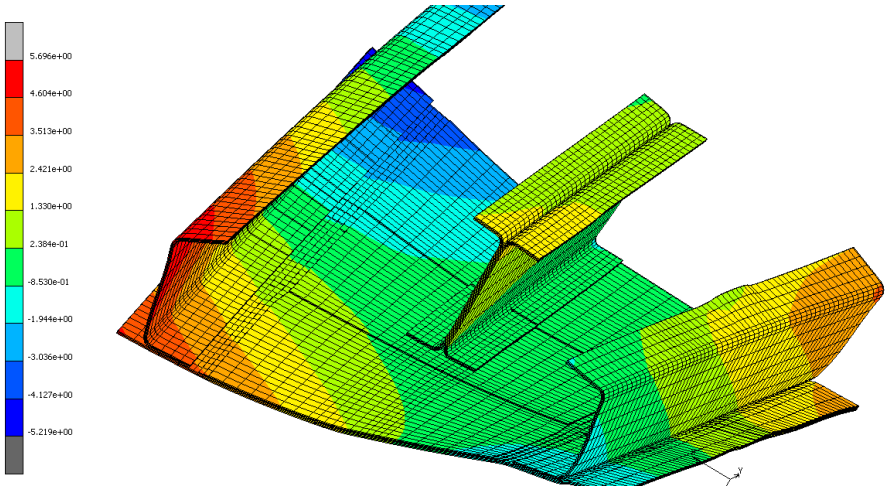


**Figure 6.5**. *Distortions of the demonstrator amplified by 10 times. Color map of displacements in the Z direction* ***[BC6.13, BC6.14]***

Additional calibration actions:

- Increasing the degree of polymerization at the end of the process from 74.8% to the target experimental value of 75-77%;
- Increasing the total volumetric contraction of polymerization to 3-4%;
- Verifying the distortion of the model against experimental data and measurement results;

### 6.1.6.8. Calibrated results

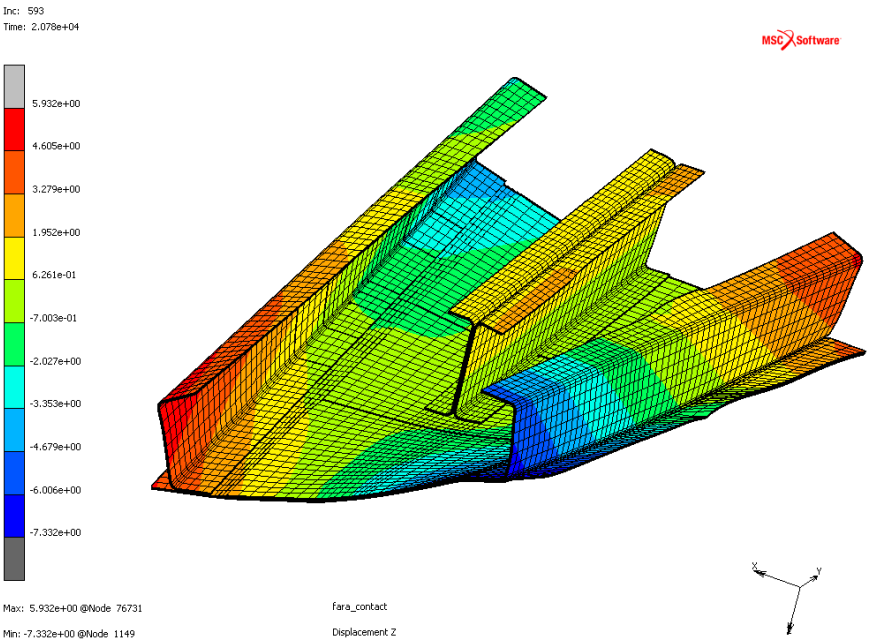


**Figure 6.6** *Calibrated LRI. Distortions of the demonstrator amplified 10 times. Color map of displacements in the Z direction. The distortions are larger in the calibrated model [**BC6.13, BC6.14**]*

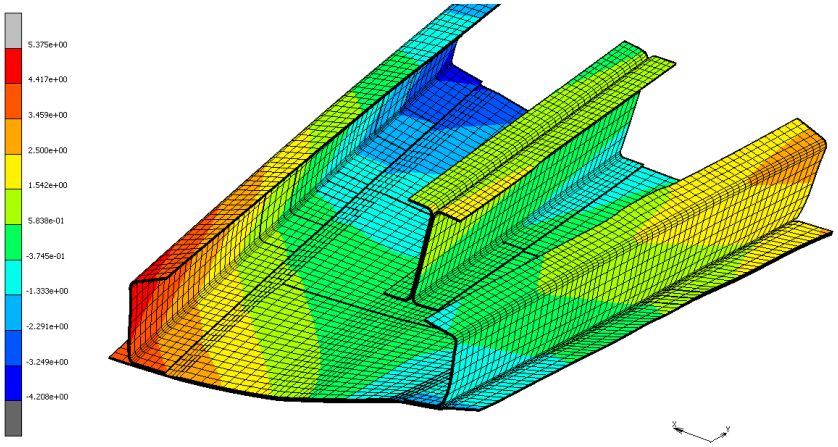


**Figure 6.7** *Calibrated prepreg. Distortions of the demonstrator amplified 10 times. Color map of displacements in the Z direction. The distortions are larger in the calibrated model [**BC6.13, BC6.14**]*

### 6.1.6.9. Conclusions for the downscale demonstrator simulations

The importance of this numerical model lies in the role it plays in the development flow of the numerical simulation tool. The complexity of the model is obviously greater than that of specimens with simple geometries, but the size of the model (the number of elements and nodes) is smaller than that of the 7m wing model [BC6.13, BC6.14]. The position of this scaled model (1.2m) in the development flow of the numerical tool—small in size and large in complexity—provides us with the opportunity to better understand the effects of certain elements:

- Discretization technique: The model consists solely of hexahedral brick elements divided into several connected "slices";
- Element type: The element used in the model is a nonlinear element. This element, as a unique entity, can be divided into layers to model composite materials. The thermal behavior of the element is nonlinear because each layer has its own integration point. The structural behavior of the element is likely linear because the element only has 8 nodes, its vertices, without intermediate nodes;
- Loads, boundary conditions, and contacts: All these components significantly affect the accuracy and numerical stability of the model. They influence both the accuracy and stability by how they are placed, and also by the moment in the simulation process when they become active or inactive;
- **Calibration**: To understand the parameters of the numerical model that can calibrate the model according to the experiment, and how these parameters affect the results and numerical stability.

The conclusions from this small-scale model have provided the opportunity to advance towards the large-scale model.

### *6.1.6.10. Downscale demonstrator measurements*

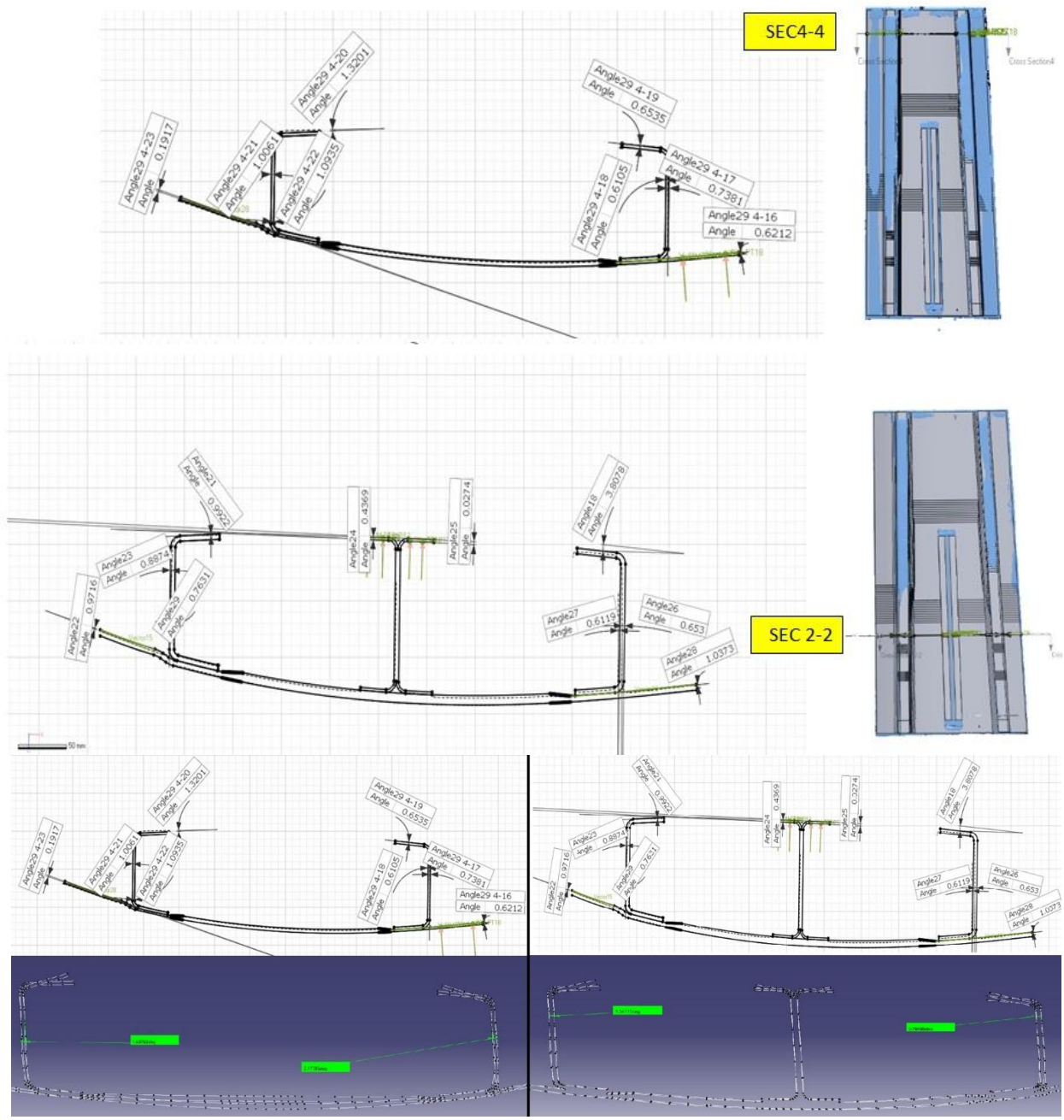


Section 4-4 A: Measured angle 0.7381 deg. Computed Angle 2.172 deg

Section 4-4 A: Measured angle 0.6119 deg. Computed Angle 0.7845 deg

Section 4-4 B: Measured angle 1.0935 deg. Computed Angle 1.537 deg

Section 4-4 B: Measured angle 0.7631 deg. Computed Angle 1.341 deg

**Figure 6.8** *3D scanning and comparison of deviations (measurements-calculation) in two sections of the 1.2m part [**BC6.13**]*

## 6.2 DISTORTION SIMULATIONS OF THE 7 METER WING

Considering that the simulation of the demonstrator – a 7-meter composite wing box – will use the methodology already detailed in the second chapter of this study, in this chapter we will limit ourselves to describing the geometry of the 7-meter demonstrator, the molds, and the simulation results.

### 6.2.1 GEOMETRY AND FEM

For the development of the simulation tool, the first step in analyzing the distortion of the full-scale demonstrator was the inspection of the CAD model to define a modeling approach that would be reliable in simulating the polymerization process.

### 6.2.2 SIMULATION RESULTS AND ANALYSIS

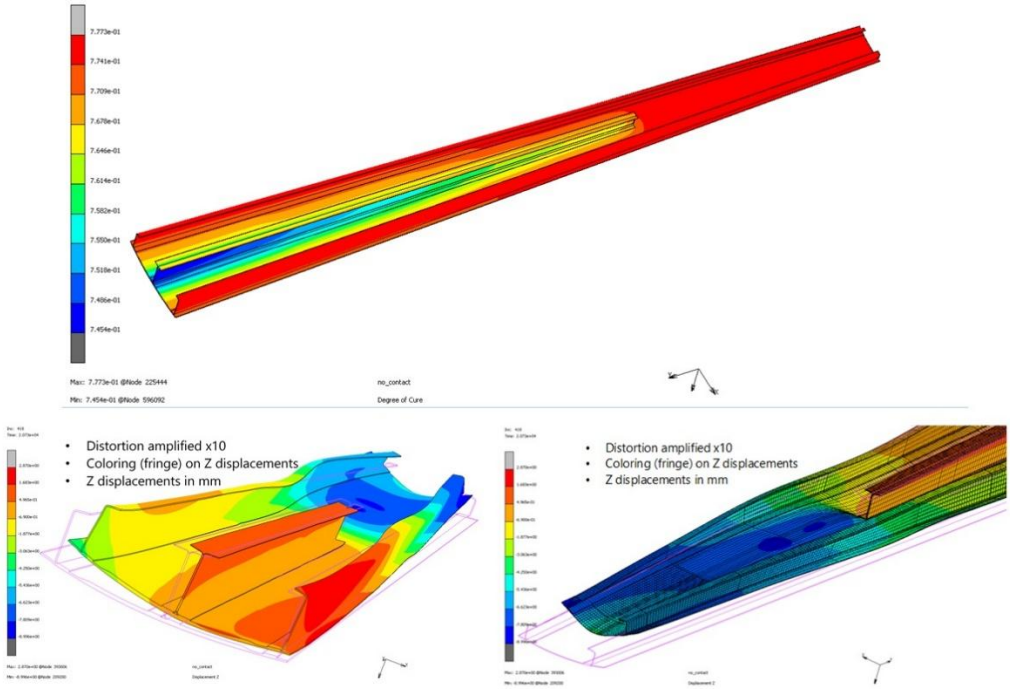


**Figure 6.9** *Simulation of a 7m wing. TOP – map of the polymerization degree gradients. BOTTOM – snapshots of the distortion graph from both ends of the simulated part.* ***[BC6.14]***

The transition from a simple geometry to a complex part presented new challenges for the simulation model. Although the accuracy of the distortion results was quite good after the calibration step, the trend and pattern of the distortion were replicated by the numerical model with very good fidelity [***BC6.14***].

Several very important lessons were learned after scaling the numerical model for a complex structure:

- Discretization technique: The model consists only of hexahedral brick elements divided into multiple connected sections;
- Element type: The element used in the model is a nonlinear element. This element, as a single entity, can be divided into layers to model composite materials. The thermal behavior of the element is nonlinear because each layer has its own integration point.

The structural behavior of the element is likely linear because the element has only 8 nodes at the vertices, without intermediate nodes;

- Loads, constraints, and contacts: All these components significantly affect the accuracy and numerical stability of the model. They affect accuracy and stability both by how they are applied and when they become active or inactive during the simulation process;
- Before calibration: Spar-type parts show spring-in of the flanges in the range of 0.3mm to 2.18mm [distortion along the Z direction]. The skin section of the part shows a different deformation pattern compared to the test specimens of the skin.
- Calibration: The parameters of the numerical model that could calibrate the model according to the experiment, and how these parameters affect the results and numerical stability, require further investigation.

The 7m wing was not 3D scanned, and we could not compare the calculated distortion results with the deviations from the real scenario. The first conclusion that can be drawn is the comparison with previous work carried out on smaller structures manufactured using the same process and materials, which is a very valuable lesson in itself. Heating and cooling the large-scale structure results in a much higher temperature gradient across the entire structure, which leads to a stronger influence of temperature variation on the polymerization degree gradient. For a real manufacturing operation, additional mold elements are considered, adding extra mass to the global model, which cannot be simplified in simulations. A decision to simplify the model and exclude heavy elements could lead to inaccuracies in the spring-in results.

Given that our study considered two material systems, we can conclude that for the Liquid Resin Infusion (LRI) manufacturing method, the final polymerization degree is in the range of 92.4% to 95.8%, while for the prepreg manufacturing method, the range is between 71.2% and 74.5%. Compared to previous simulations at the test specimen level for composite material and small-scale demonstrators, the degree variation is greater. The average gradient of the polymerization degree in both manufacturing processes is approximately identical: 3.4%. This particular variation in the polymerization degree can be attributed to the larger size of the part in certain sections, and the larger mass of the metallic features at the ends. The increased size of the area subjected to the convection and conduction process will increase and influence the heating process, which will take longer, resulting in an uneven temperature distribution, and consequently, an uneven polymerization degree distribution.

Regarding the differences between the two manufacturing methods, even though the degree variation is similar, the final polymerization degree is 21.3% higher for the LRI method compared to the prepreg manufacturing method.

Distortions in the LRI method range from -8.99mm to 2.87mm, while for the prepreg manufacturing method, the range is between -8.01mm and 3.55mm.

In the simulations of both manufacturing processes, the final geometry of the part is similar. Also, in the final geometry of the part, a combination of spring-in and spring-out of the skin

across the entire part can be observed. For I-Spar, as expected, spring-in values of 1-2mm are observed for the upper flanges.

In the numerical analysis, the polymerization degree at the end of the process differs between the LRI method and the prepreg method. The polymerization degree obtained for the prepreg method is lower than the polymerization degree obtained for the LRI method. As a result, the distortion of the part differs between the two methods. For the LRI method, the distortion is higher than for the prepreg method.

## REFERENCES CHAPTER 6

**[BC6.1]** Clean Sky 2 ELADINE Project in the Frame of H2020 Frame Program. Disponibil online: https://eladine-project.eu/ (accesat în 20 September 2024).
**[BC6.2]** Clean Sky 2 OPTICOMS Project in the Frame of H2020 Frame Program. Disponibil online: https://opticoms-horizon2020.com/ (accesat în 20 septembrie 2024).
**[BC6.3]** FITCoW - Full-scale Innovative integrated Tooling for Composite material Wing-box. Disponibil online: https://cordis.europa.eu/project/id/831985/results (accesat în 20 septembrie 2024).
**[BC6.4]** Disponibil online: https://www.solvay.com/sites/g/files/srpend221/files/2021-01/Solvay-Tooling-Brochure-2021-01.pdf (accesat în februarie 2025).
**[BC6.5]** Wisnom, M.R.; Gigliotti, M.; Ersoy, N.; Campbell, M.; Potter, K.D. Mechanisms generating residual stresses and distortion during manufacture of polymer-matrix composite structures. *Compos. A Appl. Sci. Manuf.* **2006**, *37*, 522–529. https://doi.org/10.1016/j.compositesa.2005.05.019.
**[BC6.6]** Parlevliet, P.P.; Bersee, H.E.N.; Beukers, A. Residual stresses in thermoplastic composites—A study of the literature—Part I: Formation of residual stresses. *Compos. A Appl. Sci. Manuf.* **2006**, *37*, 1847–1857. https://doi.org/10.1016/j.compositesa.2005.12.025
**[BC6.7]** Parlevliet, P.P.; Bersee, H.E.N.; Beukers, A. Residual stresses in thermoplastic composites—A study of the literature—Part II: Experimental techniques. *Compos. A Appl. Sci. Manuf.* **2007**, *38*, 651–665. https://doi.org/10.1016/j.compositesa.2006.07.002.
**[BC6.8]** Parlevliet, P.P.; Bersee, H.E.N.; Beukers, A. Residual stresses in thermoplastic composites—A study of the literature—part III: Effect of thermal residual stresses. *Compos. A Appl. Sci. Manuf.* **2007**, *38*, 1581–1596. https://doi.org/10.1016/j.compositesa.2006.12.005.
**[BC6.9]** Ito, Y.; Obo, T.; Minakuchi, S.; Takeda, N. Cure strain in thick CFRP laminate: Optical-fiber-based distributed measurement and numerical simulation. *Adv. Compos. Mater.* **2015**, *24*, 325–324. https://doi.org/10.1080/09243046.2014.906914.
**[BC6.10]** Twigg, G.; Poursartip, A.; Ferlund, G. An Experimental Method for Quantifying Tool-part Shear Interaction during Composites Processing. *Compos. Sci. Technol.* **2003**, *63*, 1985–2002. https://doi.org/10.1016/S0266-3538(03)00172-6.
**[BC6.11]** Twigg, G.; Poursartip, A.; Ferlund, G. Tool-part Interaction in Composite Processing. Part I: Experimental Investigation and Analytical Model. *Compos. Sci. Technol.* **2004**, *25*, 121–133. https://doi.org/10.1016/S1359-835X(03)00131-3.
**[BC6.12]** Twigg, G.; Poursartip, A.; Ferlund, G. Tool-part Interaction in Composite Processing. Part II: Numerical Modelling. *Compos. Sci. Technol.* **2004**, *35*, 135–141. https://doi.org/10.1016/S1359-835X(03)00132-5.
**[BC6.13]** Banu, C.; Bocioaga, M. Shape distortion prediction of high temperature curing laminates through a transient multi-physics numerical model. In Proceedings of the AIAA SCITECH 2024 Forum, Orlando, FL, USA, 8–12 January 2024.
**[BC6.14]** Banu, C.; Bugaru, M. Development of a Numerical Tool for Laminate Composite Distortion Computation Through a Dual-Approach Strategy. Appl. Sci. 2024, 14(22), 10656; https://doi.org/10.3390/app142210656
**[BC6.15]** MSC Marc Advanced Nonlinear Simulation Solution. Available online: https://hexagon.com/products/marc (accessed on 31 October 2024).
**[BC6.16]** *MSC Software–MARC 2017.1–VOLUME A: Theory and User Information*; MSC Software: Newport Beach, CA, USA, 2017; pp. 945–954
**[BC6.17]** Torre-Poza, A.; Pinto A.M.R.; Grandal T.; González-Castro, N.; Carral, L.; Travieso-Puente, R.; Rodríguez-Senín, E.; Banu, C.; Paval, A.; Bocioaga, M.; et al. ELADINE: Sensor monitoring and numerical model approach for composite material wing box shape distortions prediction. *IOP Conf. Ser. Mater. Sci. Eng.* **2022**, *1226*, 012001
**[BC6.18]** Hubert, P.; Johnston, A.; Poursartip, A.; Nelson, K. Cure Kinetics and Viscosity Models for Hexcel 8552 Epoxy Resin. In Proceedings of the SAMPE Conference, Long Beach, CA, USA, 6–10 May 2001.
**[BC6.19]** Bogetti, T.A.; Gillespie, J.W., Jr. *Influence of Cure Shrinkage on Process-Induced Stress and Deformation in Thick Thermosetting Composites*; Technical report BRL-TR-3182; Army Ballistic Research Lab: Aberdeen Proving Ground, MD, USA, 1992.

# 7. ORIGINAL CONTRIBUTIONS REGARDING THE PREDICTION OF GEOMETRIC DISTORTIONS INDUCED BY RESIDUAL STRESSES GENERATED IN THE DEVELOPMENT OF MULTILAYERED ANISOTROPIC STRUCTURES USED IN THE AEROSPACE INDUSTRY

## 7.1 THEORETICAL ASPECTS

In the previous chapters, the strategies necessary for modeling the phenomena associated with manufacturing processes, such as thermokinetics, rheology, and viscous flows, were presented, with a subsequent focus on thermo-mechanical analysis. The three material constitutive models were introduced, models that have been extensively discussed in the specialized literature. Among these, the linear-elastic and the specific constitutive models provide better accuracy than the viscoelastic model, are easier to implement, and the characterization of the components is relatively accessible. The modified CHILE model is elegant, yet at the same time, it offers a straightforward approach to considering the nonlinear behavior of materials. [***BC1.45***].

## 7.2 EXPERIMENTAL ASPECTS

Complementarily, the monitoring of manufacturing processes using FBG optical sensors and dielectric sensors (DEA analysis) is designed to globally and locally describe the polymerization process, its parameters, and the variations of these parameters during fabrication. Considering that the variation in the degree of polymerization is one of the key factors in determining the appearance and distribution of residual stresses, it is clear that sensor-based monitoring methods have the most promising potential to provide the experimental data necessary for both calibrating numerical simulation methods and refining and developing the mathematical formalisms currently in use on this topic.

The major sensitivity of manufacturing process monitoring with sensors is both technical and cost-related. In order to provide reliable and high-quality data, sensor measurements require rigorous calibration and, in the case of optical sensors, greater care in instrumentation, given that they can easily break or disconnect during the handling of test specimens or 1:1 scale structures. Regarding costs, although both Bragg sensors and dielectric sensors can be purchased at very affordable prices, the costs of the acquisition equipment and data processing are high.

## 7.3 ORIGINAL PRACTICAL ASPECTS FOR THE EXPERIMENTAL DETERMINATION OF RESIDUAL STRESSES AND DEFORMATIONS

To study the effect of manufacturing parameters on the shape distortions of the final specimens, an experimental approach was conducted on three different geometries (shell

specimens, U-stringer, and shell-stringer assembly). The last geometry represents a sector of the primary wing structure.

For the experimental part, a combination of FBG sensors and DC sensors was used, as well as a 3D CMM analysis to monitor several parameters during different stages of specimen manufacturing and post-manufacturing. The experimental data collected from laboratory tests were used to calibrate and validate a numerical tool designed to predict the geometric distortions caused by residual stresses in anisotropic laminates.

The experimental strategy was designed to collect the maximum amount of information to better understand the parameters affecting shape distortions and to gather data that will lead to the development of a precise and accurate simulation method and tool capable of predicting composite part deformations.

With the sensor distribution scheme selected for the specimen fabrication, the following manufacturing process characteristics were detected and monitored:

- Resin arrival, minimum viscosity, gel point, and the end of the polymerization process were detected by DC sensors;
- A temperature gradient was detected by the FBG-temperature sensors placed on both surfaces of the specimen. A higher temperature was reached on specimens with more layers, but the temperature gradient was smaller compared to thinner specimens. Furthermore, on the surface in contact with the mold, higher temperatures were recorded for thicker specimens, while the surface in contact with the vacuum bag was the hottest on thinner specimens. It was concluded that this phenomenon occurs due to limitations in heat transfer on thicker specimens because there is more reinforcement material.
- FBG sensors for measuring strains were able to detect polymerization and thermal contraction due to the evolution of resin polymerization throughout the manufacturing cycle. Exclusive resin monitoring led to the conclusion that a better evaluation of deformation generated during the polymerization cycle was achieved by considering the gel point as the origin or zero coordinate of the deformation. Dry areas or areas with a lower resin content were also correlated with the strain sensor readings.
- The geometry analysis performed with the 3DCMM was correlated with the deformation recorded by the same sensors (where possible) that were used during manufacturing. This post-manufacturing monitoring was done immediately after demolding and over several days.
- A reduction in the curvature radius of the shell specimens was observed, as the 3DCMM measurements revealed distortions in the central part of the specimen;
- Areas with more shape distortions were also those with different strain values and different deformation evolutions several days after demolding. Therefore, 3DCMM is in agreement with the FBG response (strain);
- 3DCMM measurements showed that the greatest deformation of the specimen occurred immediately after demolding and in the first 3-4 days. After that, the specimen geometry remained stable. These results were consistent with strain sensors,

which recorded the greatest deformation evolution in the first days after tool release. However, the strain signal did not stabilize as the specimen shape did, but it was concluded that the remaining strain was not enough to cause significant distortions on the specimen. Case studies were conducted for different simulations for calibrating the numerical tool.

After comparing the experimental and numerical results, the main conclusions drawn for the shell specimens were:

- The variation in the degree of polymerization is close to the experimental data (around 95-96% both in the experimental trials and in the numerical model).
- The temperature variation is consistent with the temperature load (oven temperature).

After comparing the experimental and numerical results, the main conclusions drawn for the U-stringer specimens were:

- The DC sensors also detected the resin arrival, minimum viscosity, gel point, and end of the polymerization process, obtaining results very similar to those obtained for the shell specimens, which is not surprising given that both parts were manufactured with the same polymerization cycle.
- Regarding temperature monitoring, the sensors placed on the R5 wing recorded lower temperatures due to the proximity to the vacuum port. Furthermore, as was observed for the 2.5mm shell specimens, the part of the specimen in contact with the vacuum bag is usually warmer.
- The strain sensors showed lower strain generation during manufacturing compared to the shell specimens, and there was a clear uneven distribution of deformations, as differences were observed between sensors placed on both surfaces of the specimen. These differences were also observed in the post-manufacturing analysis: deformation variation was lower on the surface that was in contact with the mold during manufacturing, and more deformation was observed on the flange with a higher curvature radius, which also shows a greater reduction in the angle according to the 3D CMM. Therefore, it can be concluded that there are deformation differences in the thickness direction of the part, and these seem to be the most likely cause of shape distortions: deformation of the stringer core, leading to the warping (spring-in) of the flanges.

For the demonstrator built in PHASE 2, a number of specific conclusions can be drawn. From the lessons learned during the manufacturing of this assembly, several conclusions were drawn that were useful for designing the experimental part of the 1.2m scale demonstrator proposed for the numerical study:

- Correct adjustment of sensor integration strategies for complex 3D structures;
- Positioning of the optical fiber exit to preserve its integrity;
- Choosing better protective materials for optical fiber connections to minimize bending and thus signal attenuation;
- Appropriate geometry of auxiliary materials for optical fiber protection;
- The trade-off between the number of FBGs per fiber and redundant outputs.

These lessons learned are useful for designing the FBG sensor network map for the 1.2m scale demonstrator.

## 7.4 ORIGINAL SIMULATION STATEGY

In the calibration phase, initially conducted for the shell specimens, several parameters were varied, and we evaluated how these variations influenced the spring-in displacement:

- Varying the fiber volume fraction through the thickness of the laminate from 52% to 56% led to a 0.15 mm reduction in the displacement value;
- A constant fiber volume fraction through the thickness of the laminate caused an immediate response in the distortion behavior of the laminate, reducing the maximum displacement to 0.39 mm;
- An additional improvement through model calibration was achieved by applying a variable friction coefficient between the part and the mold. The parameter values were chosen as 0.01 before the gel point and 0.1 after the gel point threshold. This step did not affect the deflection value;
- An experiment that further reduced the calculated spring-in displacement value modified the initial degree of resin polymerization and applied a constant (high) friction coefficient of 1. The resulting calibration reduced the maximum displacement to 0.37 mm, which was considered acceptable, as no other calibration methods showed significant improvements compared to the test measurements;
- Previous research [***BC5.21***] has shown that friction coefficient values can be attributed to lower reasonable values (0.2–0.5) along with the implementation of an orthotropic friction behavior between the part and the mold. Given the nearly isotropic arrangement of the studied laminates, we considered this option to have a limited impact on distortion in the experimental and numerical trials [***BC5.22***].

After learning these lessons, a different geometry was simulated – the C-shape specimens. These were extremely valuable within the overall context of the ELADINE project, especially for providing data for geometric compensation of molds regarding the distortion of the angle between the spar flange and web. C-shape specimens were manufactured, monitored, and measured following the same procedure that was used for the shell specimens.

Evaluating the spring-in angles, we encountered some remarkable results:

- Both in the experiment and in simulations, the spring-in angle increased for larger corner radii. The average value for a 3 mm thick specimen was a 1.34° (1.78%) increase in the spring-in angle for a corner radius of 12 mm. For the same specimen, a corner radius of 5 mm only showed a 1.03° (1.34%) increase in the spring-in angle. In conclusion, the experimentally measured distortion shows that spring-in has a larger magnitude for larger corner radii, requiring more careful compensation measures.
- The core (web) of the C-shape specimen showed deformation during both measurement and simulation. This behavior was initially observed for the shell specimen simulation and experimental trials. It is critical to note that the curvature

axis will differ for parts that are stiffer due to their design geometry. The simulation strategy must account for the inherited geometric rigidity to simulate more complex geometries than flat or slightly curved panels.

- Given that the specimens were monitored for two weeks after completing the manufacturing cycle (without post-curing), the specimens showed minor variations in internal residual stress, which, in turn, led to minor variations in distortion. The research team observed this situation, but since the displacement change value measured over the entire monitoring period was considerably small, we chose not to include the post-curing behavior of the laminate in the simulation strategy.
- The fact that the simulation results were very close to the experimental values, as summarized in Tables 5.1–5.3, is remarkable and encouraging for the research effort.

The summary of the simulation results demonstrates that the developed numerical tool is reliable for predicting spring-in and warping for geometries such as nearly flat panels and flange/corner geometries. This simulation capability can be used to estimate distortion for practically any composite panel or corner/flange structure, provided that the material system's behavior is fully understood and the manufacturing process data and parameters are known and precisely controlled. The current development of the simulation can provide a solid foundation for more complex geometries and co-cured composite assemblies. However, the simulation strategy requires more checks and validations than distortion models for complex geometries. At this stage of development, numerical simulation tools can be reliably used to predict distortion for simple geometries, but the technical maturity is insufficient to obtain reliable results for complex shapes and assemblies.

A numerical simulation tool that can predict distortion for complex shapes is a valuable asset when designing complex molds. Such a simulation tool can be integrated into the overall design framework for composite structures and molds for composite structures in the following phases:

- Structural shape modeling – preliminary evaluation of critical geometric deviations;
- 3D verification of structural reinforcements for local distortions of geometry (flange angles and corners);
- Mold models and mold geometry compensation to prevent manufacturing distorted parts;
- Local checks for increased friction and part adhesion to the mold caused by distortion, which may lead to difficulties in part extraction.

These complex molds must account for certain conditions and critical manufacturing phases, such as part demolding, and the molds must be designed accordingly. In this regard, not only must spring-in be predicted, but also the manufacturability of the part and the distortion compensation strategy must be defined. Distortion scenarios, such as the one described in Figure 5.34, consider the likelihood of distortion for all surfaces of the part: the wing shell, spar

web, and caps. The scenario in Figure 5.15 was studied as part of a project dedicated to the construction of a composite mold [***BC5.23***]. The task of mold compensation for such scenarios is challenging, but within a composite mold compensation software environment, a numerical tool that deals with predicting spring-in for laminates is a natural improvement. Researchers are considering extending the capabilities of the distortion simulation tool into an accompanying CAD system for geometric compensation of composite molds.

## 7.5 ORIGINAL APPROACH REGARDING THE SIMULATION CAPABILITY OF DISTORTIONS IN REAL-SCALE MULTILAYER ANISOTROPIC AERONAUTICAL STRUCTURES

When using numerical simulations to predict spring-in and distortion, several conditions must be considered to guide the activity according to the established objective.
What is the purpose of our effort? We can use simulations to reduce the number of trials that a manufacturer needs to perform to achieve excellent and consistent part geometries, thereby reducing recurring costs. Simulations are extremely useful in the mold design phase. We can also use them to more accurately replicate the manufacturing conditions for new material systems specific to a particular manufacturer, thus optimizing the manufacturing process before mass production. However, the exclusive use of simulations involves a high risk; without solid experimental data regarding the behavior of selected materials and without precise information on process parameters, the distortion prediction results will be inaccurate and unreliable..

What is the factor with the greatest influence on distortion? After completing the experimental activities and numerical simulations, and analyzing the results of our study, the key parameter in controlling distortion values is the crosslinking degree gradient. Based on the sensitivity of the numerical model to parameter changes during the calibration phase, we can identify the mechanisms with the greatest influence on distortion:

- Tool-part interaction;
- Gradients in fiber volume fraction;
- Consolidation and variations in fiber volume fraction through the layer thickness;
- Variability in crosslinking degree, which determines the chemical shrinkage gradient of the resin.

What is the geometric complexity we want to simulate? This question is particularly relevant when manufacturing relatively simple parts, and the manufacturer already has a valuable database and precise practical rules for achieving high-quality parts. Other researchers have previously studied distortion behavior and mold compensation for complex double-curvature parts to evaluate simulation performance [***BC5.22***]. However, to obtain precise and accurate predictions of distortion in full-scale aeronautical structures, further investigation and advanced development of the numerical model will be required.

From a general perspective on the development of the numerical model, several aspects can be clearly mentioned as lessons learned in the process:

- The choice of protocols and mathematical models, the simulation philosophy, and the flow of the model were critical;
- Defining boundary conditions was probably the most difficult task to complete [***BC6.20***];
- Finding the appropriate corrective solution in the calibration process, as NOT ALL initial ideas worked with the best mature model [***BC6.21***];
- The simulation model must strike a balance between flexibility (the ability to calibrate) and robustness (the model must be able to run for different conditions);
- Material behavior – this was a recurring issue that required solving with realistic and robust input data in the simulation process. Not every time were we able to obtain the necessary material data, and in some cases, we used available information from the literature;
- A small-scale model behaves VERY differently from a large structure. Temperature gradients and variations in the degree of polymerization are parameters that influence the final distortion state. Following a non-robust approach leads to scaling difficulties from small test specimens to large structures. Sometimes, scaling is even impossible.

# GENERAL REFERENCES

**[BG.1]** Baran, I.; Cinar, K.; Ersoy, N.; Akkerman, R.; Hattel, J. A Review on the Mechanical Modeling of Composite. *Arch. Comput. Methods Eng.* **2017**, *24*, 365–395. https://doi.org/10.1007/s11831-016-9167-2.
**[BG.2]** Hubert P, Poursartip A (1998) A review of flow and compaction modelling relevant to thermoset matrix laminate processing. J Compos Mater 17(4):286–318
**[BG.3]** Johnston A (1997) An integrated model of the development of process-induced deformation in autoclave processing of composite structures. Ph.D. thesis, The University of British Columbia
**[BG.4]** Bogetti TA, Gillespie JW Jr (1992) Process-induced stress and deformation in thick-section thermoset composite laminates. J Compos Mater 26(5):626–660
**[BG.5]** Bogetti, T.A.; Gillespie, J.W., Jr. *Influence of Cure Shrinkage on Process-Induced Stress and Deformation in Thick Thermosetting Composites*; Technical report BRL-TR-3182; Army Ballistic Research Lab: Aberdeen Proving Ground, MD, USA, 1992
**[BG.6]** White SR, Hahn HT (1992) Process modelling of composite materials: residual stress development during cure. Part II.Experimental validation. J Compos Mater 26(16):2423–2453
**[BG.7]** Hubert, P.; Johnston, A.; Poursartip, A.; Nelson, K. Cure Kinetics and Viscosity Models for Hexcel 8552 Epoxy Resin. In Proceedings of the SAMPE Conference, Long Beach, CA, USA, 6–10 May 2001
**[BG.8]** Banu, C.; Bocioaga, M. Shape distortion prediction of high temperature curing laminates through a transient multi-physics numerical model. In Proceedings of the AIAA SCITECH 2024 Forum, Orlando, FL, USA, 8–12 January 2024.
**[BG.9]** Banu, C.; Bugaru, M. Development of a Numerical Tool for Laminate Composite Distortion Computation Through a Dual-Approach Strategy. Appl. Sci. 2024, 14(22), 10656; https://doi.org/10.3390/app142210656
**[BG.10]** Torre-Poza, A.; Pinto, A.M.R.; Grandal, T.; González-Castro, N.; Carral, L.; Travieso-Puente, R.; Rodríguez-Senín, E.; Banu, C.; Paval, A.; Bocioaga, M.; et al. ELADINE: Sensor monitoring and numerical model approach for composite material wing box shape distortions prediction. *IOP Conf. Ser. Mater. Sci. Eng.* **2022**, *1226*, 012001
**[BG.11]** MSC Marc Advanced Nonlinear Simulation Solution. Available online: https://hexagon.com/products/marc (accessed on 31 October 2024).
**[BG.12]** *MSC Software–MARC 2017.1–VOLUME A: Theory and User Information*; MSC Software: Newport Beach, CA, USA, 2017; pp. 945–954
**[BG.14]** Clean Sky 2 ELADINE Project in the Frame of H2020 Frame Program. Disponibil online: https://eladine-project.eu/ (accesat în 20 September 2024).
**[BG.14]** Clean Sky 2 OPTICOMS Project in the Frame of H2020 Frame Program. Disponibil online: https://opticoms-horizon2020.com/ (accesat în 20 septembrie 2024).
**[BG.15]** FITCoW - Full-scale Innovative integrated Tooling for Composite material Wing-box. Disponibil online: https://cordis.europa.eu/project/id/831985/results (accesat în 20 septembrie 2024).
[**BG.16**] Cesar Banu, *FITCoW – Co-polymerizing large-scale structures through OOA processes*, JEC Composites Magazine, **April-May 2022**. Disponibil online: https://digital-magazine.jeccomposites.com/jec-composites-magazine/jec-composites-magazine/n145-2022 (accesat în 18 martie 2025).

# ANEXX 1 – PUBLISED PAPERS WITH WoS and SCOPUS INDEX

*SCOPUS indexed*

1. Cesar Banu, *FITCoW – Co-polymerizing large-scale structures through OOA processes*, JEC Composites Magazine, **April-May 2022**. Disponibil online: https://digital-magazine.jeccomposites.com/jec-composites-magazine/jec-composites-magazine/n145-2022 (accesat în 18 martie 2025). ***JEC Composites Magazine,*** Issue 145, Pages 26 - 28, **SCOPUS INDEXEED** ISSN:1639965X, https://0d10e1015-y-https-www-scopus-com.z.e-nformation.ro/record/display.uri?eid=2-s2.0-85170530679&origin=resultslist&sort=plf-f&src=s&sid=f2d43e27c434cb272e0f829b0dbfd15d&sot=anl&sdt=aut&s=AU-ID%28%22Banu%2C+Cesar%22+58571368900%29&sl=32&sessionSearchId=f2d43e27c434cb272e0f829b0dbfd15d&relpos=2
2. Banu, C.; Bocioaga, M. Shape distortion prediction of high temperature curing laminates through a transient multi-physics numerical model. Conference Paper, Conference Proceedings, ISBN 978-162410711-5, DOI :10.2514/6.2024-2352, AIAA SciTech Forum and Exposition, 2024, Orlando, USA, 8 January through 12 January 2024,
   **SCOPUS INDEXEED,** https://0d10e1015-y-https-www-scopus-com.z.e-nformation.ro/record/display.uri?eid=2-s2.0-85196172544&origin=resultslist&sort=plf-f&src=s&sid=f2d43e27c434cb272e0f829b0dbfd15d&sot=anl&sdt=aut&s=AU-ID%28%22Banu%2C+Cesar%22+58571368900%29&sl=32&sessionSearchId=f2d43e27c434cb272e0f829b0dbfd15d&relpos=1

*WoS indexed*

3. Banu, C.; Bugaru, M. Development of a Numerical Tool for Laminate Composite Distortion Computation Through a Dual-Approach Strategy. MDPI-Applied Sciences, e-ISSN 2076-3417, **2024**, Volume14, Issue: 22, DOI:10.3390/app142210656, Article number: 10656, Published : November 2024, Indexed: 06/12/2024, **WOS:001366851500001**, https://www.webofscience.com/wos/woscc/full-record/WOS:001366851500001, **IF=2,5, Q1.**

*Conferences*

4. Banu, C.; Bugaru, Development of a numerical tool for laminate composites distortion computation through a dual approach strategy. 11th International Conference from "Scientific Computing to Computational Engineering", 11th IC-SCCE, 3-6 July, Loutraki, Greece, **2024**, pp. 75-84, ISSN: 2241-8865, ISBN: 978-618-84028-6-7